Use of patient-specific models for computer-assisted cochlear implant programming

By

Ahmet Cakir

Dissertation

Submitted to the Faculty of the

Graduate School of Vanderbilt University

in partial fulfillment of the requirements for the degree of

DOCTOR OF PHILOSOPHY

in

Computer Science

August 9th, 2019

Nashville, Tennessee

Approved:

Jack H. Noble, Ph.D.
Benoit M. Dawant, Ph.D.
Robert F. Labadie, M.D., Ph.D.
Bennett A. Landman, Ph.D.
Michael I. Miga, Ph.D.

TABLE OF CONTENTS

Page

LIST OF TABLES

LIST OF FIGURES

LIST OF ABBREVIATIONS

ACCRE	Advanced computing center for research and education
AGF	Amplitude growth function
ANFM	Auditory nerve fiber model
ANHI	Auditory nerve health imaging
ANOVA	Analysis of variance
AP	Alternating polarity
ASM	Active shape model
BEM	Boundary element method
BM	Basilar membrane
BMC	Basilar membrane curve
BP	Bipolar
C	Cochleostomy
CC	Correlation coefficient
CF	Current focusing
CI	Cochlear Implant
CDL	Cochlear duct length
CDP	Current density profile
COV	Coefficient of variation
CS	Current steering
CSM	Cochlear shape model
CT	Computed-tomography
DVF	Distance versus Frequency
EAM	Electro-anatomical model
EFI	Electrical field imaging
eCAP	Electrically evoked compound action potential

EFI	Electrical field imaging
ESP	Electrode stimulation patterns
FDM	Finite difference method
FMS	Forward-masking subtraction
FOV	Field of view
gSEF	Generalized Schwarz-Eikhof-Frijns
HH	Hodgkin-Huxley
IAC	Internal auditory canal
IGCIP	Image-guided cochlear implant programming
LRM	Linear regression model
mCD	Maximum total current density
MO	Modiolus
MP	Monopolar
MPI	Mask probe interval
MRI	Magnetic resonance imaging
NSL	Nerve soma location
OSL	Osseous spiral lamina
RC	Rosenthal's Canal
RM	Reissner's membrane
RT	Rotational tomography
RW	Round Window
SD	Standard deviation
SG	Spiral ganglion
SM	Scala media
SOE	Spread of excitation
ST	Scala tympani
SV	Scala vestibuli
TP	Tripolar

TPS	Thin-plate splines
VC	Virtual channels
wHH	Warm Hodgkin-Huxley
3-D	Three-dimensional
2-D	Two-dimensional
2T	Two-turn
μCT	MicroCT

Chapter I

INTRODUCTION

1.1 Cochlea and cochlear implants

Hearing is the outcome of a series of complex steps that translate sound wave signals into electrical signals. Incoming sound waves traveling through the ear canal reach cochlea, which is the snail-shaped fluid-filled cavity[1]. Cochlea is composed of three principal cavities called the scala tympani (ST), scala vestibuli (SV) and scala media (SM). The ST and SM are separated by the basilar membrane (BM) and the SM and SV are separated by Reissner's membrane (RM). The sound waves collected by the outer ear cause a ripple effect within cochlea which results in movement of the hair cells that correspond to the frequencies of the received sound[1].

The hair cells are tonotopically ordered by decreasing characteristic frequency along the length of the cochlea; the hair cells located within the lower part of the cochlea correspond to higher frequency of sounds, and those that are located in the upper part of the cochlea correspond to lower frequency sounds[3,4]. The movement of the corresponding hair cells releases chemicals into the ear inner activating the spiral ganglion nerve cells[5]. This stimulation is propagated along the auditory nerve fiber traveling through the brain stem and finally reaching the auditory cortex allowing the brain to process and hear the sound.

In simple terms, the inner ear performs a frequency spectrum decomposition of incoming signals, and the auditory nerve fibers send this information to the brain for further processing. In patients suffering from sensorineural hearing loss caused by abnormalities in hair cells, direct electrical stimulation of spiral ganglion cells is possible. This is done with a neural prosthesis

called a cochlear implant (CI)[6] as shown in Figure 1.1.

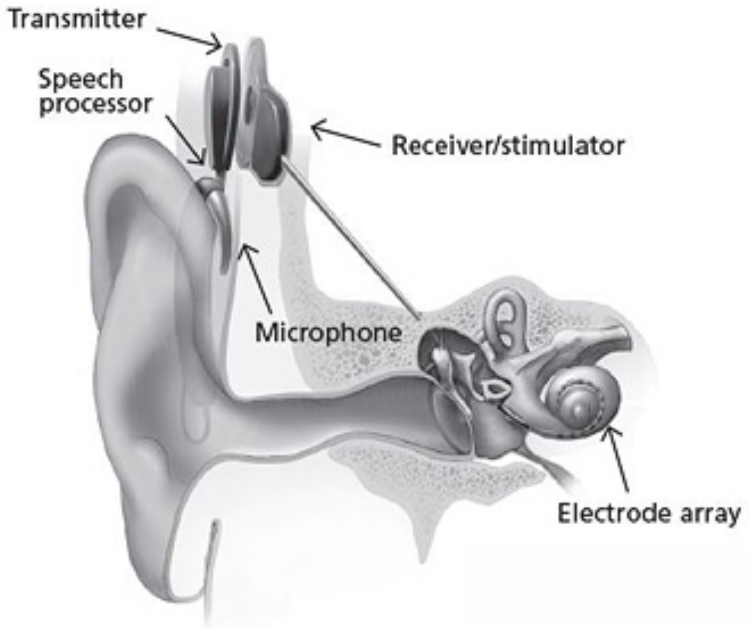

Figure 1.1. Example of a cochlear implant's external and internal parts. Image retrieved from[7].

The main components of a CI are an electrode array with up to 22 contacts that is surgically implanted into the cochlea, an externally-worn processor with microphone that picks up and decomposes the incoming signals, and a stimulator that transforms the output of the processor into biphasic electrical pulses that are sent to the appropriate contact in the electrode array. These high-frequency pulse trains stimulate the nerves in a frequency-specific manner to maintain tonotopicity of the system. Patient-specific parameter values for the processor are set by an audiologist in a series of office visits, resulting in a so-called MAP, and the process of selecting these parameter values is referred to as mapping.

With over 700,000 recipients worldwide and significant speech understanding benefits in the majority of those recipients, CIs are arguably the most successful neural prostheses to date. Yet, a significant number of recipients achieve poor outcomes and restoration to normal fidelity is

rare even among the best performers. The factors that affect hearing performance in CI recipients have been studied extensively. Scalar electrode location, the distance from electrodes to neural activation sites and neural survival are some of such factors. Electrode interaction is another factor that negatively affects the hearing performance of CI recipients. In natural hearing, each neural pathway can only be activated when the corresponding frequency is present in a sound. However, since CIs have relatively larger sizes of electrode contacts that create a wide current spread, each electrode stimulates a group of nerves that correspond to a wide range of frequencies.

This phenomenon known as channel interaction causes spectral smearing artifacts, which could be addressed and accounted for during clinical mapping sessions as CI devices allow manipulation of several settings, including activation or deactivation of contacts, assigning stimulation levels and sound frequency bands to each active electrode, etc. However, most of these settings are left at default during the mapping sessions due to lack of objective cues available that could indicate what settings will lead to better hearing outcomes. The audiologists depend heavily on patient feedback trying to optimize available CI settings, which is a difficult task because weeks or months of experience with given settings is necessary before the hearing performance can be reliably measured. Thus, the programming process often converges to sub-optimal settings and several sessions over the course of many years may be required.

In order to generate objective information that might indicate what settings will lead to better hearing outcomes, one would need to accurately determine the location of the electrodes as well as the electrode-neuron interface, which refers to an implant channel's ability to effectively stimulate the auditory nerve[8]. The positional factor of an electrode can be grouped into three different categories: (1) Scalar location of an electrode, i.e. whether the electrode lies within the ST or SV, (2) modiolar distance of an electrode, i.e. the distance between the electrode and the

neural activation sites; and (3) angular depth of the insertion. The scalar location[9,10] as well as modiolar distance[11] of electrodes have been found to correlate with hearing outcomes. Studies also suggest that hearing outcomes[12,13] as well as maintenance of residual hearing[14,15] are superior when all electrodes are located within the ST. Angular depth of insertion on the other hand had conflicting results with some studies showing better outcomes are associated with deeper[16–19] or shallower[10,11] insertions. Some factors such as distance to the modiolus have been little studied, and others such as depth of insertion led to conflicting findings. One potential reason for this is that methods used in aforementioned studies do not provide an accurate enough estimation of the position of intra-cochlear anatomy. Recent studies have shown that individual human cochleae differ not only in size but also in morphology[20–23]. Non-rigid variations, from the simplest variation of overall cochlea size to more complex variations such as changing proportions of specific areas (e.g. a deeper basal turn or a more horizontally positioned round window), need to be captured in order to accurately determine the position of the electrodes.

Another important factor is the electrode-neuron interface, which can be thought as spread of excitation caused by each electrode coupled with the health of the auditory nerve fibers along the length of cochlea. Analyses of temporal bones of CI users have revealed varying degrees of spiral ganglion counts of less than one third to almost 80% of those in age-matched healthy ears[8]. It has also been shown that neuron loss generally occurs heterogeneously, e.g. different segments of cochlea have different levels of neural survival[24,25]. Spiral ganglion loss as well as channel interaction, which occurs when two electrodes with two distinct frequency allocations stimulate the same nerve group, has been shown to limit spatial selectivity[26,27].

Thus, it is important to develop new techniques that could not only accurately localize the important structures within the cochlea, but could also predict the patient-specific electrode-neuron

interface in CI users. Our group has developed several image processing techniques that permit localization of anatomical structures that are of interest[28–31] as well as CI electrodes[32–34] in patient computed-tomography (CT) images with high accuracy. Using these techniques, our lab has developed the first image-guided CI programming (IGCIP) technique where electrode position is used to estimate the neural activation patterns caused by the electrodes, which is unique information that audiologists can use to define patient-specific CI processor settings[26]. Briefly, the patient cochlea anatomy is segmented using the pre-operative CT image, and the location of the intra-cochlear electrodes are segmented using the corresponding post-operative CT image. The anatomical structures segmented in the pre-operative CT are spatially aligned with the intra-cochlear electrodes segmented in the post-operative CT image. An example of the segmentation process is shown in Figure 1.2. The Euclidian distance from each electrode to the neural activation sites characterized by the frequencies to which they correspond is measured and is visualized using the Distance Vs. Frequency (DVF) curves. For each new patient, a DVF curve is created and an automatic method is used to generate patient-specific deactivation mapping plan[35].

In [26], IGCIP method was tested with a total of 68 patients, and significant improvements were reported for 39 out of 72 ears. In addition, patients elected to keep the experimental IGCIP maps for 56 ears (78%). Even though it has been shown that our IGCIP method leads to better hearing outcomes, it is possible that the method could be improved with a better estimate of the electrodes' neural activation patterns. In our current system, neural activation is estimated indirectly using only the Euclidian distance from each electrode to the neural activation sites as a surrogate for activation.

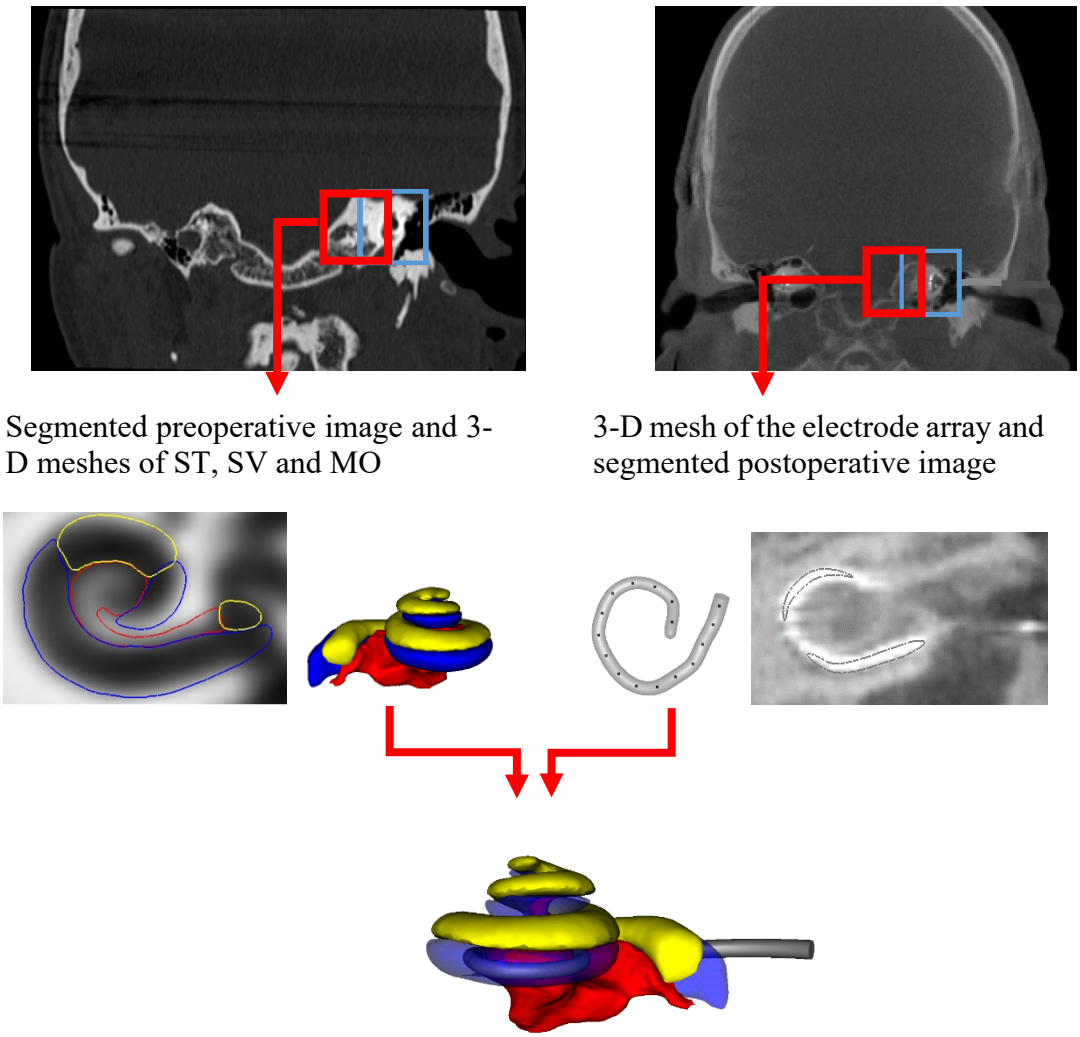

Figure 1.2. Overview of the process of segmenting the intra-cochlear structures as well as the electrodes.

We hypothesize not only that comprehensive and physics-based electro-anatomical and auditory nerve fiber models will better estimate neural activation patterns than our current approach but also that these models will enable us to estimate neural health along the length of cochlea which is currently not possible. In the remainder of this chapter, we present brief reviews on the methods that are currently used to determine the position of electrodes as defined above as well as methods that estimate the patient-specific electrode-neuron interface. We will also identify the limitations of such methods and introduce the contributions of this dissertation.

1.2 Effect of cochlear anatomy variations

Variability in human cochlea size has been previously demonstrated. Differences in cochlear anatomy exists not only between males and females but also between individual differences[20–23,36]. Because of variations in cochlea anatomy, detailed quantified information on the patient-specific differences need to be provided and such individual differences need to be taken into account in selecting appropriate prosthesis. Accurately estimating the shape and size of the cochlea can be beneficial in not only selecting the correct electrode array size for individual patients, but also in accurately determining the location of the electrode array.

Selection of a properly sized electrode array may be an important element in maintaining residual hearing and/or improving hearing outcomes for CI recipients. At present, CI companies offer a finite number of choices for electrode length and little to no instruction to optimize surgical placement given individualized anatomy. A properly sized electrode array might not only reduce the trauma caused by the electrode array insertion but also allow a better placement of the electrode array with respect to the neural activation sites. Studies suggest that a deeper insertion impacts scalar position and intra-cochlear trauma[10,37,38]. Finley et al.[10] and Radeloff et al.[38] found that insertion depth impacts scalar position and increases the number of electrodes in the SV, which is negatively correlated with hearing outcomes. Since the advent of cochlear implantation, multiple studies have assessed the role of using the cochlear duct length (CDL), which is defined as the length of the scala media, to determine the appropriate electrode length for implantation. This is particularly important as the length of the cochlea can vary between 25 and 45mm in patients[36,39–47] , and the angular depth of insertion is dependent upon CDL and the length of the implanted electrode. Ketten et al.[45] and Alexiades et al.[48] described a formula to calculate CDL at a given

angular depth using CT, and by measuring the distance from the middle of the round window (RW) to the farthest point on the opposite wall of the cochlea, denoted *A*. Determining the farthest point from the RW on the opposite lateral wall of the cochlea can be a demanding task given that surgeons are only presented 2D slices and the middle of the RW and the farthest point might be located on 2 different slices. A comparison between manually determined length *A*s as measured by two different experts is shown in Figure 1.3.

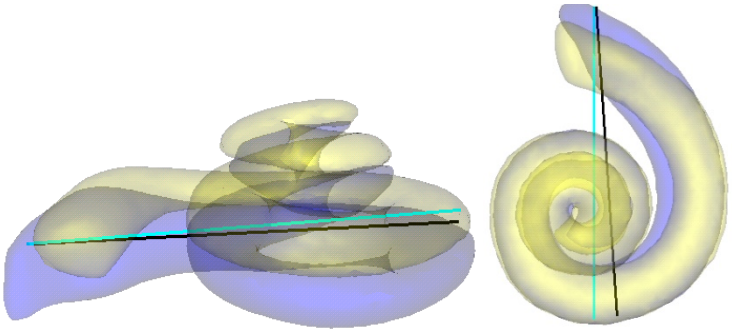

Figure 1.3. Length *A* measured by two expert neurotologists shown in different colors.

Manually determining *A* remains time consuming and operator dependent, and intra- or inter-observer variability in measurements might exist. An automatic method to measure CDL at a given angular depth would minimize the error introduced by the manual measurements and would provide a more accurate selection of a properly sized electrode array. As part of this dissertation, we have developed and evaluated an automatic way to measure both *A* and CDL. We have also compared expert measurements with automatic measurements of *A*, and investigate the sensitivity of the choice of electrode type to the choice of CDL measurement method by counting how often the choice of electrode would differ when different expert or automatic measures are used to estimate CDL.

Another factor that affects outcomes is electrode position which, as previously mentioned,

can be grouped into three different categories: (1) Scalar location of an electrode, (2) modiolar distance of an electrode, and (3) angular depth of the insertion. Different methods have been used in order to estimate the shape of the cochlea and localize intra-cochlear electrode positions, ranging from manually determining the intra-cochlear electrode location on CT images to creating cochlear shape models (CSM) and registering these models to patient images. Aschendorff et al.[13], Verbist et al.[49], and Boyer et al.[50] presented different manual segmentation techniques that use CT imaging to evaluate the correlation between the scalar electrode position and hearing outcomes. However, manually determining intra-cochlear electrode location using images alone is arduous and labor-intensive. In addition, CT imaging lacks the adequate resolution to visualize fine scale intra-cochlear structures, such as the modiolar wall.

Although CT imaging still remains the imaging modality best suited for this task, some groups have also used magnetic resonance imaging (MRI), which is the only modality that can directly visualize the membrane separating the ST and SV[51]. As it is not possible to use MRI for post-implantation imaging, Neri et al.[52] developed a technique in which postoperative CT images were registered to 1.5 T preoperative MRI images to assess electrode location within the membranous labyrinth. Even though this method allows visualization of certain intra-cochlear structures, the ST and SV were non-differentiable on MRI images. It is important to note that with current MRI technology achieving the high signal quality and CT-like resolution necessary to accurately image ST and SV requires hours of scan time and the use of high field scanners not yet approved for clinical use, making use of MRI for large scale analysis of patient cochleae not yet a viable option.

Creating CSM of intra-cochlear anatomy that can be registered to a patient CT image to define the location of the intra-cochlear structures was the approach in several papers[9–11], where a

rigid CSM was created using a histological image of a single cochlear specimen and was rigidly registered to new patient CT image.

However, as explained previously, non-rigid variations exist between different individuals, and using a single model that is rigidly registered to patient images does not provide an accurate enough estimation of the position of intra-cochlear anatomy. Indeed, this approach does not permit to take into account normal non-rigid inter-subject anatomical variations and thus leads to error when localizing anatomic structures. Anatomical differences that exist between two ex-vivo specimens are shown in Figure 1.4. These specimens are first manually segmented in high-resolution images and then rigidly registered to each other. As part of this thesis, we propose an approach to quantify the accuracy of measurements of intra-cochlear electrode positions when using rigid CSM. As rigid CSMs cannot capture the non-rigid variations between individuals, this study will also enable us to quantify the effect of cochlea anatomy variations on electrode localization. Another application of interest for which selection of an accurate CSM is important is creating of patient-specific EAMs. Since EAMs depends on accurate localization of intra-cochlear electrode position for each patient, choosing an appropriate cochlear model is crucial.

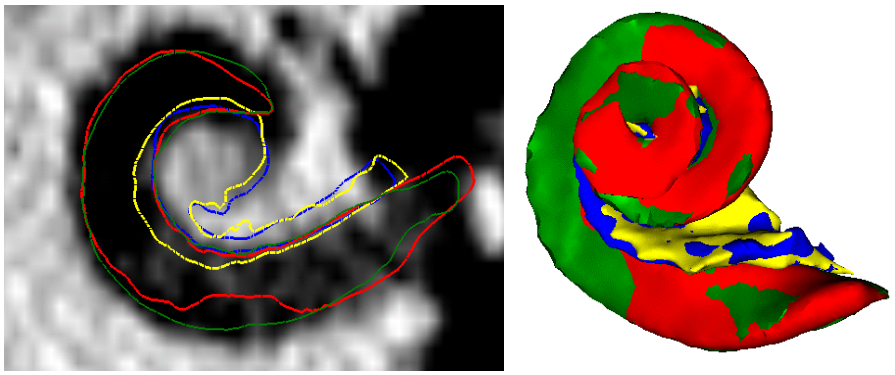

(a) (b)

Figure 1.4. Two rigid shape models containing scala tympani and modiolus. The contours are shown on a CT image (a) and in 3D meshes (b).

1.3 Electro-anatomical model of the electrically stimulated cochlea

Noble et al.[26] showed that neural activation caused by CI electrodes can be estimated from CT images. The DVF curve based spatial analysis approach has been successful when used for coarse strategies, but these techniques rely on Euclidean distance measured between the electrodes and the nerves. Work from other groups has shown that purely distance-based measures do not provide an accurate estimation of stimulation patterns[53]. Thus, we need to develop more comprehensive models to accurately estimate stimulation and neural activation patterns. A computational electro-anatomical model can be used to estimate patient-specific current density fields created by the electrodes, and the magnitude of these fields in the region where neural activation occurs estimates the neural stimulation patterns. EAMs can estimate stimulation patterns more accurately than distance based measures because these simulation: (a) account for the differing electrical properties of tissues when estimating the distribution of electrical current, (b) can account for the size and shape of contacts when estimating the current patterns emitted from those contacts, and (c) can account for complex anatomical geometry to simulate events such as cross-turn stimulation, which is a phenomenon where current injected at one location in the cochlea can cross through the thin tissue separating one turn of the cochlea from another to stimulate entirely separate groups of nerves. Cross-turn stimulations have long been suspect to cause performance degradations[54,55]. An example of the resulting voltage map is shown in Figure 1.5.

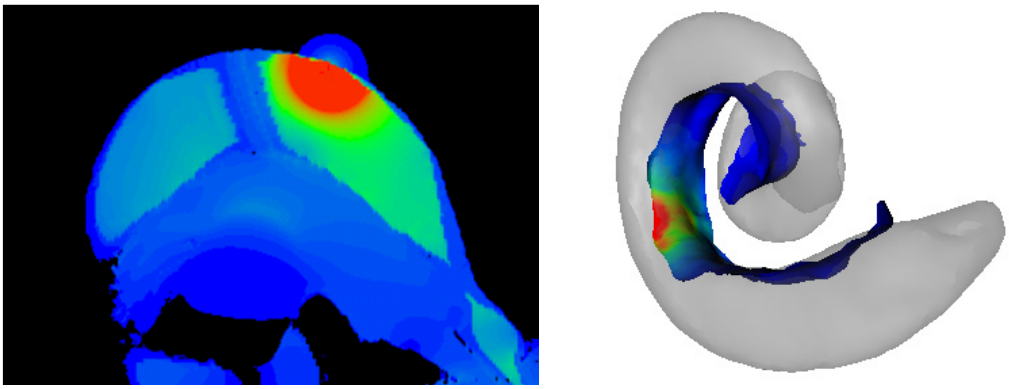

(a) (b)

Figure 1.5. An example of a resulting current density map within cochlea (a) and along the neural interface (b)

Several groups have used EAMs to study intra-cochlear voltage distribution and its effect on neural activation. Several methods to create EAMs have been adopted by different groups ranging from using a rotationally symmetric model of human cochlea[55] to using human cochleae from histological images. Although these models have been shown to be useful, they cannot be applied in vivo; thus, patient-specific differences cannot be incorporated into these models. Additionally, these models do not account for patient-specific electrical characteristics, i.e., the resistivity value of different tissue types. This is important because the ultimate goal of such models is to estimate neural stimulation patterns, and to do so accurately will require accurately estimating the voltage distribution in the cochlea.

As part of this thesis, we are proposing a method to anatomically and electrically customize EAMs using patient CT images and electric field imaging (EFI) data, respectively. EFI is measured such that one electrode at a time is activated while voltage at each of the remaining electrodes in the cochlea is measured, thus sampling the intra-cochlear potentials at sites where electrodes sit. Electrical customization method also includes a step in which intra-cochlear regions where fibrous tissue might have grown is determined. This is a phenomenon seen with CI users, where after the

electrode insertion, the body treats the electrode array as a foreign object and starts forming scar/fibrous tissue around it[56–59]. This is a crucial step as it has been shown that the efficiency of CIs is affected by such tissue growths consisting of inflammation or fibrosis[60].

1.4 Auditory nerve fiber model

The response of an auditory nerve fiber to an external stimulation depends on the electrical and physical properties of the nerve as well as the strength and polarity of the extracellular potential. Electrical properties i.e. ion channels, myelination, conductance, etc., and physical properties i.e. length and diameter of different parts of the nerve can be modeled using a compartmental auditory nerve fiber model (ANFM). ANFMs can be used not only to better analyze and understand the neural response caused by the CI electrodes, but also to better program CIs.

Several groups have worked on predicting neural activation caused by electrical stimulation. In one of the earliest works, Rattay[61] used a current term generated from an EAM which is proportional to the second spatial derivative of the extracellular field and concluded that the activity of the axon depends on the second derivative of the extracellular medium, denoted as the "activating function".

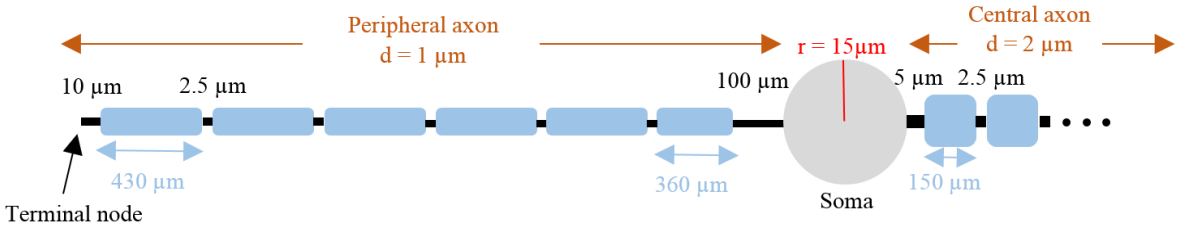

Figure 1.6. The geometrical properties of the auditory nerve fiber.

This was the method of choice in [62,63]. However, the activating function is a first approximation

which assumes that the axon is infinitely long and thus, in a resting state[64] when stimulated by a constant source, which would not hold true for a finite length axon placed in a non-uniform extracellular field. Most common models that are integrated into non-uniform EAMs are physiologically-based active membrane nerve models as shown in Figure 1.6. The potential at the active sites calculated by the EAMs are used to predict the activation of auditory nerve fibers. Such models were employed by several different groups in their studies[65–70]. These methods developed in the aforementioned studies either lack the capacity to be applied in-vivo[65,68–70] or only confine themselves to anatomical customization[71] and do not make us of the physiological measurements that are clinically available. In this work we are proposing a semi-automatic way to create a physiologically-based active membrane nerve model. Our approach involves creating subject-customized computational models of auditory nerve fibers that are parameterized by neural health. Fiber-specific neural health is numerically estimated such that electrically evoked compound action potential (eCAP) model simulations match eCAPs measured directly from the CI. We clinically evaluate the auditory neural health estimations with clinically measured psychophysical measurements. This breakthrough could provide an unprecedented window into the health of the inner ear, opening the door for studying population variability and intra-subject neural health dynamics. It could further potentially transform the CI rehabilitation process by permitting comprehensive subject-specific simulation and optimization of the neural stimulation strategy based on the health of the electro-neural interface.

1.5 Goals and contributions of the dissertation

The goals of this dissertation are to develop patient-specific electro-anatomical models (EAMs) and auditory nerve fiber models (ANFMs) and clinically verify them. Fine resolution anatomical

as well as tissue electrical properties are incorporated into the EAMs. The methods developed in this dissertation allow such information to be transferred from high-resolution μCT images to patient CT image with high accuracy. μCTs have the resolution necessary to detect some of the fine structures required for accurate electrical modeling, such as Rosenthal's canal and the neural pathways. While EAMs constructed using image-based techniques are quite useful, they cannot accurately capture certain patient-specific factors such as post-implantation tissue growth or regions that lack neural survival. Thus, taking advantage of ANFMs as well as physiological measurements such as electric field imaging and electrically evoked compound action potentials, we propose a method that can potentially estimate tissue growth regions as well as regions that lack neural survival.

The specific contributions of this dissertation are summarized below:

Chapter II presents the effects of non-rigid variations in cochlea anatomy on intra-cochlear electrode localization. This is important because constructing an accurate EAM and simulating a variety of physiological CI measurements depend not only on accurate segmentation of the anatomical structures but also on accurate localization of the electrode positions with respect to these structures.

Chapter III proposes an automatic method to measure both length *A*, the line from the center of the round window through modiolus to the farthest point on the lateral wall of the basal turn of the cochlea, as well as cochlear duct, measured from round window to the helicotrema. Such measurements are important not only in selecting the appropriate size of array but also in comparing individual cochleae differences.

Chapter IV introduces a method that allows construction of high-resolution EAMs of electrically stimulated cochlea from μCT images of ex-vivo specimens. We extend this method by

incorporating fine resolution tissue electrical property information that can be transferred from high-resolution μCT images to patient CTs to create *in-vivo* patient-specific models that approximate electrical tissue properties. We compare these patient-specific models to models created from ground-truth μCT images.

Chapter V presents the optimization algorithm we developed in order to electrically customize patient-specific EAMs. This method uses physiological measurements called electric field imaging in order to optimize the resistivity values of different tissue types, namely soft and neural tissue. This is an important step in creating patient-specific electro-anatomical and auditory nerve fiber models because the resistivity values will change the path of the current that flows between an active electrode and the distant ground, which in turn will affect the neural activation patterns caused by each electrode.

Chapter VI proposes a graph-search based algorithm used to segment auditory nerve fibers. CT image slices do not have the adequate resolution to accurately visualize the fine intra-cochlear structures including the auditory nerve fibers, which are roughly 2μm in width. Thus, our algorithm relies on a priori information of the morphology of the fibers to estimate their positon. Since the location of certain structures crucial in nerve fiber segmentation are estimated, it is important to evaluate the sensitivity of the algorithm as well as auditory nerve fiber models to moderate changes in nerve fiber shape.

Chapter VII introduces the method we developed in order to create patient-specific auditory nerve fiber models (ANFMs). Coupled with electro-anatomical models, ANFMs can provide insight with respect to the health of the inner ear, opening the door for studying intra-subject neural health dynamics. It could further transform the cochlear implant rehabilitation process by permitting comprehensive subject-specific simulation and optimization of the neural

stimulation strategy based on the health of the electro-neural interface. In this work, we have developed the first approach for estimating *in vivo*, subject-specific health of auditory nerve fiber populations in different regions of the inner ear. Our approach involves creating subject-customized computational models of auditory nerve fibers that are parameterized by neural health. In order to evaluate the validity of our ANFMs, we have performed clinical tests and compared the results to our estimations.

Chapter VIII provides the summary of the work and discusses possible future work.

References

1. How Do We Hear? | NIDCD. https://www.nidcd.nih.gov/health/how-do-we-hear. Accessed April 10, 2019.

2. Hudspeth AJ. Integrating the active process of hair cells with cochlear function. *Nature Reviews Neuroscience*. 2014;15(9):600-614. doi:10.1038/nrn3786

3. Stakhovskaya O, Sridhar D, Bonham BH, Leake PA. Frequency Map for the Human Cochlear Spiral Ganglion: Implications for Cochlear Implants. *J Assoc Res Otolaryngol*. 2007;8(2):220-233. doi:10.1007/s10162-007-0076-9

4. Greenwood DD. A cochlear frequency-position function for several species--29 years later. *J Acoust Soc Am*. 1990;87(6):2592-2605.

5. Cochlear Implants. :2.

6. Wilson BS, Dorman MF. Cochlear implants: current designs and future possibilities. *J Rehabil Res Dev*. 2008;45(5):695-730.

7. https://www.nidcd.nih.gov/health/cochlear-implants

8. Bierer JA. Probing the electrode-neuron interface with focused cochlear implant stimulation. *Trends Amplif*. 2010;14(2):84-95. doi:10.1177/1084713810375249

9. Skinner MW, Holden TA, Whiting BR, et al. In vivo estimates of the position of advanced bionics electrode arrays in the human cochlea. *Ann Otol Rhinol Laryngol Suppl*. 2007;197:2-24.

10. Finley CC, Holden TA, Holden LK, et al. Role of electrode placement as a contributor to variability in cochlear implant outcomes. *Otol Neurotol*. 2008;29(7):920-928. doi:10.1097/MAO.0b013e318184f492

11. Holden LK, Finley CC, Firszt JB, et al. Factors affecting open-set word recognition in adults with cochlear implants. *Ear Hear*. 2013;34(3):342-360. doi:10.1097/AUD.0b013e3182741aa7

12. Wanna GB, Noble JH, Carlson ML, et al. Impact of electrode design and surgical approach on scalar location and cochlear implant outcomes. *Laryngoscope*. 2014;124 Suppl 6:S1-7. doi:10.1002/lary.24728

13. Aschendorff A, Kubalek R, Turowski B, et al. Quality control after cochlear implant surgery by means of rotational tomography. *Otol Neurotol*. 2005;26(1):34-37.

14. Wanna GB, Noble JH, Gifford RH, et al. Impact of Intrascalar Electrode Location, Electrode Type, and Angular Insertion Depth on Residual Hearing in Cochlear Implant Patients: Preliminary Results. *Otol Neurotol*. 2015;36(8):1343-1348. doi:10.1097/MAO.0000000000000829

15. Nordfalk KF, Rasmussen K, Hopp E, Greisiger R, Jablonski GE. Scalar position in cochlear implant surgery and outcome in residual hearing and the vestibular system. *Int J Audiol*. 2014;53(2):121-127. doi:10.3109/14992027.2013.854413

16. Skinner MW, Ketten DR, Holden LK, et al. CT-derived estimation of cochlear morphology and

electrode array position in relation to word recognition in Nucleus-22 recipients. *J Assoc Res Otolaryngol*. 2002;3(3):332-350. doi:10.1007/s101620020013

17. Yukawa K, Cohen L, Blamey P, Pyman B, Tungvachirakul V, O'Leary S. Effects of insertion depth of cochlear implant electrodes upon speech perception. *Audiol Neurootol*. 2004;9(3):163-172. doi:10.1159/000077267

18. Hochmair I, Arnold W, Nopp P, Jolly C, Müller J, Roland P. Deep electrode insertion in cochlear implants: apical morphology, electrodes and speech perception results. *Acta Otolaryngol*. 2003;123(5):612-617.

19. O'Connell BP, Cakir A, Hunter JB, et al. Electrode Location and Angular Insertion Depth are Predictors of Audiologic Outcomes in Cochlear Implantation. *Otol Neurotol*. 2016;37(8):1016-1023. doi:10.1097/MAO.0000000000001125

20. Erixon E, Högstorp H, Wadin K, Rask-Andersen H. Variational anatomy of the human cochlea: implications for cochlear implantation. *Otol Neurotol*. 2009;30(1):14-22. doi:10.1097/MAO.0b013e31818a08e8

21. Avci E, Nauwelaers T, Lenarz T, Hamacher V, Kral A. Variations in microanatomy of the human cochlea. *J Comp Neurol*. 2014;522(14):3245-3261. doi:10.1002/cne.23594

22. Verbist BM, Ferrarini L, Briaire JJ, et al. Anatomic considerations of cochlear morphology and its implications for insertion trauma in cochlear implant surgery. *Otol Neurotol*. 2009;30(4):471-477. doi:10.1097/MAO.0b013e3181a32c0d

23. Pelosi S, Noble JH, Dawant BM, Labadie RF. Analysis of intersubject variations in intracochlear and middle ear surface anatomy for cochlear implantation. *Otol Neurotol*. 2013;34(9):1675-1680. doi:10.1097/MAO.0b013e3182a1a7e6

24. Fayad JN, Linthicum FJH. Multichannel cochlear implants: relation of histopathology to performance. *The Laryngoscope*. 2006;116(8):1310-1320. doi:10.1097/01.mlg.0000227176.09500.28

25. Khan AM, Whiten DM, Nadol JB, Eddington DK. Histopathology of human cochlear implants: correlation of psychophysical and anatomical measures. *Hear Res*. 2005;205(1-2):83-93. doi:10.1016/j.heares.2005.03.003

26. Noble JH, Labadie RF, Gifford RH, Dawant BM. Image-guidance enables new methods for customizing cochlear implant stimulation strategies. *IEEE Trans Neural Syst Rehabil Eng*. 2013;21(5):820-829. doi:10.1109/TNSRE.2013.2253333

27. Noble JH, Gifford RH, Hedley-Williams AJ, Dawant BM, Labadie RF. Clinical evaluation of an image-guided cochlear implant programming strategy. *Audiol Neurootol*. 2014;19(6):400-411. doi:10.1159/000365273

28. Noble JH, Labadie RF, Majdani O, Dawant BM. Automatic segmentation of intracochlear anatomy in conventional CT. *IEEE Trans Biomed Eng*. 2011;58(9):2625-2632. doi:10.1109/TBME.2011.2160262

29. Noble JH, Gifford RH, Labadie RF, Dawant BM. Statistical shape model segmentation and frequency mapping of cochlear implant stimulation targets in CT. *Med Image Comput Comput Assist Interv*.

2012;15(Pt 2):421-428.

30. Reda FA, McRackan TR, Labadie RF, Dawant BM, Noble JH. Automatic segmentation of intra-cochlear anatomy in post-implantation CT of unilateral cochlear implant recipients. *Med Image Anal*. 2014;18(3):605-615. doi:10.1016/j.media.2014.02.001

31. Reda FA, Noble JH, Labadie RF, Dawant BM. An artifact-robust, shape library-based algorithm for automatic segmentation of inner ear anatomy in post-cochlear-implantation CT. *Proc SPIE Int Soc Opt Eng*. 2014;9034:90342V. doi:10.1117/12.2043260

32. Noble JH, Schuman TA, Wright CG, Labadie RF, Dawant BM. Automatic Identification of Cochlear Implant Electrode Arrays for Post-Operative Assessment. *Proc SPIE Int Soc Opt Eng*. 2011;7962. doi:10.1117/12.878490

33. Zhao Y, Dawant BM, Labadie RF, Noble JH. Automatic localization of cochlear implant electrodes in CT. *Med Image Comput Comput Assist Interv*. 2014;17(Pt 1):331-338.

34. Noble JH, Dawant BM. Automatic graph-based localization of cochlear implant electrodes in CT. *Med Image Comput Comput Assist Interv*. 2015;9350:152-159.

35. Zhao Y, Dawant BM, Noble JH. Automatic electrode configuration selection for image-guided cochlear implant programming. In: *Medical Imaging 2015: Image-Guided Procedures, Robotic Interventions, and Modeling*. Vol 9415. International Society for Optics and Photonics; 2015:94150K. doi:10.1117/12.2081473

36. Miller JD. Sex differences in the length of the organ of Corti in humans. *The Journal of the Acoustical Society of America*. 2007;121(4):EL151-EL155. doi:10.1121/1.2710746

37. Adunka O, Kiefer J. Impact of electrode insertion depth on intracochlear trauma. *Otolaryngol Head Neck Surg*. 2006;135(3):374-382. doi:10.1016/j.otohns.2006.05.002

38. Radeloff A, Mack M, Baghi M, Gstoettner WK, Adunka OF. Variance of angular insertion depths in free-fitting and perimodiolar cochlear implant electrodes. *Otol Neurotol*. 2008;29(2):131-136. doi:10.1097/MAO.0b013e318157f0ea

39. Walby AP. Scala tympani measurement. *Ann Otol Rhinol Laryngol*. 1985;94(4 Pt 1):393-397.

40. Úlehlová L, Voldřich L, Janisch R. Correlative study of sensory cell density and cochlear length in humans. *Hearing Research*. 1987;28(2):149-151. doi:10.1016/0378-5955(87)90045-1

41. Wright A, Davis A, Bredberg G, et al. Hair cell distributions in the normal human cochlea. A report of a European working group. *Acta Otolaryngol Suppl*. 1987;436:15-24.

42. Bredberg G, Teti A, Zambonin Zallone A, Lundevall E, Iurato S. Ultrastructural evaluation of the microslicing method for the study of temporal bone pathology. *Acta Otolaryngol Suppl*. 1987;436:7-14.

43. Ariyasu L, Galey FR, Hilsinger R, Byl FM. Computer-generated three-dimensional reconstruction of the cochlea. *Otolaryngol Head Neck Surg*. 1989;100(2):87-91. doi:10.1177/019459988910000201

44. Kawano A, Seldon HL, Clark GM. Computer-aided three-dimensional reconstruction in human

cochlear maps: measurement of the lengths of organ of Corti, outer wall, inner wall, and Rosenthal's canal. *Ann Otol Rhinol Laryngol*. 1996;105(9):701-709. doi:10.1177/000348949610500906

45. Ketten DR, Skinner MW, Wang G, Vannier MW, Gates GA, Neely JG. In vivo measures of cochlear length and insertion depth of nucleus cochlear implant electrode arrays. *Ann Otol Rhinol Laryngol Suppl*. 1998;175:1-16.

46. Adunka O, Unkelbach MH, Mack MG, Radeloff A, Gstoettner W. Predicting Basal Cochlear Length for Electric-Acoustic Stimulation. *Arch Otolaryngol Head Neck Surg*. 2005;131(6):488-492. doi:10.1001/archotol.131.6.488

47. Lee J, Nadol JB, Eddington DK. Depth of Electrode Insertion and Postoperative Performance in Humans with Cochlear Implants: A Histopathologic Study. *Audiol Neurootol*. 2010;15(5):323-331. doi:10.1159/000289571

48. Alexiades G, Dhanasingh A, Jolly C. Method to estimate the complete and two-turn cochlear duct length. *Otol Neurotol*. 2015;36(5):904-907. doi:10.1097/MAO.0000000000000620

49. Verbist BM, Frijns JHM, Geleijns J, van Buchem MA. Multisection CT as a valuable tool in the postoperative assessment of cochlear implant patients. *AJNR Am J Neuroradiol*. 2005;26(2):424-429.

50. Boyer E, Karkas A, Attye A, Lefournier V, Escude B, Schmerber S. Scalar localization by cone-beam computed tomography of cochlear implant carriers: a comparative study between straight and periomodiolar precurved electrode arrays. *Otol Neurotol*. 2015;36(3):422-429. doi:10.1097/MAO.0000000000000705

51. van Egmond SL, Visser F, Pameijer FA, Grolman W. Ex vivo and in vivo imaging of the inner ear at 7 Tesla MRI. *Otol Neurotol*. 2014;35(4):725-729. doi:10.1097/MAO.0000000000000276

52. Neri E, Berrettini S, Salvatori L, Forli F, Franceschini SS, Bartolozzi C. 3-D CT and MRI co-registration in the assessment of cochlear implantation. *Med Sci Monit*. 2005;11(10):MT63-67.

53. Whiten DM (Darren M. Electro-anatomical models of the cochlear implant. 2007. http://dspace.mit.edu/handle/1721.1/38518. Accessed April 10, 2019.

54. Briaire JJ, Frijns JHM. The consequences of neural degeneration regarding optimal cochlear implant position in scala tympani: a model approach. *Hear Res*. 2006;214(1-2):17-27. doi:10.1016/j.heares.2006.01.015

55. Frijns JH, Briaire JJ, Grote JJ. The importance of human cochlear anatomy for the results of modiolus-hugging multichannel cochlear implants. *Otol Neurotol*. 2001;22(3):340-349.

56. Choi C-H, Oghalai JS. Predicting the effect of post-implant cochlear fibrosis on residual hearing. *Hearing Research*. 2005;205(1):193-200. doi:10.1016/j.heares.2005.03.018

57. Hanekom T. Modelling encapsulation tissue around cochlear implant electrodes. *Med Biol Eng Comput*. 2005;43(1):47-55. doi:10.1007/BF02345122

58. Wilk M, Hessler R, Mugridge K, et al. Impedance Changes and Fibrous Tissue Growth after Cochlear Implantation Are Correlated and Can Be Reduced Using a Dexamethasone Eluting Electrode. *PLoS ONE*. 2016;11(2):e0147552. doi:10.1371/journal.pone.0147552

59. Keithley EM, Chen MC, Linthicum F. Clinical diagnoses associated with histologic findings of fibrotic tissue and new bone in the inner ear. *Laryngoscope*. 1998;108(1 Pt 1):87-91.

60. Kamakura T, Nadol JB. Correlation between word recognition score and intracochlear new bone and fibrous tissue after cochlear implantation in the human. *Hear Res*. 2016;339:132-141. doi:10.1016/j.heares.2016.06.015

61. Rattay F, Lutter P, Felix H. A model of the electrically excited human cochlear neuron. I. Contribution of neural substructures to the generation and propagation of spikes. *Hear Res*. 2001;153(1-2):43-63.

62. Nicoletti M, Wirtz Chr, Hemmert W. Modeling Sound Localization with Cochlear Implants. In: Blauert J, ed. *The Technology of Binaural Listening*. Modern Acoustics and Signal Processing. Berlin, Heidelberg: Springer Berlin Heidelberg; 2013:309-331. doi:10.1007/978-3-642-37762-4_12

63. Finley CC, Wilson BS, White MW. Models of Neural Responsiveness to Electrical Stimulation. In: Miller JM, Spelman FA, eds. *Cochlear Implants: Models of the Electrically Stimulated Ear*. New York, NY: Springer New York; 1990:55-96. doi:10.1007/978-1-4612-3256-8_5

64. Hanekom T. Three-dimensional spiraling finite element model of the electrically stimulated cochlea. *Ear Hear*. 2001;22(4):300-315.

65. Frijns JH, de Snoo SL, ten Kate JH. Spatial selectivity in a rotationally symmetric model of the electrically stimulated cochlea. *Hear Res*. 1996;95(1-2):33-48.

66. Kalkman RK, Briaire JJ, Frijns JHM. Current focussing in cochlear implants: an analysis of neural recruitment in a computational model. *Hear Res*. 2015;322:89-98. doi:10.1016/j.heares.2014.12.004

67. Kalkman RK, Briaire JJ, Dekker DMT, Frijns JHM. Place pitch versus electrode location in a realistic computational model of the implanted human cochlea. *Hear Res*. 2014;315:10-24. doi:10.1016/j.heares.2014.06.003

68. Cartee LA. Spiral ganglion cell site of excitation II: numerical model analysis. *Hear Res*. 2006;215(1-2):22-30. doi:10.1016/j.heares.2006.02.011

69. Cartee LA. Evaluation of a model of the cochlear neural membrane. II: comparison of model and physiological measures of membrane properties measured in response to intrameatal electrical stimulation. *Hear Res*. 2000;146(1-2):153-166.

70. Frijns JHM, Briaire JJ, Schoonhoven R. Integrated use of volume conduction and neural models to simulate the response to cochlear implants. *Simulation Practice and Theory*. 2000;8(1):75-97. doi:10.1016/S0928-4869(00)00008-2

71. Malherbe TK, Hanekom T, Hanekom JJ. Constructing a three-dimensional electrical model of a living cochlear implant user's cochlea. *Int J Numer Method Biomed Eng*. 2016;32(7). doi:10.1002/cnm.2751

Chapter II

EVALUATION OF RIGID COCHLEAR MODELS FOR MEASURING COCHLEAR IMPLANT ELECTRODE POSITION

Ahmet Cakir[1], Robert F. Labadie[2], M. Geraldine Zuniga[2], Benoit M. Dawant[1], Jack H. Noble[1]

[1]Department of Electrical Engineering and Computer Science, Vanderbilt University, Nashville, TN 37232

[2]Department of Otolaryngology-Head and Neck Surgery, Vanderbilt University Medical Center, Nashville, TN 37232

Abstract

Objective: To investigate the accuracy of rigid cochlear models in measuring intra-cochlear positions of cochlear implant (CI) electrodes

Patients: 93 adults who had undergone CI and pre- and post-operative CT imaging.

Main Outcome Measures: Seven rigid models of cochlear anatomy were constructed using micro-CTs of cochlear specimens. Using each of the 7 models, the position of each electrode in each of the 98 ears in our dataset was measured as its depth along the length of the cochlea, its distance to the basilar membrane, and its distance to the modiolus. Cochlear duct length was also measured using each model.

Results: Standard deviation across rigid cochlear models in measures of electrode depth, distance to basilar membrane, distance to modiolus, and length of the cochlear duct at two turns were 0.68, 0.11, 0.15, and 1.54 mm. Comparing the estimated position of the electrodes with respect to the basilar membrane, i.e., deciding whether an electrode was located within the scala tympani (ST) or the scala vestibuli (SV), there was not a unanimous agreement between the models for 19% of

all the electrodes. With respect to the modiolus, each electrode was classified into one of the three groups depending on its modiolar distance: Close, medium, and far. Rigid models did not unanimously agree on modiolar distance for approximately 50% of the electrodes tested.

Conclusions: Inter-model variance of rigid cochlear models exists, demonstrating that measurements made using rigid cochlear models are limited in terms of accuracy due to non-rigid inter-subject variations in cochlear anatomy.

2.1 Introduction

Cochlear implants (CIs) are considered standard treatment for patients who experience sensorineural hearing loss. Each CI has an electrode array with a certain number of electrodes, between 12 and 22, depending on the type and the manufacturer. The electrode array is surgically inserted into the cochlea. Although CIs have been very successful at restoring hearing, restoration to normal auditory performance is rare, and some CI recipients may experience poor outcomes. Electrode position is one of the factors that has been shown in several studies to affect hearing outcomes. However, the intra-cochlear positioning of the electrode array is invisible to the surgeon as the array must be blindly threaded into the cochlea through a small opening, and x-ray-based imaging modalities have been the only option for intra-operative imaging but are difficult to interpret and to implement in the traditional clinical workflow. Different groups have tried to estimate the shape of the cochlea and localize intra-cochlear electrode positions using post-implantation computed-tomography (CT) imaging, which remains the imaging modality best suited for postoperative CI imaging. Aschendorff et al.[1] used rotational tomography (RT) to manually determine whether electrodes were located within the scala tympani (ST) or the scala vestibuli (SV). In a later study[2], this imaging approach was used to show that hearing outcomes

are correlated with the scalar positioning of the electrode array. Verbist et al.[3] presented another CT imaging technique to evaluate electrode scalar position. Recently, Boyer et al.[4] presented another technique using cone-beam CT to study the scalar positioning of electrode arrays. However, manually determining intra-cochlear electrode location using images alone is arduous. Further, while these methods may be accurate enough to detect correlations of gross differences in electrode positioning with hearing outcomes with a large enough dataset, they are prone to error. This is because it is not possible in CT to directly visualize fine scale intra-cochlear structures, such as the modiolar wall (the inner wall of the cochlea) or the basilar membrane and the bone that separate the ST from the SV, because of the lack of adequate resolution of the CT.

Magnetic resonance imaging (MRI) is another modality that has great potential for imaging the cochlea. It is the only modality that can directly visualize the ST and SV[5]. However, it is not possible to use MRI for post-implantation imaging because the electrodes within the cochlea corrupt the MRI signal in the region around the cochlea. In addition, only certain types of MRI are considered safe for cochlear implant recipients. Neri et al.[6] developed a technique in which postoperative CT images were registered to 1.5 T preoperative MRI images to assess electrode location within the membranous labyrinth. Even though this method allows visualization of certain intra-cochlear structures, the ST and SV were non-differentiable on MRI images. It is important to note that with current MRI technology achieving the high signal quality and CT-like resolution necessary to accurately image ST and SV requires hours of scan time and the use of high field scanners not yet approved for clinical use, making use of MRI for large scale analysis of patient cochleae not yet a viable option. However, with future improvements to MRI technology it may become possible to fuse an MRI for pre-implantation imaging of the cochlea anatomy and a CT

for post-implantation localization of the CI electrodes to accurately quantify intra-cochlear electrode position.

Another approach is to create a model of intra-cochlear anatomy that can be registered to a patient CT image to define the location of the basilar membrane, modiolus, and other intra-cochlear structures, which are not directly visible in the images. This was the approach of Skinner et al.[7], who created a rigid model of cochlear anatomy using a high-resolution multi-section histological image of a single cochlear specimen where the fine structures of the cochlea can be visualized. Using a spatially aligned CT volume, this model could be rigidly registered to new patient CT images to estimate the position of the electrodes relative to the model-estimated position of the basilar membrane and other fine intra-cochlear structures. This model has been used in several studies to investigate the relationship between electrode position and hearing outcomes. In Skinner et al.[7] and Finley et al.[8], it was found that scalar location of the electrode array is correlated with hearing outcomes. Later in Holden et al.[9], it was found that in addition to scalar location, the distance of the electrode array to the modiolus is another factor that is predictive of outcomes. Depth of insertion into the cochlea is another factor that has been studied, but results are conflicting with some studies showing better outcomes are associated with deeper[10,11] or shallower[8,9] insertions. Thus, even with a model based approach, some factors such as distance to the modiolus have been little studied, and others such as depth of insertion led to conflicting findings. One potential reason for this is that using a single model that is rigidly registered to patient images does not provide an accurate enough estimation of the position of intra-cochlear anatomy. Indeed, this approach does not permit to take into account normal non-rigid inter-subject anatomical variations and thus leads to error when localizing anatomic structures. For example, consider using a square model to approximate a circle. Even with optimal rotation and translation

of the model, it never perfectly matches the circle in shape. Recent studies have shown that individual human cochleae differ not only in size but also in morphology[12–15]. Studying 73 ears, Erixon et al.[12] found large variations in cochlea dimensions, concluding that each cochlea was uniquely shaped. Avci et al.[13] also observed large variability across different measurements of cochlea, including height, width, length, and number of cochlear turns. Non-rigid variations, from the simplest variation of overall cochlea size to more complex variations such as changing proportions of specific areas (e.g., a deeper basal turn or a more horizontally positioned round window), cannot be captured by rotating or translating one geometric model to fit another and thus cannot be accounted for by rigid models.

A cochlear model that captures non-rigid variations in anatomy and that can be automatically and accurately aligned with new patient CT images has been proposed and developed by Noble et al.[16], and the authors have begun to use it to assess electrode placement and its effect on outcomes[17,18]. Consider the analogy of matching a square model to a circle above. With non-rigid transformation of the model, the square model can be warped to match the shape of the circle. Similarly, non-rigid models of the cochlea have the advantage of being able to be warped to more accurately match the shape of the target anatomy. When the non-rigid cochlea model was introduced by Noble et al.[16], it was shown that it more accurately estimates the position of intra-cochlear structures than a rigid model; however, the effect that the anatomy localization method, i.e., rigid versus non-rigid, has on the accuracy of electrode position measurements has not been quantified. In this study, we propose an approach to quantify the accuracy of measurements of intra-cochlear electrode positions when using rigid cochlear models. In future work, we plan to design a study to quantify measurement accuracy with non-rigid models which will require expanding our dataset as will be discussed in the conclusions section.

Another application of interest for which selection of an accurate cochlear model is important is image-guided CI programming (IGCIP)[19]. After CI surgery, each CI is programmed by an audiologist to attempt to optimize hearing performance. These programming sessions include deciding which electrodes will be activated, and assigning stimulation levels as well as sound frequency bands. With the intra-cochlear position of the electrodes unknown, audiologists have little quantitative information they can use to guide programming. Thus, they have to depend on the feedback that the patients provide to try to optimize the settings. However, the adjustment process often converges to suboptimal settings, and it requires several programming sessions over the course of many years. In IGCIP, the goal is to accurately identify the intra-cochlear location of the CI electrodes and to use that information to assist the audiologist in selecting better patient-customized programming settings. Previous studies have shown that this approach leads to significant improvement in hearing outcomes[20,21]. Since IGCIP depends on accurate localization of intra-cochlear electrode position for each patient, choosing an appropriate cochlear model is crucial.

2.2 Methods

We use a dataset of pre- and post-implantation CTs of 98 CI ears from 93 patients to quantify the accuracy of measurements of intra-cochlear electrode positions when using rigid cochlear models. Our approach is to 1) fit individual rigid models of cochlear anatomy we have created from seven different cochleae to each of the CI ears; 2) evaluate intra-cochlear electrode position in each ear relative to each of the seven models; and 3) quantify the errors because of non-rigid variations in cochlear anatomy as the differences in resulting measurement of electrode position across the seven different models. Our approach is described in detail in the following sections.

2.2.1. Dataset

Our model construction dataset consists of seven μCTs of cochlea specimens in which the ST, SV, and modiolus were manually segmented to create seven different rigid cochlea models. μCTs rather than CTs must be used because intra-cochlear structures are not visible in CT images as discussed in the introduction section. Figure 2.1 shows a cropped μCT image where ST, SV, and modiolus are represented with blue, yellow, and red contours, respectively.

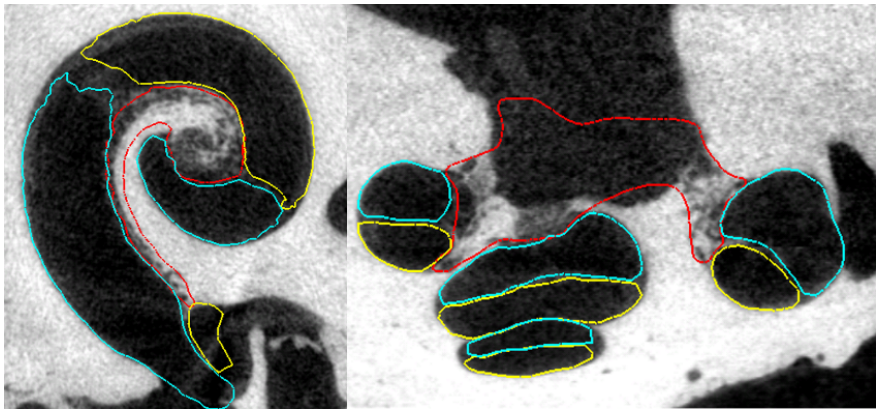

Figure 2.1. Two different view of a cropped μCT image where scala tympani (ST), scala vestibuli (SV), and modiolus are represented with light blue, yellow, and red contours, respectively.

Our testing dataset consists of pre- and post-implantation CTs for 98 ears of 93 CI patients. CT images were obtained with various scanners and parameters and had voxel size ranging from approximately $0.2x0.2x0.3mm^3$ to $0.4x0.4x0.4mm^3$. As a pre-processing step, we have implemented the approach of Noble et al.[16] to localize the ST, SV, and modiolus in the pre-implantation CT. We then localized the electrodes in the post-implantation CT[22–25], and rigidly registered the two CTs to bring the two datasets into alignment. Localizing the ST, SV, and modiolus in the preimplantation CTs facilitates an automatic approach for fitting each of the seven rigid models to the dataset as will be described below. Each pre-localization was visually inspected

in the preimplantation CT by an experienced Otolaryngologist, although it is not necessary for our pre-localizations to be extremely accurate for the analyses we describe below.

2.2.2. Model fitting

The seven rigid models represent the ST, SV, and modiolus as surfaces composed of a set of over 3,000 points distributed uniformly over the surfaces of these structures. Each of these points corresponds to a specific anatomical site that was semi automatically determined when the active-shape model of the cochlea was created[16].

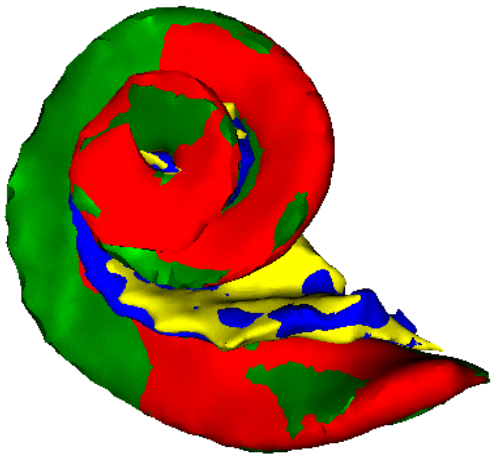

Figure 2.2. Rigidly model fitting result. Scala tympani (ST—red) and modiolus (blue) are the surfaces in the preimplantation CTs, and ST (green) and modiolus (yellow) belong to one of the rigid models.

Thus, the rigid models were created such that point correspondences exist not only across the models but also with the pre-localizations of the ST, SV, and modiolus in the testing dataset of 98 CI cases. Using these point correspondences, we automatically rigidly registered the seven models to each patient using well known point-based registration techniques[26]. All of the points that make up the ST, SV, and modiolus surfaces were used in the point-based registration. This method finds

the translation and the rotation that will be applied to a set of points to spatially align them with another set of points while minimizing the sum of squared errors between the point sets. As it is an error minimizing method, it is more accurate than manual registration done based on visual observation. Point-based registration also has the advantage that it guarantees a solution that globally minimizes the surface error, as opposed to techniques such as image-based registration, where the image intensity-based error minimizing procedure could fall into a local minima and cause alignment errors. By using our point registration approach in which the models are registered to a reference in an unbiased way, we minimize the possibility that the differences we measure in relative electrode position across models are because of model alignment errors. Figures 2.2 and 2.3 show an example result of this process.

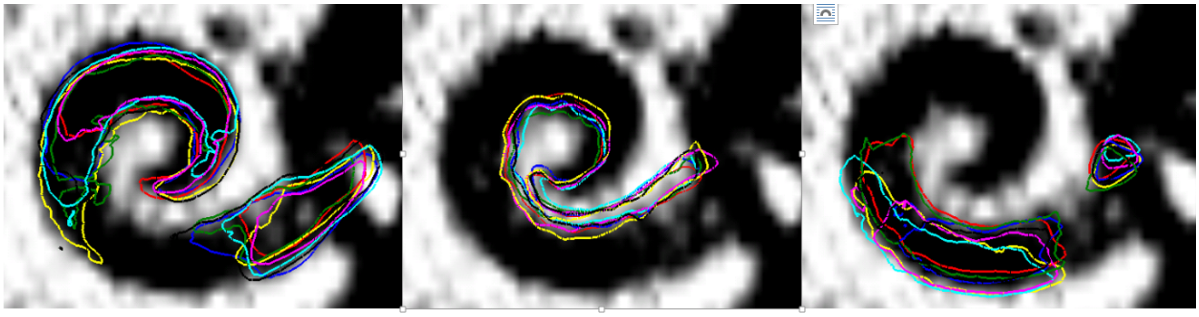

Figure 2.3. Segmentation of anatomical structures using seven different rigid models are represented with seven different colors. Scala tympani (ST) on the left, scala vestibuli (SV) in the middle, and modiolus on the right.

2.2.3. Relative electrode position

In order to measure the relative position of the electrodes with respect to the basilar membrane, we first use the ST and SV to define a "basilar membrane curve," or BMC for short, which is a curve that lies along the length of the cochlea on the basilar membrane, between the ST and the SV, and located midway between the modiolus and the lateral wall of the cochlea. The BMC is shown in white on Figure 2.4 where the ST and the SV are shown as blue and green 3D meshes,

respectively.

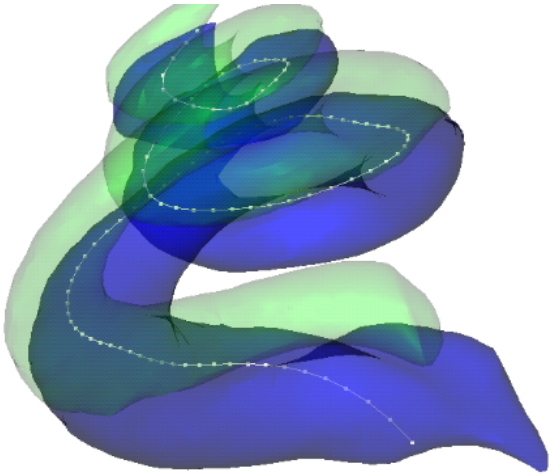

Figure 2.4. The basilar membrane curve (BMC) that separates scala tympani (ST) and scala vestibuli (SV) is shown in white. ST and SV are shown as blue and green 3-D meshes, respectively.

At each point ***c*** along the BMC, a vector, ***m***, that points from ***c*** towards the mid-modiolar axis can be found. Next, a vector ***s***, which is perpendicular to both ***m*** and the tangent of the BMC at ***c*** can be found. The mid-modiolar axis and the ***m*** and ***s*** vectors found along the length of the BMC for one case are shown in Figure 2.5 in red, light blue, and yellow, respectively.

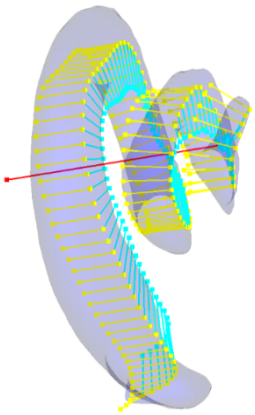

Figure 2.5. Scala tympani (ST) is shown as the blue 3-D mesh. Midmodiolar axis, m and s vectors are in red, light blue, and yellow, respectively.

Using the BMC and these vectors, we can measure the intra-cochlear location of each electrode. For each electrode, first, the closest point ***p*** along the BMC is found. Then, the depth of insertion of the electrode can be found by measuring the geodesic distance, i.e., the distance along the BMC between ***p*** and the round window (RW). The geodesic distance is calculated as the sum of Euclidian distances of each line segment that defines the BMC between RW and ***p***. Next, the modiolar distance of the electrode is found by measuring the distance to the electrode along the vector ***m*** associated with BMC point ***p***. Finally, the scalar location of the electrode relative to the basilar membrane is found by measuring the position of the electrode along the ***s*** vector associated with BMC point ***p***. Because ***p*** lies on the basilar membrane and ***s*** is defined to be normal to the basilar membrane, electrodes that are found to be in the positive ***s*** direction relative to ***p*** are located in the ST, and those that are found to be in the negative ***s*** direction are located in the SV.

2.2.4. Cochlear duct length at 2 turns

The cochlear duct length (CDL) is another quantity of interest for CI as its measurement has been proposed as an approach for pre-operative patient-specific selection of the electrode array. Measurement of CDL using a rigid model would not be useful because it would be measured identically for each patient. However, herein we report the standard deviation of the length of the cochlear duct at a depth of two turns across rigid models as an indicator for inter-subject variations in CDL.

2.3. Results

Standard deviation across rigid models in measures of electrode location relative to the basilar membrane was 0.11 mm. We also counted the number of times the rigid models were in unanimous

agreement about the scala in which each electrode was located. Out of 1834 electrodes, the models were in agreement for 1348 electrodes being in ST and 133 electrodes being in SV. The models did not unanimously agree for 353 electrodes.

Standard deviation across rigid models in measures of distance to the modiolus was 0.15 mm. Electrodes found to sit more than 0.3 mm from the BMC towards the modiolus were considered to be close to the modiolus and labelled as group *I* electrodes. Those found to sit more than 0.3 mm from the BMC towards the lateral wall of the cochlea were considered far from the modiolus and labelled as group *III* electrodes. All other electrodes were considered as sitting a medium distance to the modiolus and labelled as group *II* electrodes. We found that out of 1834 electrodes, the rigid models unanimously agreed on 326 electrodes as belonging to group *I*, 169 as belonging to group *II*, and 426 as belonging to group *III*. The models did not agree on the remaining 913 electrodes.

Average standard deviation across rigid models in measurement of electrode depth within the cochlea was found to be 0.68 mm. We found the standard deviation in CDL across rigid models to be 1.54mm.

2.4. Conclusions

The primary aim of this study was to quantify the performance of rigid models in measuring intra-cochlear electrode position. Quantifying intra-cochlear position of CI electrodes is important for studying the relationship between electrode position and hearing outcomes. It is also important for image-guided cochlear implant programming techniques that rely on measurements of electrode positions to determine patient-customized programming settings. Rigid models are commonly used for measuring intra-cochlear electrode position, but the accuracy of electrode position

measurements when using a rigid model has not been widely studied. Rigid models of anatomy are limiting because they are aligned by simple rotation and translation and assume identical size and proportions of the cochlea exist between patients. This approach is effective if the assumptions are met but fails when there are substantial inter-patient differences.

In this study, we compared measurements of intra-cochlear electrode position on 93 subjects when using 7 different rigid models. Standard deviations of electrode position measures across rigid models are relatively high, leading to potentially different findings about the scalar position of electrodes and their proximity to the modiolus depending on which rigid model is used. The rigid models disagreed on scalar position for 19% of the electrodes in our dataset and on modiolar proximity for 50% of the electrodes. The error minimizing approach we used to align the rigid models ensures that we have minimized the likelihood that the disagreements we observe in measurements of electrode position are due to misalignment of the rigid models. These results motivate the use of non-rigid models of cochlear anatomy, such as that proposed by Noble et al.[16], when measuring intra-cochlear electrode position as they have been shown to be more accurate than rigid ones. It was not possible in this study to similarly analyze variability in non-rigid models because it was not possible to create multiple unique non-rigid models to compare to each other. However, in future work, we plan to collect μCTs of a large number of implanted cochlea specimens which will facilitate more direct measurement of errors in electrode positioning using both rigid and non-rigid models.

References

1. Aschendorff A, Kubalek R, Hochmuth A, et al. Imaging procedures in cochlear implant patients--evaluation of different radiological techniques. *Acta Otolaryngol Suppl*. 2004;(552):46-49.

2. Aschendorff A, Kubalek R, Turowski B, et al. Quality control after cochlear implant surgery by means of rotational tomography. *Otol Neurotol*. 2005;26(1):34-37.

3. Verbist BM, Frijns JHM, Geleijns J, van Buchem MA. Multisection CT as a valuable tool in the postoperative assessment of cochlear implant patients. *AJNR Am J Neuroradiol*. 2005;26(2):424-429.

4. Boyer E, Karkas A, Attye A, Lefournier V, Escude B, Schmerber S. Scalar localization by cone-beam computed tomography of cochlear implant carriers: a comparative study between straight and periomodiolar precurved electrode arrays. *Otol Neurotol*. 2015;36(3):422-429. doi:10.1097/MAO.0000000000000705

5. van Egmond SL, Visser F, Pameijer FA, Grolman W. Ex vivo and in vivo imaging of the inner ear at 7 Tesla MRI. *Otol Neurotol*. 2014;35(4):725-729. doi:10.1097/MAO.0000000000000276

6. Neri E, Berrettini S, Salvatori L, Forli F, Franceschini SS, Bartolozzi C. 3-D CT and MRI co-registration in the assessment of cochlear implantation. *Med Sci Monit*. 2005;11(10):MT63-67.

7. Skinner MW, Holden TA, Whiting BR, et al. In vivo estimates of the position of advanced bionics electrode arrays in the human cochlea. *Ann Otol Rhinol Laryngol Suppl*. 2007;197:2-24.

8. Finley CC, Holden TA, Holden LK, et al. Role of electrode placement as a contributor to variability in cochlear implant outcomes. *Otol Neurotol*. 2008;29(7):920-928. doi:10.1097/MAO.0b013e318184f492

9. Holden LK, Finley CC, Firszt JB, et al. Factors affecting open-set word recognition in adults with cochlear implants. *Ear Hear*. 2013;34(3):342-360. doi:10.1097/AUD.0b013e3182741aa7

10. Skinner MW, Ketten DR, Holden LK, et al. CT-derived estimation of cochlear morphology and electrode array position in relation to word recognition in Nucleus-22 recipients. *J Assoc Res Otolaryngol*. 2002;3(3):332-350. doi:10.1007/s101620020013

11. Yukawa K, Cohen L, Blamey P, Pyman B, Tungvachirakul V, O'Leary S. Effects of insertion depth of cochlear implant electrodes upon speech perception. *Audiol Neurootol*. 2004;9(3):163-172. doi:10.1159/000077267

12. Erixon E, Högstorp H, Wadin K, Rask-Andersen H. Variational anatomy of the human

cochlea: implications for cochlear implantation. *Otol Neurotol*. 2009;30(1):14-22. doi:10.1097/MAO.0b013e31818a08e8

13. Avci E, Nauwelaers T, Lenarz T, Hamacher V, Kral A. Variations in microanatomy of the human cochlea. *J Comp Neurol*. 2014;522(14):3245-3261. doi:10.1002/cne.23594

14. Verbist BM, Ferrarini L, Briaire JJ, et al. Anatomic considerations of cochlear morphology and its implications for insertion trauma in cochlear implant surgery. *Otol Neurotol*. 2009;30(4):471-477. doi:10.1097/MAO.0b013e3181a32c0d

15. Pelosi S, Noble JH, Dawant BM, Labadie RF. Analysis of intersubject variations in intracochlear and middle ear surface anatomy for cochlear implantation. *Otol Neurotol*. 2013;34(9):1675-1680. doi:10.1097/MAO.0b013e3182a1a7e6

16. Noble JH, Labadie RF, Majdani O, Dawant BM. Automatic segmentation of intracochlear anatomy in conventional CT. *IEEE Trans Biomed Eng*. 2011;58(9):2625-2632. doi:10.1109/TBME.2011.2160262

17. Wanna GB, Noble JH, Carlson ML, et al. Impact of electrode design and surgical approach on scalar location and cochlear implant outcomes. *Laryngoscope*. 2014;124 Suppl 6:S1-7. doi:10.1002/lary.24728

18. Wanna GB, Noble JH, McRackan TR, et al. Assessment of electrode placement and audiological outcomes in bilateral cochlear implantation. *Otol Neurotol*. 2011;32(3):428-432. doi:10.1097/MAO.0b013e3182096dc2

19. Noble JH, Labadie RF, Gifford RH, Dawant BM. Image-guidance enables new methods for customizing cochlear implant stimulation strategies. *IEEE Trans Neural Syst Rehabil Eng*. 2013;21(5):820-829. doi:10.1109/TNSRE.2013.2253333

20. Noble JH, Gifford RH, Hedley-Williams AJ, Dawant BM, Labadie RF. Clinical evaluation of an image-guided cochlear implant programming strategy. *Audiol Neurootol*. 2014;19(6):400-411. doi:10.1159/000365273

21. Noble JH, Hedley-Williams AJ, Sunderhaus L, et al. Initial Results With Image-guided Cochlear Implant Programming in Children. *Otol Neurotol*. 2016;37(2):e63-69. doi:10.1097/MAO.0000000000000909

22. Zhao Y, Dawant BM, Labadie RF, Noble JH. Automatic localization of cochlear implant electrodes in CT. *Med Image Comput Comput Assist Interv*. 2014;17(Pt 1):331-338.

23. Noble JH, Dawant BM. Automatic graph-based localization of cochlear implant electrodes in CT. *Med Image Comput Comput Assist Interv*. 2015;9350:152-159.

24. Zhao Y, Chakravorti S, Labadie RF, Dawant BM, Noble JH. Automatic graph-based method for localization of cochlear implant electrode arrays in clinical CT with sub-voxel accuracy. *Med Image Anal*. 2019;52:1-12. doi:10.1016/j.media.2018.11.005

25. Zhao Y, Dawant BM, Labadie RF, Noble JH. Automatic localization of closely spaced cochlear implant electrode arrays in clinical CTs. *Med Phys*. 2018;45(11):5030-5040. doi:10.1002/mp.13185

26. Wahba G. A Least Squares Estimate of Satellite Attitude. *SIAM Rev*. 1965;7(3):409-409. doi:10.1137/1007077

Chapter III

AUTOMATIC COCHLEAR DUCT LENGTH ESTIAMTION FOR SELECTION OF COCHLEAR IMPLANT ELECTRODE ARRAYS

Alejandro Rivas[2], Ahmet Cakir[1] (co-first authorship), Jacob B. Hunter[2], Robert F. Labadie[2], M. Geraldine Zuniga[2], George B. Wanna[2], Benoit M. Dawant[1], Jack H. Noble[1]

[1]Department of Electrical Engineering and Computer Science, Vanderbilt University, Nashville, TN 37232

[2]Department of Otolaryngology-Head and Neck Surgery, Vanderbilt University Medical Center, Nashville, TN 37232

Abstract

Hypothesis: Cochlear duct length (CDL) can be automatically measured for custom selection of cochlear implant (CI) electrode arrays.

Background: CI electrode array selection can be influenced by measuring the CDL, which is estimated based on the length of the line that connects the round window and the lateral wall of the cochlea when passing through the modiolus. CDL measurement remains time consuming and inter-observer variability has not been studied.

Methods: We evaluate an automatic approach to directly measure the two-turn (2T) CDL using existing algorithms for localizing cochlear anatomy in computed tomography (CT). Pre-op CT images of 309 ears were evaluated. Two fellowship-trained neurotologists manually and independently measured CDL. Inter-observer variability between measurements across experts and automatic observers is assessed. Inter-observer differences for choice of electrode type are also investigated.

Results: Manual measurement of CDL by experts tends to underestimate cochlea size and has high inter-observer variability, with mean absolute differences between expert CDL estimations of 1.15 mm. Our results show that this can lead to a large number of cochleae for which a different electrode array type would be selected by different observers.

Conclusion: Choosing the best CI electrode array is an important task for optimizing hearing outcomes. Manual cochleae length measurements are user-dependent, and errors impact upon the CI electrode array choice for certain patients. Measuring cochlea length automatically is less time consuming and generates more repeatable results. Our automatic approach could make use of CDL for patient-customized treatment more clinically adoptable.

3.1 Introduction

The human cochlea and cochlear duct, defined as the length of the scala media, are fully formed at birth. In 1938, Hardy first reported the histologic measurements of the cochlear duct length (CDL) in 68 cadaveric specimens via graphic reconstructions of serial sections, measuring from the middle of the round window to the helicotrema[1]. Since the advent of cochlear implantation, multiple studies have assessed the role of using the CDL to determine the appropriate electrode length for implantation. This is particularly important as the length of the cochlea can vary between 25 – 45 mm in patients[2–12].

Several studies have demonstrated that greater angular insertion depths result in improved speech perception performance[13–16]. Since the angular depth of insertion is dependent upon CDL and the length of the implanted electrode, the variability in CDL and electrode options can influence speech perception performance. In addition, as evidence suggests atraumatic cochlear implantation preserves residual hearing and postoperative performance, knowing the correct CDL

is of paramount importance to ensure trauma caused by over-insertion (e.g. scalar translocation) is avoided.

Recently, building on the work of Hardy[1] and others[8], Alexiades et al. described a simplified formula to calculate CDL at a given angular depth using computerized tomography (CT) and by measuring the distance from the middle of the round window (RW) to the farthest point on the opposite wall of the cochlea, denoted A[17]. However, this method remains time consuming and operator dependent, and intra- or inter-observer variability in measurements have not been studied.

Thus, herein we have developed an automatic method to measure both A and CDL at a given angular depth using an active-shape-model-based, automatic cochlea segmentation technique[18]. In the current work, we assess the inter-observer variability by computing differences between measurements of A across expert observers. We also compare expert measurements to automatic measurements of A, and investigate the sensitivity of the choice of electrode type to the choice of CDL measurement method by counting how often the choice of electrode would differ when different expert or automatic measures are used to estimate CDL.

3.2 Methods

After Institutional Review Board approval, we retrospectively reviewed a CT imaging database to identify 275 pre-operative CT scans that were available for review for adult patients who underwent cochlear implantation. As described in the following sub-sections, CDL was measured in each of these CTs using manual and automatic measurement methods.

3.2.1. Cochlear duct length from *A*

Previous literature has shown that *A,* the length of the line from the center of the round window (RW) through the modiolus to the farthest point on the lateral wall of the basal turn of the cochlea, can be used to calculate the length of the cochlear duct along the outer wall of the cochlea from the center of the RW to a specified angular depth[19]. The formula is defined as follows:

$$\mathrm{CDL}(A,\theta) = 2.62\ A\ \log_e\left(1.0 + \frac{\theta}{235°}\right) \qquad (3.1)$$

where θ is the angular depth within the cochlea at which we want to estimate the CDL. The angular depth of a point in the cochlea is defined as proposed by Verbist et al[20]. It is measured using the position of the mid-modiolar axis and the center of the round window membrane, as shown in Figure 3.1, which are found automatically using the automatic image processing methods described below.

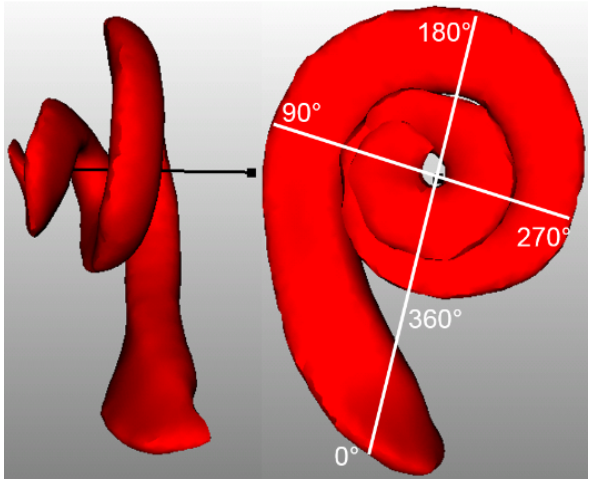

Figure 3.1. Explanation of angular depth. Scala tympani is shown in red and mid-modiolar axis is shown in black. Round window (RW) is marked with 0 degree.

The middle of the round window membrane defines the 0° depth, and the angular depth of a point is measured as its angle around the mid-modiolar axis along the length of the cochlea spiral relative

to the round window reference angle. 0° to 360° corresponds to the first turn of the cochlea, 360° to 720° corresponds to the second turn, etc. The angular depth where the cochlear duct ends is approximately 2.5 turns but this varies across subjects. Since advancement of the arrays past 2 turns (2T) is rare, and estimation of CDL at 2T is more reliable than that of the full CDL[17], in this work we choose to estimate CDL at 2T rather than the full CDL. Measuring CDL along the outer wall of the cochlea to a depth of 2T implies θ = 720°, and thus Equation 3.1 simplifies to 2.62A $\log_e(1.0 + \frac{720}{235})$ = 3.67A. Further, Alexiades et al. showed that Equation 3.1 could be modified to calculate the length an electrode array with average diameter *d* would need to have to reach a specified depth as[17]:

$$\mathrm{E}(A, \theta, d) = 2.62\ (A - d)\ \log_e\ (1.0 + \frac{\theta}{235°}) \qquad (3.2)$$

3.2.2. Manual Measurement of *A*

Manual measurement of patient-specific *A* values was done using a software package developed in-house that allows for rotation of the CT volume to create oblique axial, coronal, and sagittal reconstructions as well as 3D views and permits selecting the RW and lateral wall points. Two fellowship-trained neurotologists independently reviewed each patient's imaging study, identifying the RW and the farthest point on the opposite wall of the cochlea for which a straight line could be drawn through the modiolus. The manually measured *A* values were denoted as A_{S1} for surgeon 1 and A_{S2} for surgeon 2. An example result of this process is shown in Figure 3.2. Using Equation 3.1 with $\theta = 720°$, the CDL along the outer wall at 2T can be computed for both A_{S1} and A_{S2}, and these quantities are denoted as CDL_{S1} and CDL_{S2}, respectively.

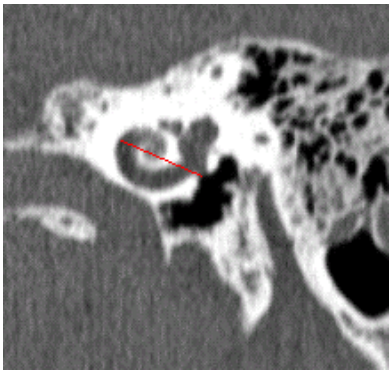

Figure 3.2. Example of manual selection of A.

3.2.3. Automatic measurement of *A*

Automatic segmentation of the cochlea was achieved by implementing the model fitting-based approach described by Noble et al., which was shown to localize highly accurate surface models of cochlear anatomy in patient CTs[18,21]. This method permits accurately identifying anatomical sites anywhere on the surface of the cochlea. Thus, we used this approach to automatically identify a point on the middle of the RW and another point on the lateral wall of the first turn of the cochlea that is farthest from the RW. We then computed the distance between these two points for each patient. The automatically measured *A* values were denoted as A_{Auto}. All automatic cochlea segmentations were visually inspected in the patient CT image and confirmed to be accurate. Using Equation 3.1, the corresponding CDL at 2T can be computed for A_{Auto} as $CDL_{A\text{-}Auto}$.

3.2.4. Automatic direct measurement of CDL at 2T

In addition to computing the CDL at 2T automatically as $CDL_{A\text{-}Auto}$ by using Equation 3.1 with A_{Auto}, we can also use the automatic segmentation method to directly measure the CDL at 2T. Points along the outer wall of the cochlea along the CD were identified in the cochlea model to form the model CD curve. These points were automatically mapped to each patient CT using the

model[22]. Then for each patient, we directly measure the outer wall CDL at 2T, $CDL_{Direct\text{-}Auto}$, by computing the length of the CDL curve defined by the model from RW to an angular depth of 2T.

3.2.5. Effect of CDL measurement approach on selection of array type

While many factors go into the decision about what electrode array is most suitable for a patient, we investigated whether the choice of CDL measurement could affect selection of the electrode array when only CDL is considered. To do this, we assessed how often CDL measurement would result in a different choice of electrode array between two array types, the Med-El (Innsbruck, Austria) $Flex24^{TM}$ (Array 1) and $Flex28^{TM}$ (Array 2). Array 1 and Array 2 both have 12 electrodes and average diameter of approximately 0.6 mm, and lengths of 24 and 28 mm, respectively. With lateral wall arrays, studies have shown a trend of deeper implantation being associated with better outcomes, suggesting that in general longer arrays are better, although several additional factors should be considered when selecting the electrode array. A smaller CDL warrants a shorter electrode to ensure the base of the array can be fully inserted and all basal electrodes are available for stimulation. Basal contacts that are too shallow and lie either near the entrance of the cochlea or outside the cochlea typically provide ineffective stimulation due to lack of access to neural populations. Such contacts are sometimes deactivated during cochlear implant (CI) programming but often are left at default values due to adequate volume perception potentially leading to sub-optimal hearing outcomes by interfering with other electrodes. On the other hand, a larger CDL warrants a longer electrode to ensure the tip of the array can reach apical stimulation sites which has also been shown to be important in maximizing audiological outcomes[16]. Given that there has been little evidence on what electrode depth is best for optimal hearing outcomes, the specific threshold value of *A* (*thresh-A*) used to decide between Array 1 and Array 2 is a matter

of surgeon preference. Thus, in this work, we aim to show how often the choice of array would differ over a range of choices of *thresh-A* across different techniques for measuring cochlea size when only cochlea size is used to make this decision. We tested the range of values of *thresh-A* from 8 mm (*CDL* at 2T = 29.54 mm) to 10.25 mm (*CDL* at 2T = 37.66 mm) as this matches the range of *A* values in our dataset. The different measures of cochlea size described in the previous sub-sections, CDL_{S1}, CDL_{S2}, $CDL_{A\text{-}Auto}$, and $CDL_{Direct\text{-}Auto}$ were each used to estimate *A* for each case. Then, for each value of *thresh-A*, we counted how many times the different measures of cochlea size would lead to a different choice in the array that is selected.

3.2.6. Statistical analysis

Continuous features were described with means, ranges, and standard deviations. Analysis of variance (ANOVA) with post-hoc comparison analysis was performed to compare means. Inter-observer variability in measurement of cochlea size were assessed with mean differences, mean absolute differences, and maximum absolute differences. Fisher's exact tests were used to determine if measurement techniques influenced appropriate electrode selection. *p*-values less than 0.05 were considered statistically significant.

3.3 Results

The mean, range, and standard deviations for length *A* for A_{Auto}, A_{S1} and A_{S2} are shown in Table 3.1. A one-way repeated measures ANOVA revealed significant differences between the three different measurement means for the 309 ears ($p < 0.001$).

Post-hoc analyses were conducted in order to assess the significant difference between each of the measurements. The three paired t-tests revealed that the means were significantly different

($p<0.001$) between each pair of measurements.

Table 3.1. Maximum, minimum, mean, and standard deviation across automatically and manually measured A values. A_{Auto} indicates automatically measured A values; A_{S1}, surgeon 1; A_{S2}, surgeon 2.

	Maximum (mm)	Minimum (mm)	Mean ± standard deviation (mm)
A_{Auto}	10.25	8.04	9.22 ± 0.44
A_{S1}	11.56	7.58	8.91 ± 0.49
A_{S2}	10.99	7.97	9.00 ± 0.46

The mean difference, mean absolute difference, and the maximum absolute difference between the manual measurements A_{S1} and A_{S2} were, 0.06 mm, 0.18 mm, and 2.18 mm, respectively. The same measurements between A_{Auto} and A_{S1} were 0.18 mm, 0.25 mm, and 1.92 mm, and between A_{Auto} and A_{S2} were 0.12 mm, 0.18 mm, and 1.92 mm, respectively.

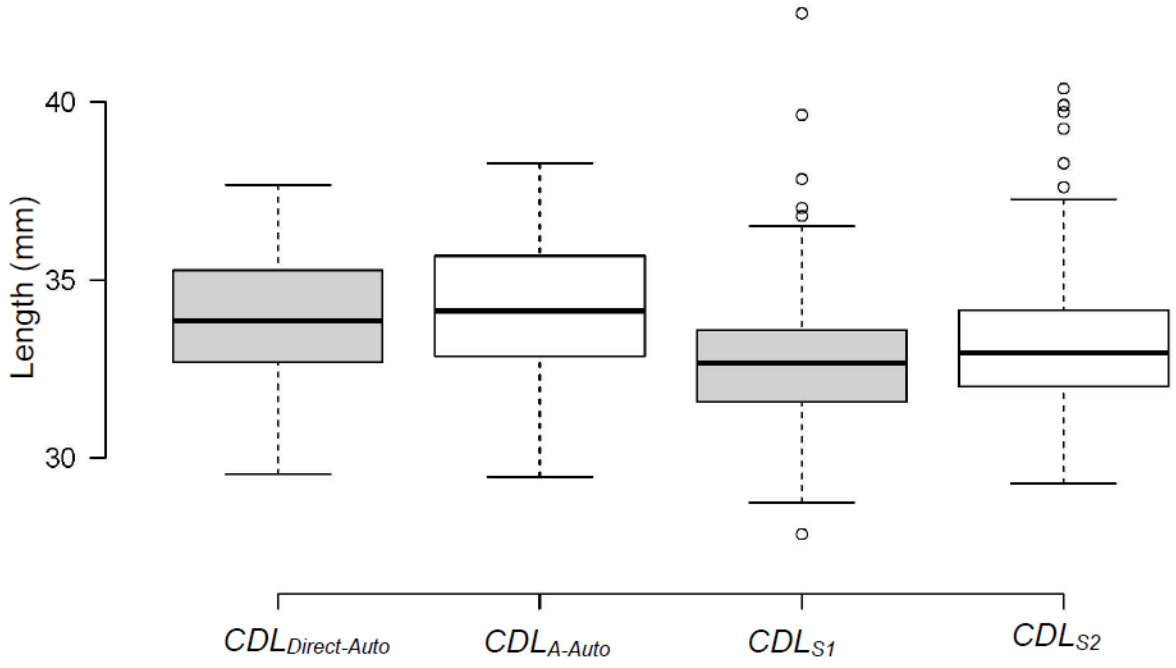

Figure 3.3. Boxplots of the automatically measured and the estimated CDL. CDL indicates cochlear duct length.

The mean and standard deviations for CDL_{S1}, CDL_{S2}, $CDL_{A\text{-}Auto}$, and $CDL_{Direct\text{-}Auto}$ were 32.71 ± 1.80, 33.07 ± 1.69, 33.87 ± 1.61, and 34.14 ± 1.75 mm, respectively. A box plot of these measurements is displayed in Figure 3.3 where each of the box-plot represents a different measurement. In each boxplot, the box represents the inter-quartile range, the black line is the median, values that fall 1.5 times the interquartile range above the third quartile or below the first quartile are considered outliers and shown as circles, and the "whiskers" at the bottom and at the top represent the minimum and the maximum values excluding the outliers, respectively. Comparing the means, an ANOVA test revealed a significant difference between the four measurement means ($p < 0.001$). Post-hoc analyses were conducted.

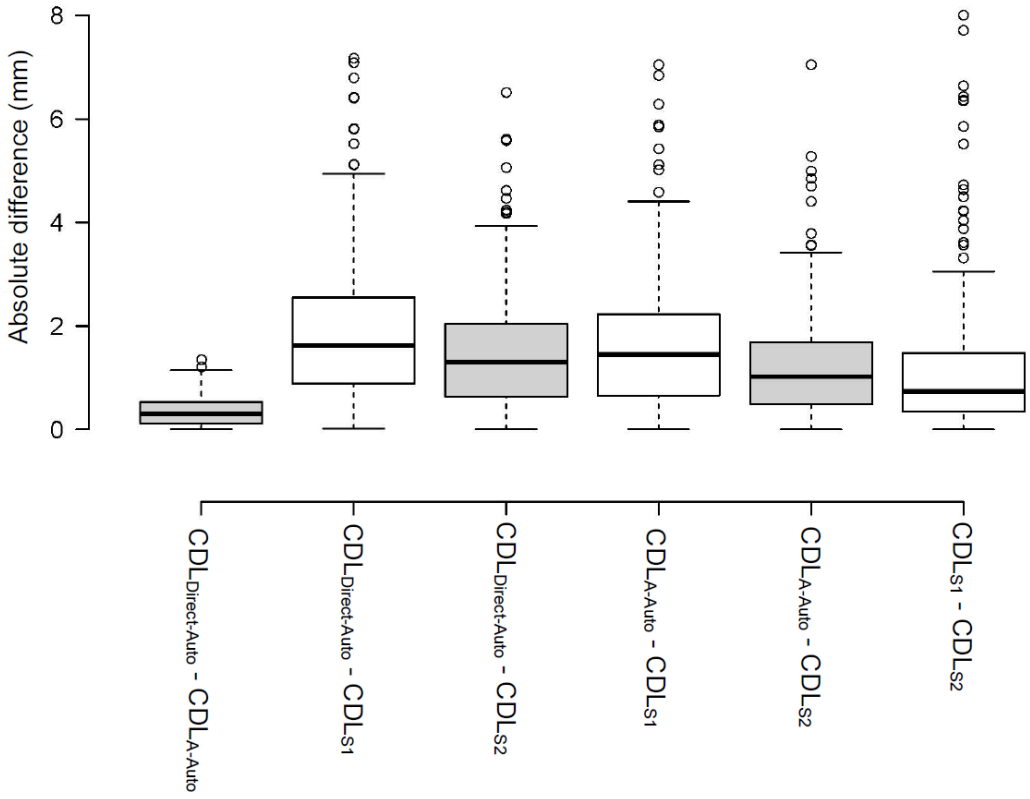

Figure 3.4. Boxplots of the difference between all of the four different cochlear duct length (CDL) values.

The paired t-tests between the six combinations of measures showed that each pair of measurements were significantly different ($p < 0.001$). Figure 3.3 illustrates that manually measuring *A* tends to underestimate *A* in comparison to automated techniques, resulting in an underestimation of the CDL. A comparison between different CDL measurements is shown in Figure 3.4 where each boxplot represents the absolute values of the differences between various CDL measurements.

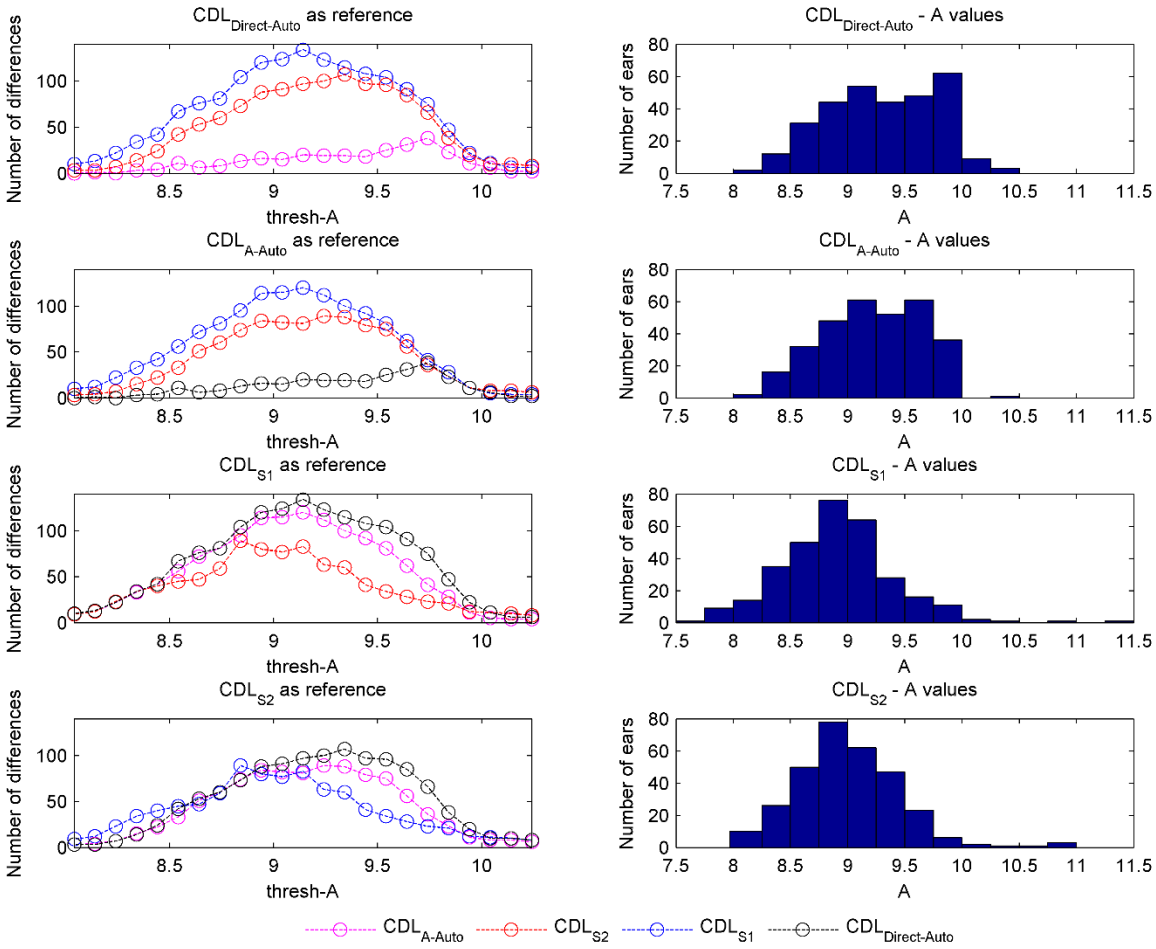

Figure 3.5. Panels in the left column show the number of times the selected electrode arrays differed among measurement methods for different values of thresh-A. Right columns show histograms of cochlea size across subjects using each measurement technique.

In the left column of Figure 3.5, each panel corresponds to one measurement technique and shows the number of ears for which a different electrode array would be selected when using each other measurement method to measure *A* across the range of values of *thresh-A*. In the right column of Figure 3.5, a histogram of cochlea size across subjects is shown as measured using each of the measurement techniques. Equation 3.1 was used to map values between CDL at 2T and *A*. It is clear from the two upper plots in the left column that using $CDL_{Direct\text{-}Auto}$ or $CDL_{A\text{-}Auto}$ measurements resulted approximately in the same electrode array type selections, with the biggest difference of 38 ears out of 309 occurring at a *thresh-A* of 9.74 mm. Automated techniques to measure length *A* and CDL did not lead to significant differences in the selected electrode array type for any value of *thresh-A* smaller than 9.5 mm ($p > 0.68$). Manual measurements by the first and second surgeon, on the other hand, led to a larger number of differences in the selected electrode array type between each other and the automated measures, as observed in Figure 3.5. The selections by the first surgeon were significantly different than the selections by the $CDL_{Direct\text{-}Auto}$ for all values of *thresh-A* smaller than 10 mm ($p < 0.015$). When comparing selections based on measurements done by the second surgeon with those by CDL_{Direct_Auto}, Fisher's exact test revealed statistically significant differences between these two selections for *thresh-A* greater than 8.34 and smaller than 9.84 mm ($p < 0.02$).

3.4 Discussion

Several studies have documented a correlation between the angular depth of insertion and speech performance outcomes following cochlear implantation[13-16]. The angular depth of insertion is dependent on CDL and length of the electrode array[12-17]. Choosing the appropriate length CI electrode array could ensure the desired angular depth of insertion, which in turn can improve

postoperative hearing outcomes. The importance of the relationship between CDL and electrode length deals with cochlear coverage. An ideal electrode covers the entire frequency spectrum of the cochlea. Electrodes that are too short fail to reach the apical cochlea, possibly leading to poorer patient outcomes. On the other hand, electrodes that are too long may lead to cochlear trauma, leading to poorer patient outcomes; or under-insertion at the basal end, leading to a loss of coverage of the high-frequency spectrum also leading to poorer outcomes. Thus, an ideal fit between the electrode and the CDL is desired. Given these findings, determining the CDL and selecting the most appropriately sized electrode is important in maximizing patient benefit. Nonetheless, while several studies have described techniques in determining CDL, these techniques remain burdensome and time consuming with unknown intra-and inter-observer variability. Thus, we developed an automatic method measuring both length *A* and 2T CDL using an automatic model-based segmentation technique and compared it to previous reported techniques.

The results presented herein will permit weighing the importance of choice of measurement method when using cochlear size to choose between different array lengths for a specific subject and choice of *thresh-A*. Our long-term goal is to develop a system to assist with patient-customized selection of electrode arrays using comprehensive information including but not limited to the patient's CDL. In ongoing investigation, preliminary results indicate that a reasonable choice for *thresh-A* would be 8.5 mm. To arrive at this value, we have reviewed post-implantation CTs of 10 subjects in our CT imaging database who were implanted by multiple surgeons and with Array 2. We found that the base of the array was not fully inserted in 7 cases, leaving the most basal contact(s) ineffective. Further advancement of the array was not done due to the perception of resistance to avoid the risk of trauma. We speculate that deeper angular depths increase the likelihood resistance is encountered due to the increased redirection of forces necessary to advance

the array as the coiling of the array increases (i.e. additive frictional forces as more of the electrode array abuts against intra-cochlear anatomy).

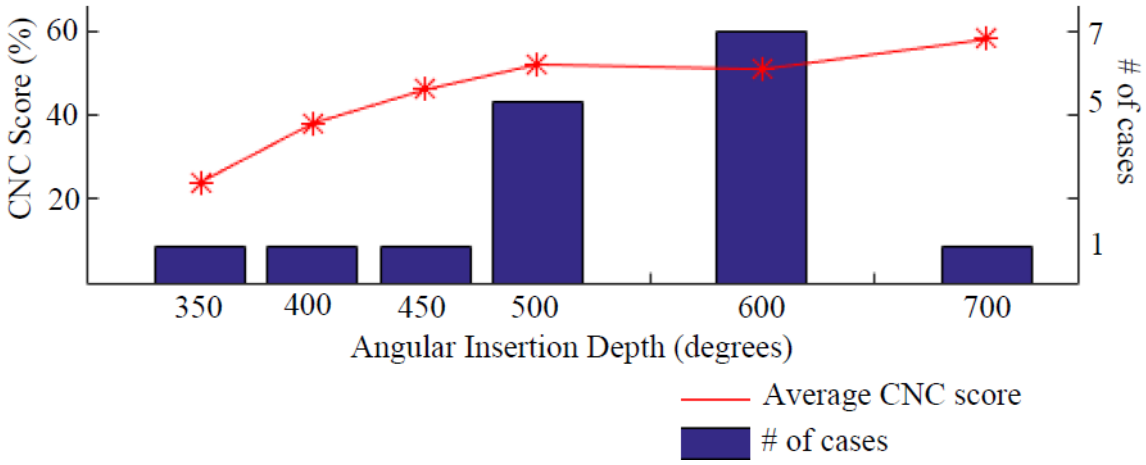

Figure 3.6. Angular Insertion depth measurements in relation to CNC word scores for 16 subjects

The average depth of the apical electrode across these 10 cases was 560°, thus we assume this is the angular depth at which resistance is encountered for the average cochlea. To establish a minimum target insertion depth, we further examined insertion depth in relation to CNC word scores for 16 subjects including the 10 subjects implanted with Array 2 mentioned above as well as other subjects implanted with long electrodes from the same manufacturer. These data are shown in Figure 3.6. As seen in the red curve in the figure, the trend is that increasing angular depth is associated with better CNC scores, however that trend appears to plateau once the insertion depth passes 450 degrees, suggesting that this insertion depth is deep enough to expect maximal outcomes. Thus, our strategy would be to choose *thresh-A* such that the array we select is long enough to at least reach a 450 degree depth at full insertion and is short enough to permit having all basal electrodes inserted into the cochlea when the tip insertion depth reaches 560 degrees. At *thresh-A* = 8.5 mm, Equation 3.2 predicts the length of the intra-cochlear path of Array 2 to reach

560° depth to be 25 mm for cochleae of that size. For the reader's reference, angular insertion depths predicted by Equation 3.2 for Array 1 and Array 2 for cochleae of different sizes are shown in Figure 3.7 for "full-insertion," where the depth marker on the array reaches the RW, as well as for an insertion where the 12th electrode is located at RW, denoted as "under-insertion." The lengths of the electrode arrays between the tip and the 12th electrode are approximately 21 mm and 24 mm, for Array 1 and Array 2, respectively. Thus, insertion depth for a full-insertion Array 1 and for an under-insertion Array 2 is the same, as shown in the figure. Since Array 2 is 28 mm in length with contacts distributed on the apical 24 mm of that length, it is likely that the array will be under-inserted at the base for cochleae that are smaller than *A*=8.5mm. For smaller cochlea, it is reasonable to consider Array 1 instead. At full-insertion, Array 1 would be predicted to reach 515°, which is deep enough that we would not expect a detriment to outcomes due to lack of insertion depth. For cochleae with *A* greater than 8.5 mm, Array 2 would be the preferred choice to ensure greater insertion depths can be reached. From Figure 3.5, it can be seen that Array 2 would be selected in 291/309 cases when using $CDL_{A\text{-}Auto}$, and it can be seen that the choice of array would differ in 53 and 30 of the 309 cases when using CDL_{S1} and CDL_{S2}. For cochleostomy (C) insertion on the other hand, *thresh-A* = 9 mm (CDL at 2T = 33.1 mm) could be used as the intra-cochlear path of the array will be around 1.5 mm shorter for cochleostomy insertions, and thus the *thresh-A* value needs to be appropriately adjusted. With *thresh-A* = 9 mm, Figure 3.5 shows that Array 2 would be selected in 211/309 cases when using $CDL_{A\text{-}Auto}$, and it can be seen that the choice of array would differ in 115 and 80 of the 309 cases when using CDL_{S1} and CDL_{S2}. Future temporal bone studies would be necessary to assess the effectiveness of these choices for *thresh-A*.

While Escude et al. described the length of the cochlear lateral wall based on the length

A^{19}, we noted significant inter-observer variability between manual measurements conducted by fellowship trained neurotologists. When we automated the measurement, we noted further significant differences between all three measurements. Rather than continuing to measure an indirect metric of CDL, we automatically segmented CDL and measured its length directly. There were significant differences between the automatic CDL measure and the calculated CDLs utilizing the manual *A* measurements. Ignoring all other factors that influence electrode selection, we found that the significant difference in CDL measurement techniques might lead to different clinical decisions across the range of possible choices for *thresh-A*.

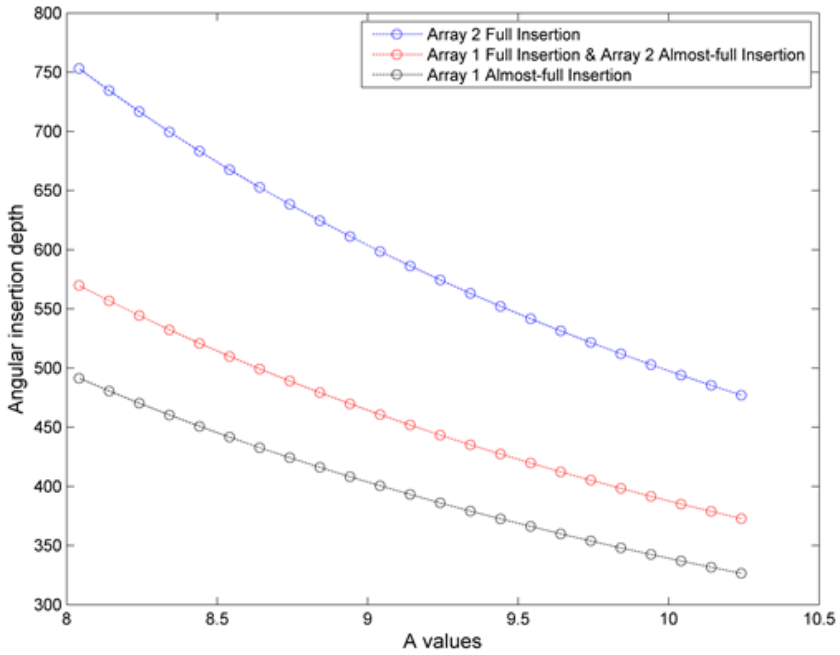

Figure 3.7. Angular insertion depths for Array 1 and Array 2 when fully and under-inserted across the range of cochlea size.

Figure 3.3 and the histograms in Figure 3.5 illustrates that the surgeons tend to underestimate the *A* value, in turn causing underestimation of CDL. Statistically significant differences between surgeons for both approaches can be explained by multiple factors. First, the

measurement requires identification of the RW, modiolus, and the opposite lateral wall of the cochlea. However, the slice containing all three anatomic landmarks is not available within normal coronal, axial or sagittal views, thus requiring specific reformatting; and difficulties in reformatting can lead to possible measurement errors. Second, once familiar with the reformatting approach, we estimate that it took approximately 90 seconds per ear to identify the appropriate angle and measure *A*. We estimate an even longer process would be necessary in clinical practice where less optimized CT analysis programs are available and familiarity with the software is rare.

Because of the large variability in the measurement of *A* value and its possible implication on the choice of the electrode clinically selected, a more consistent, less time consuming and reproducible method to determine CDL would be of high utility. The current study shows that an automatically selected *A* could achieve these desired qualities requiring ~30 seconds processing time on a standard PC. In determining CDL, there was no significant difference when using $CDL_{Direct\text{-}Auto}$ or $CDL_{A\text{-}Auto}$ calculations regarding chosen electrode type when *thresh-A* of less than 9.5 mm is used. While future studies will be required to better understand the differences between the $CDL_{A\text{-}Auto}$ and $CDL_{Direct\text{-}Auto}$ measurements, the results presented highlight the role an automated system may have in selecting electrode array types.

There were several limitations to our study. First, ideally these measurement techniques should be correlated with histopathologic and/or microCT datasets. Second, we recognize that multiple factors are considered in determining the appropriate electrode for each patient including residual hearing, etiology of hearing loss, and duration of hearing loss to name but a few. Volume and cross-sectional area of the scala tympani are other factors that might be important for electrode selection, although recent studies have not found volume to be significantly associated with scalar translocations[16]. In this study, those variables were ignored as our aim was to evaluate variability

due to choice of CDL measurement technique alone. However, it is likely that volume and cross-sectional area are correlated with CDL, and this relationship will be investigated in future work.

3.5. Conclusions

Choosing the best CI electrode array for a patient is an important task for optimizing hearing outcomes. *A*-values measured manually are user-dependent, and errors in measurement of *A* impact upon the choice of length of CI electrode array for certain patients. Measuring *A* and CDL automatically is less time consuming and generates more repeatable results. Our automatic approach could make the use of CDL for patient-customized treatment more clinically adoptable.

References

1. Hardy M. The length of the organ of Corti in man. *American Journal of Anatomy*. 1938;62(2):291-311. doi:10.1002/aja.1000620204

2. Walby AP. Scala tympani measurement. *Ann Otol Rhinol Laryngol*. 1985;94(4 Pt 1):393-397.

3. Úlehlová L, Voldřich L, Janisch R. Correlative study of sensory cell density and cochlear length in humans. *Hearing Research*. 1987;28(2):149-151. doi:10.1016/0378-5955(87)90045-1

4. Wright A, Davis A, Bredberg G, et al. Hair cell distributions in the normal human cochlea. A report of a European working group. *Acta Otolaryngol Suppl*. 1987;436:15-24.

5. Bredberg G, Teti A, Zambonin Zallone A, Lundevall E, Iurato S. Ultrastructural evaluation of the microslicing method for the study of temporal bone pathology. *Acta Otolaryngol Suppl*. 1987;436:7-14.

6. Ariyasu L, Galey FR, Hilsinger R, Byl FM. Computer-generated three-dimensional reconstruction of the cochlea. *Otolaryngol Head Neck Surg*. 1989;100(2):87-91. doi:10.1177/019459988910000201

7. Kawano A, Seldon HL, Clark GM. Computer-aided three-dimensional reconstruction in human cochlear maps: measurement of the lengths of organ of Corti, outer wall, inner wall, and Rosenthal's canal. *Ann Otol Rhinol Laryngol*. 1996;105(9):701-709. doi:10.1177/000348949610500906

8. Ketten DR, Skinner MW, Wang G, Vannier MW, Gates GA, Neely JG. In vivo measures of cochlear length and insertion depth of nucleus cochlear implant electrode arrays. *Ann Otol Rhinol Laryngol Suppl*. 1998;175:1-16.

9. Adunka O, Unkelbach MH, Mack MG, Radeloff A, Gstoettner W. Predicting Basal Cochlear Length for Electric-Acoustic Stimulation. *Arch Otolaryngol Head Neck Surg*. 2005;131(6):488-492. doi:10.1001/archotol.131.6.488

10. Miller JD. Sex differences in the length of the organ of Corti in humans. *The Journal of the Acoustical Society of America*. 2007;121(4):EL151-EL155. doi:10.1121/1.2710746

11. Erixon E, Högstorp H, Wadin K, Rask-Andersen H. Variational anatomy of the human cochlea: implications for cochlear implantation. *Otol Neurotol*. 2009;30(1):14-22. doi:10.1097/MAO.0b013e31818a08e8

12. Lee J, Nadol JB, Eddington DK. Depth of Electrode Insertion and Postoperative Performance in Humans with Cochlear Implants: A Histopathologic Study. *Audiol Neurootol*. 2010;15(5):323-331. doi:10.1159/000289571

13. Yukawa K, Cohen L, Blamey P, Pyman B, Tungvachirakul V, O'Leary S. Effects of insertion

depth of cochlear implant electrodes upon speech perception. *Audiol Neurootol*. 2004;9(3):163-172. doi:10.1159/000077267

14. Skinner MW, Ketten DR, Holden LK, et al. CT-derived estimation of cochlear morphology and electrode array position in relation to word recognition in Nucleus-22 recipients. *J Assoc Res Otolaryngol*. 2002;3(3):332-350. doi:10.1007/s101620020013

15. Hochmair I, Arnold W, Nopp P, Jolly C, Müller J, Roland P. Deep electrode insertion in cochlear implants: apical morphology, electrodes and speech perception results. *Acta Otolaryngol*. 2003;123(5):612-617.

16. O'Connell BP, Cakir A, Hunter JB, et al. Electrode Location and Angular Insertion Depth are Predictors of Audiologic Outcomes in Cochlear Implantation. *Otol Neurotol*. 2016;37(8):1016-1023. doi:10.1097/MAO.0000000000001125

17. Alexiades G, Dhanasingh A, Jolly C. Method to estimate the complete and two-turn cochlear duct length. *Otol Neurotol*. 2015;36(5):904-907. doi:10.1097/MAO.0000000000000620

18. Noble JH, Labadie RF, Majdani O, Dawant BM. Automatic segmentation of intracochlear anatomy in conventional CT. *IEEE Trans Biomed Eng*. 2011;58(9):2625-2632. doi:10.1109/TBME.2011.2160262

19. Escudé B, James C, Deguine O, Cochard N, Eter E, Fraysse B. The size of the cochlea and predictions of insertion depth angles for cochlear implant electrodes. *Audiol Neurootol*. 2006;11 Suppl 1:27-33. doi:10.1159/000095611

20. Verbist BM, Skinner MW, Cohen LT, et al. Consensus panel on a cochlear coordinate system applicable in histologic, physiologic, and radiologic studies of the human cochlea. *Otol Neurotol*. 2010;31(5):722-730. doi:10.1097/MAO.0b013e3181d279e0

21. Schuman TA, Noble JH, Wright CG, Wanna GB, Dawant B, Labadie RF. Anatomic verification of a novel method for precise intrascalar localization of cochlear implant electrodes in adult temporal bones using clinically available computed tomography. *Laryngoscope*. 2010;120(11):2277-2283. doi:10.1002/lary.21104

22. Goshtasby A. Registration of images with geometric distortions. *IEEE Transactions on Geoscience and Remote Sensing*. 1988;26(1):60-64. doi:10.1109/36.3000

Chapter IV

DEVELOPMENT AND EVALUATION OF A μCT-BASED PATIENT SPECIFIC MODEL OF THE ELECTRICALLY STIMULATED COCHLEA

Ahmet Cakir, Benoit M. Dawant, and Jack H. Noble

Department of Electrical Engineering and Computer Science, Vanderbilt University, Nashville, TN 37232

Abstract

Cochlear implants (CIs) are considered standard treatment for patients who experience sensory-based hearing loss. Although these devices have been remarkably successful at restoring hearing, it is rare to achieve natural fidelity, and many patients experience poor outcomes. Previous studies have shown that outcomes can be improved when optimizing CI processor settings using an estimation of the CI's neural activation patterns found by detecting the distance between the CI electrodes and the nerves they stimulate in pre- and post-implantation CT images. We call this method Image-Guided CI Programming (IGCIP). More comprehensive electro-anatomical models (EAMs) might better estimate neural activation patterns than using a distance-based estimate, potentially leading to selecting further optimized CI settings. Our goal in this study is to investigate whether μCT-based EAMs can accurately estimate neural stimulation patterns. We propose a method to create such customized electro-anatomical models of the electrically stimulated cochlea. We compare the accuracy of our patient- specific models to the accuracy of generic models. Our results show that the patient-specific models are on average more accurate than the generic models, which motivates the use of a patient-specific modeling approach for cochlear implant patients.

4.1 Introduction

Cochlear implants (CIs) are neural prosthetics that are used to treat sensory-based hearing loss. Over the last 20 years, they have been one of the most successful implants. CIs use an array of up to 22 electrodes to apply electrical stimulation to the inner ear to stimulate auditory nerves and permit the sensation of sound. Auditory nerve fibers in the cochlea are tonotopically mapped such that activation of nerve fibers that are deeper in the cochlea creates the sensation of lower frequency sounds. CIs are designed such that the array of electrodes is placed along the length of the cochlea, and each electrode is assumed to stimulate independent nerve populations corresponding to independent frequency channels. After a CI has been implanted, the implant processor is programmed by an audiologist. This procedure is called mapping, and each program is called a MAP. Mapping involves determining program parameters, e.g., which electrodes will be activated or deactivated, stimulation levels assigned to each active electrode, sound frequency bands assigned to each electrode, etc. The mapping process is one of the elements that has a high impact on the effectiveness of the implant. Optimal settings depend on many factors, including the location of the electrode array within the cochlea[1–3]. Since the electrode array is blindly threaded into the cochlea, with its location generally unknown, it has been impossible to determine how to optimize settings to account for variable intra-cochlear electrode position. Lacking an effective objective programming approach, audiologists make changes based entirely on patient feedback. As weeks or months of experience with given settings can be required for hearing performance to stabilize with a given set of settings, the standard clinical approach can require many programming sessions over the course of years and does not result in optimal settings for many patients.

Our group has recently developed a technique that permits detecting the intra-cochlear location of CI electrodes with a high degree of accuracy in post-op CT images[2,4–8]. Using this

approach, our group has developed the first Image-Guided Cochlear Implant Programming (IGCIP) strategy[4]. IGCIP aims to reduce channel interaction artifacts. Channel interaction occurs when an electrode stimulates the same populations of nerves that are stimulated by other electrodes. With IGCIP, electrodes that cause high levels of channel interaction are detected based on their distance to the nerves, and these electrodes are removed from the patient's map[4]. A large clinical study by our group has shown statistically significant improvement in average outcomes when implants are programmed using this approach[2].

While our studies have shown that our IGCIP approach already leads to improved outcomes, our current method for detecting channel interaction relies on an indirect estimation of each electrode's neural activation pattern based purely on the distance from the electrodes to the neural stimulation sites. This approach may be less accurate than a more comprehensive model of electrical stimulation, such as a high-resolution electro-anatomical model (EAM) of the electrically stimulated cochlea. Three-dimensional EAMs have been used by several different groups in order to investigate the voltage distribution and neural activation within the cochlea[9–12]. Even though these models have been shown to be useful, they lack the capacity to be applied in vivo, and patient-specific differences cannot be incorporated. It has been previously shown that anatomical shape variations exist[13] and likely lead to different neural activation patterns[14]. For this reason, Malherbe et al.[15] used CT images to construct patient-specific electrical models of CI users. However the model relies on manual point selection as well as approximation of fine scale intra-cochlear structures. In this study, our aim is to (1) evaluate the use of μCT-based EAMs for our application and test EAMs of various resolutions and fields-of-view to evaluate the sensitivity of the results to the choice of resolution and scope of the EAM and (2) create patient-specific high resolution EAMs using the patient CT image. As opposed to a rough approximation of the fine

scale structures as is done in[15] we leverage existing segmentation approaches that permit highly accurate localization of structures when creating the model. This is important because it has been shown in[14] that accurate localization is critical to make an accurate model and approximations done at CT resolution are inadequate. We also aim to compare accuracy of generic models, which are currently the community standard, to patient-specific ones.

4.2 Methods

4.2.1. Dataset

μCT images of 9 cadaveric cochlea specimens were acquired using a ScanCo μCT scanner that produces images with voxel size of 0.036 mm isotropic. Conventional CT images of 5 of the 9 cadaveric cochlea specimens were acquired using a Xoran XCAT scanner with voxel size of 0.3 mm isotropic. The remaining 4 specimens were used in another study which prevented acquisition of conventional images.

4.2.2. Electro-anatomical model creation

EAMs were designed based on our μCT images in a similar fashion to those designed with histological images by Whiten et al.[9]. An example μCT image is shown in Figure 4.1. The tissue was assumed to be electrically linear and the impedances of all the tissue types were assumed to be purely resistive. A uniform 3D grid of nodes was defined over the field of view of the μCT image. Nodes were assigned tissue resistivity classes, including air, bone, soft tissue, neural tissue, and electrolytic fluid. The μCT was used to determine the class of each node. Manual segmentation of the modiolus and the scala tympani and vestibuli in the μCT were used to label nodes as neural tissue and electrolytic fluid, respectively. Intensity thresholding of the μCT was used to classify

the remaining nodes into air, bone, and soft tissue classes. Electrical resistivity values for each class were selected as values found by other groups[16], with air, bone, neural tissue, soft tissue, and electrolytic fluid being assigned resistivity values of ∞, 5000, 300, 300 and 50 Ωcm, respectively.

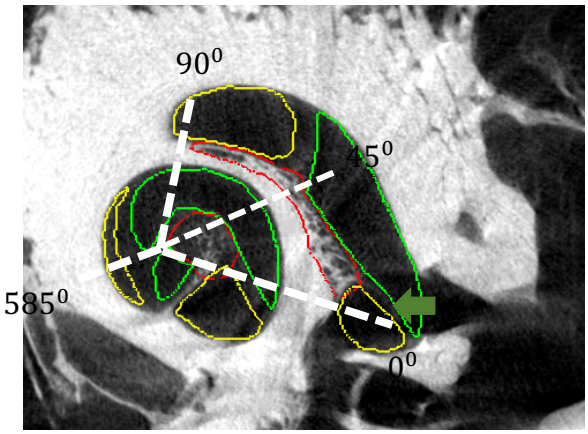

Figure 4.1. μCT image of specimen 5. Red contour represents modiolus with a resistivity of 300 Ωcm, green scala tympani, yellow scala vestibuli both with a resistivity of 150 Ωcm. Green arrow points to round window (RW) according to which angles are defined. Angles 0, 45, 90 and 225 degrees, are shown with white dashed lines.

Once the resistivity values are assigned, a system of linear equations is created by solving Poisson's Equation for electrostatistics using finite difference method:

$$\nabla \cdot J = -\sigma \nabla^2 \phi \tag{4.1}$$

where J is the current density, σ is the conductivity and ϕ is the potential. The current flows between the source (an active electrode) and the sink (a ground) which are both located within the scope of the μCT image. We adopt the Neumann boundary condition:

$$J \cdot n = 0 \tag{4.2}$$

where n is the outward normal vector at the model boundary. This condition simply states that current flow is confined to the interior of the model. The tissue in our model was assumed to be purely resistive. Thus, the amount of current that enters a node is equal to the amount of current that leaves the same node, except for the sink and source nodes. Using this notion and the

formulation of Whiten et al[9], a current conservation formula for each a node located at i,j,k can be written as:

$$I_{i,j,k}^{x^+} + I_{i,j,k}^{x^-} + I_{i,j,k}^{y^+} + I_{i,j,k}^{y^-} + I_{i,j,k}^{z^+} + I_{i,j,k}^{z^-} = \begin{cases} +1\ \mu A\ \ node_{i,j,k} = source \\ -1\ \mu A\ node_{i,j,k} = sink \\ 0\ otherwise \end{cases} \tag{4.3}$$

where $I_{i,j,k}^{x^+}$ is the current entering the node at i,j,k in the x^+ direction. The left hand variables describe the current flow between a node and one of its 6-connected neighbor nodes. Using Ohm's Law V=IR and the resistance formula, current is defined as:

$$I = \frac{\phi A \sigma}{\mathrm{L}} \tag{4.4}$$

where I is the current, ϕ is the voltage, L is the length, σ is the conductivity and A is the cross section. Given two notes located at i,j,k and $i+1,j,k$ with dimensions $\Delta x, \Delta y$, and Δz, the Equation is 4.4 can be rewritten as:

$$I^{x^+} = \left(\frac{\sigma_{i,j,k} \cdot \sigma_{i+1,j,k}}{\sigma_{i,j,k} + \sigma_{i+1,j,k}}\right)\left(\frac{\phi_{i+1,j,k} - \phi_{i,j,k}}{\Delta x}\right)\Delta y \Delta z \tag{4.5}$$

for the current in x^+ direction. A system of linear equations using the formulation $A\vec{\phi} = \vec{b}$ was created where A is a sparse matrix containing coefficients of the linear sum of currents' equations, $\vec{\phi}$ are the set of node voltages that are being determined and are concatenated into a vector, and $\vec{b}$ is a vector containing the sum of current for each node equation. In order to solve the system described above, bi-conjugate gradient method was used[17]. After solving for the voltage map $\vec{\phi}$, the current amplitude passing through each node was calculated using the Equation 4.5 in order to estimate neural activation patterns. It is believed that neural activation with cochlear implants is directly related to the current density induced by the CI in spiral ganglion cells located in Rosenthal's Canal (RC), which is located in the modiolus along the length of the cochlea[18].Thus,

we estimate neural activation patterns as the current density in RC estimated by the EAM. The position of RC was manually defined in the μCT of each specimen. Figure 4.2 shows an example result of this process.

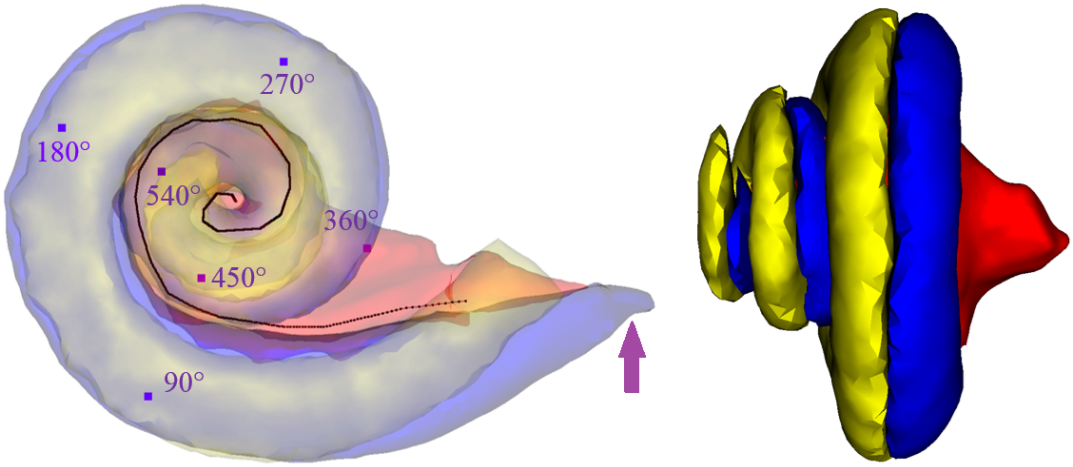

Figure 4.2. Scala tympani, scala vestibuli, and modiolus 3-D meshes are shown in blue, yellow, and red, respectively. Rosenthal's Canal (RC) is shown with a black line; stimulating electrodes at 90, 180, 270, 360, 450, and 540 degree-depths with purple squares; and Round Window with the arrow.

To simulate various electrode positions, we place a stimulating electrode at 90, 180, 270, 360, 450 and 540 degrees along the length of the scala tympani (see Figure 4.2). Angular-depth within the cochlea is defined by angle along the cochlea's spiral with 0° being defined by the location of the round window membrane of the cochlea. The cochlea has three turns, and the points corresponding to depths less than 360 degrees are located in the first turn of the cochlea. The points corresponding to depths larger than 360 degrees are located in the second turn of the cochlea. The simulated electrode locations were chosen at these angles because they are representative of the typical range of electrode locations with CIs. A node in the internal auditory canal (IAC) was defined as the ground as it is thought that nearly all current returning to the CI ground travels through the IAC[9].

4.2.3. EAM sensitivity analysis

We evaluated the importance of patient-specific design of the EAM by comparing model estimations across the EAMs built for each specimen. The sensitivity of the model to different anatomical structures is evaluated by comparing the resulting estimated current density profile (CDP) along the length of RC (see Figure 4.3) across specimens.

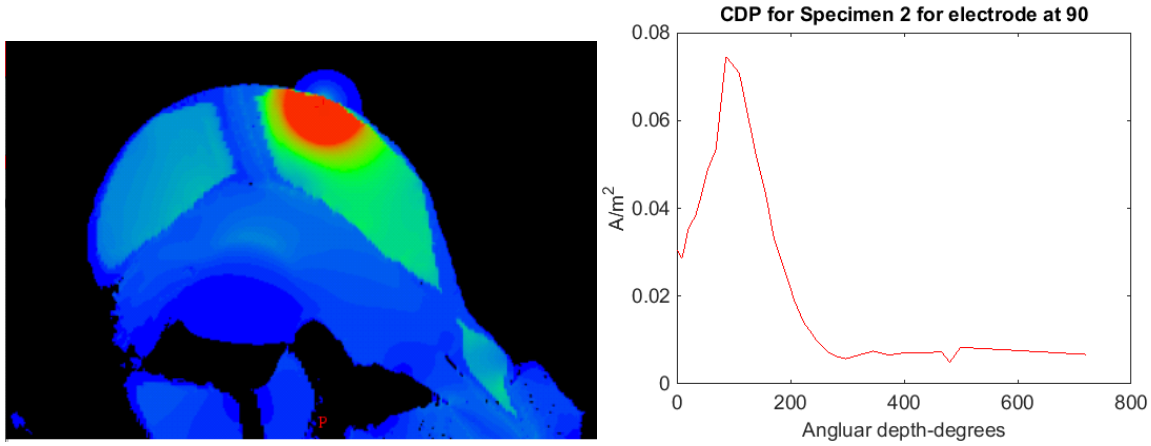

Figure 4.3. Resulting current density map (left) and current density profile (CDP—right) of the same specimen for an electrode located at 90 degree.

We also evaluated the performance of the model by testing the sensitivity of model estimations to design parameters, including field-of-view (FOV) of the mesh, resolution of the mesh, and tissue resistivity values. A more limited FOV mesh improves computational efficiency but may decrease accuracy. Similarly, coarser resolution of the mesh can improve efficiency but may decrease accuracy. Measuring the sensitivity of the model to changes in tissue resistivity will help in understanding the limits of the model's accuracy. To test sensitivity to FOV, EAMs were built with FOV at the full μCT FOV and at a limited FOV containing approximately 5 mm of space around the cochlea. To test sensitivity to resolution, EAMs were built at the full resolution of the μCT $4.6x10^{-5}mm^3$ as well as at a resolution downsampled by a factor of 2 at each step in one

direction. Further EAMs were constructed with resistivity values halved and doubled for each of the electrolytic fluid, nervous tissue, and bone resistivity values.

4.2.4. Creating anatomically customized EAMs from CT images

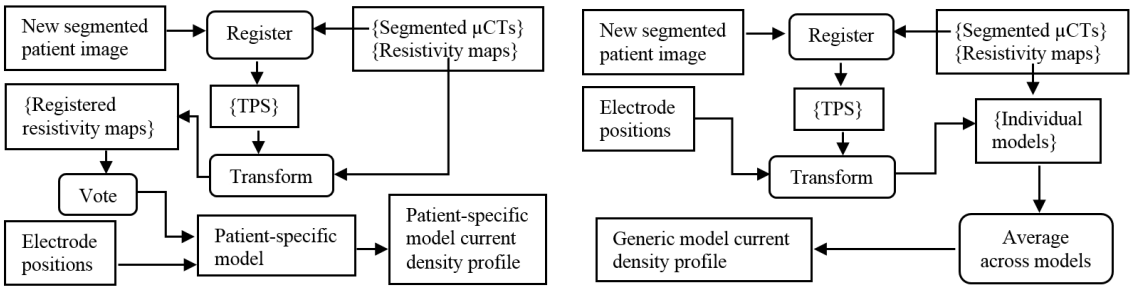

Figure 4.4. Method for creating patient-specific (a) and generic models (b).

The overview of the method proposed in this section is shown in Figure 4.4. In order to make an anatomically customized EAM with a new patient image, high resolution resistivity maps were created from μCT images of ex-vivo specimens and were projected onto the patient image through a thin-plate spline (TPS)[19] transformation that registers segmentations in the new patient image with segmentations in the μCTs. A combined resistivity map is created using a majority voting scheme between all of the 9 possible resistivity maps. Using the combined resistivity map and the patient's known electrode position, an anatomically customized EAM is created. Patient-specific neural activation is then estimated as the CDP along RC (see Figure 4.3), which is where spiral ganglion nerve cells activated by the CI are located. We also create what we refer to as a generic model to compare to our patient-specific one. A generic model is created for a new patient by mapping the patient electrode positions onto the set of high resolution resistivity maps using a TPS transformation. Each resistivity map is used to estimate a CDP. Then, the generic CDP is computed

by averaging CDPs calculated from all 9 models. We create our generic CDP by averaging the results of multiple models, as opposed to using the results from a single model, to avoid biasing the results towards the anatomy of a single individual. In this work, we implemented these proposed models and evaluated their accuracy using a leave-one-out strategy.

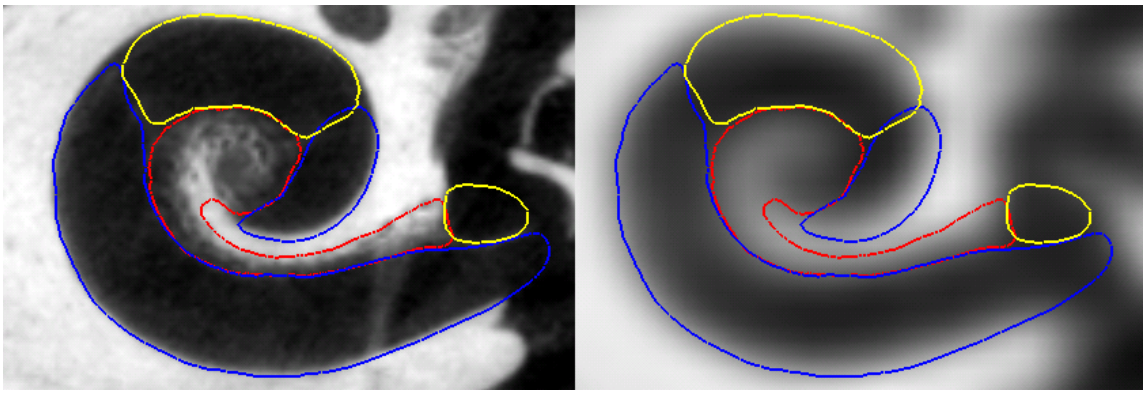

Figure 4.5. μCT (left) and CT (right) images of specimen 4, where the scala tympani, scala vestibuli, and modiolus meshes are represented with blue, yellow and red contours, respectively.

CT images were automatically segmented using previously published techniques[20] to localize the position of the electrodes and the anatomical structures that we used to create EAMs, including ST, SV, and MO. After automatic segmentation, each CT image was manually aligned with its corresponding μCT image in order for the electrodes defined in the μCT image space to correspond to the same anatomical location in the CT image space. An example of segmented and aligned μCT and CT images of a specimen is shown in Figure 4.5. Our segmentation algorithm prevents us from segmenting SM and RM. While RM is an important structure for natural hearing, its width is finer than the resolution of the μCT images so ignoring it does not affect the electrical simulations achieved by our model, and thus, segmentation of the RM was not considered critical in this study. The 3-D meshes of the anatomical structures are surfaces composed of a set of points, and they were created using an active-shape model approach.

We warped each individual μCT to match the shape of the cochlea in the CT image and combined the tissue segmentations using a voting scheme. To do this, the CT image was non-linearly registered to each of the high-resolution μCTs using TPS. The TPS formulation presented in Equation 4.6 is limited to 2-D, but extension to the 3-D formulation we used in this work is straightforward. TPS define a non-rigid transformation that minimizes the bending energy, which is given by:

$$I_f = \iint_{R^2} (f_{xx}^2 + 2f_{xy}^2 + f_{yy}^2) dxdy \tag{4.6}$$

where *f(x,y)* is the mapping function.

The surface points of the segmented ST, SV, and MO were used as landmarks in the CT image. For a one-to-one point correspondence to exist between these surfaces and the manual segmentations of the ST, SV, and MO in the μCT images, the active shape model was registered to each of the μCT images. This was done in a semi-automated fashion where first, the active shape model was fit to the image, then visible errors between the active shape model and the manual segmentations were manually corrected using software designed for this purpose, and finally the closest points on the manual segmentation surfaces were found. These points were used as the landmarks in the μCT images for the TPS transformation. The TPS registration between the low-resolution CT image and high-resolution μCTs allowed us to create a high-resolution resistivity map for each patient. The TPS mapping between two different spaces defined by two corresponding landmark point sets (x^i, y^i) and (x_i', y_i') has the form:

$$f(x,y) = a_0 + a_1 x + a_2 y + \sum_{i=1}^{n} w_i U(|(x_i', y_i') - (x,y)|) \tag{4.7}$$

where $U(r) = r^2 log r$ is the radial basis function, a_0, a_1 and a_2 are the affine coefficients, and the w_i

is the weight vector. The coefficients and the weight vector are determined such that total bending energy, e.g. total curvature, is minimized while providing an exact transformation between the two sets of landmark points.

The patient resistivity map was created in the region around the patient's cochlea and with the same resolution as the grids defined on the μCTs. The TPS registrations provided the non-linear mapping between the patient space and μCT spaces and were used to label each node in a new high-resolution patient resistivity map. For each node x in the patient resistivity map, the corresponding point y in a μCT can be found using the TPS registration. The tissue class of y was then stored as a candidate assignment for the tissue class of x. This procedure was followed for each μCT image. Using a leave-one-out strategy, 8 nonlinear mappings were created between a CT image of one specimen and the μCT images of the remaining 8 specimens. These nonlinear mappings allowed the construction of 8 different high resolution resistivity maps for each CT image. The tissue class at each pixel in the final map was chosen by majority vote:

$$L = argmax_l \sum_{i=1}^{8} (z_i = l) \tag{4.8}$$

where z_i is the stored candidate tissue class for the i^{th} resistivity map.

In addition, the nonlinear mapping was used to localize the RC (see Figure 4.2) in the newly constructed resistivity map as RC is not visible in CT images due to lack of adequate resolution. Manually segmented RCs in the remaining 8 μCT images were mapped to the CT image, resulting in 8 different RC segmentations. The final RC segmentation was generated as the average RC of all 8 segmentations. The position of the electrodes for each specimen was determined to be the same position defined in the corresponding registered μCT for that specimen.

4.2.5. Generic electro-anatomical model

Using a leave-one-out strategy, electrode locations defined in a target specimen image were nonlinearly mapped to the high resolution resistivity maps of the remaining 8 specimens through the corresponding TPS transformations. This produced 8 individual models which were executed resulting in 8 different CDPs. The final generic CDP was determined as the mean across the 8 CDPs. This method was used to create a CDP that is representative of an average cochlea.

4.2.6. Evaluation

While in-vivo CDP measurement would provide the best ground truth, such measurements are not possible. Thus, we defined the CDPs calculated from the models created using the target specimens' μCT images as the ground truth, and compared them to the CDPs calculated using patient-specific and generic models. One potential source of error in creating our models is the accuracy of the automatic anatomy segmentations in the target specimen CT image because the segmentations serve as landmarks for registration with the resistivity maps. To characterize how sensitive our results are to those errors, we also evaluated models constructed using the manual anatomy localizations that we have for the target specimen from its corresponding μCT image, which provides a baseline for how accurate our models could be given ideal landmark localization.

4.3 Results

4.3.1. Patient-specific design

We evaluated the importance of patient-specific design of the EAM by comparing model estimations across the EAMs built for each specimen. The sensitivity of the model to different anatomical structures is evaluated by comparing the resulting estimated current density profile

(CDP) along the length of RC (see Figure 4.2.) across specimens. To measure difference in model predictions across specimens, we compute the coefficient of variation (COV) in the estimated CDPs across specimens for identically located simulated electrodes. Since we are interested in using the model to estimate the relative differences in CDP between electrodes for a given cochlea, a groupwise change in scale of the CDPs among electrodes from one cochlea to another is not as important, and a direct comparison of CDP across specimens would not be appropriate. Thus, prior to comparing CDP across specimens, for each specimen, the electrode with the maximum total current density (mCD) along RC is identified, and the CDPs for all electrodes for that specimen are normalized by rescaling them by 1/mCD. mCD is chosen as the normalization factor because perception levels are thought to be related to total current density in RC. After normalization, the COV of the CDPs across specimens for each electrode can be measured to quantify inter-model differences, and these results are shown in Table 4.1.

Table 4.1. Coefficient of variation values of normalized current density profiles across all nine specimens.

	EL1	**EL2**	**EL3**	**EL4**	**EL5**	**EL6**	**Average**
Mean	0.198	0.192	0.176	0.175	0.154	0.177	0.179
Max	0.483	0.570	0.613	0.485	0.571	0.604	0.554

As seen in Table 4.1, the average mean and maximum COV values of current density, estimated at each of the densely sampled points along the length of RC are 0.179 and 0.554**.** These are relatively large values, suggesting that patient-specific anatomical difference might lead to different neural activation patterns.

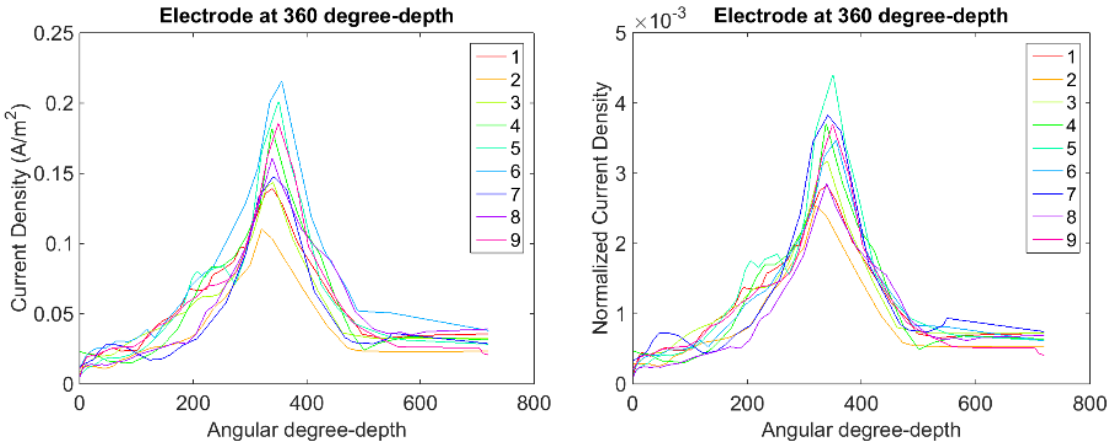

Figure 4.6. Non-normalized (left) and normalized (right) current density profiles (CDPs) of an electrode placed at 360 degree-depth across all nine models.

This indicates that using a generic model might lack the accuracy to correctly estimate CDPs, and that patient-specific models are necessary. A visual analysis also shows that the CDPs across specimens for the same electrode location differ from each other. Figure 4.6 shows the non-normalized and normalized CDPs of an electrode placed at 360 degrees across all nine models.

4.3.2. Model resolution and field of view

There are several design parameters on which our model is based. The first parameter is the FOV of the μCT images. Since we define a node for each voxel, an increase in the FOV will lead to an increase in the computational cost. On the other hand, limiting the FOV might decrease the accuracy of our model. The same principle holds true for the resolution of the μCT images. Coarser resolution will improve computational efficacy but it may decrease accuracy. In order to test the sensitivity of our model to FOV, EAMs were built with FOV at the full μCT FOV and a limited FOV that contains approximately 5 mm of space around cochlea in each direction. To test the sensitivity to resolution, the EAMs were built with full μCT resolution, 4.6×10^{-5} mm3, as well as

lower resolution levels that were achieved by downsampling the μCT images by a factor of 2 at each step.

We have calculated average percent differences in estimated CDPs between the full and the limited FOV, as well as between the full and limited resolution models. These results are shown in Table 4.2.

Table 4.2. The average percent differences in estimated current density profile along RC between full and limited FOV models, between the full and limited resolution model.

	S1	*S2*	*S3*	*S4*	*S5*	*S6*	*S7*	*S8*	*S9*	*Average*
Limited FOV	3.00	4.88	4.57	3.80	5.30	7.24	4.60	4.70	3.25	4.60
Downsampled^{2}	1.08	0.99	1.01	0.97	1.19	0.46	1.60	0.77	0.66	0.97
Downsampled^{4}	2.32	2.10	2.52	1.64	1.88	0.85	2.91	1.03	1.31	1.84
Downsampled^{8}	2.35	2.42	2.91	3.66	4.52	1.52	6.05	2.02	2.95	3.16

As can be seen in the table, limiting the FOV results in relatively small differences in estimations of current density profiles for all the specimens. In addition to accuracy, another important aspect is computational requirements and it is evident that solving a system with limited FOV is quicker, up to an order of magnitude, and requires less memory. Another parameter that effects accuracy and computational requirements is model resolution. As can be seen from Table 4.2, model resolution reduction results in small differences ~1.0%, ~1.8%, and ~3.2% when downsampled by 2, 4 and by 8, respectively. It is also evident from the table that each resolution reduction leads to a bigger mean difference, demonstrating that as resolution is increased towards the μCT resolution, the current density estimations to be converging to a specific value. This suggests that the μCT resolution is high enough and leads to accurate results. Comparisons between CDPs for full vs limited FOV, for specimens 1, 4 and 6, are shown in Figure 4.7. CDPs for specimens 1, 2 and 9, comparing different resolution levels are shown in Figure 4.8.

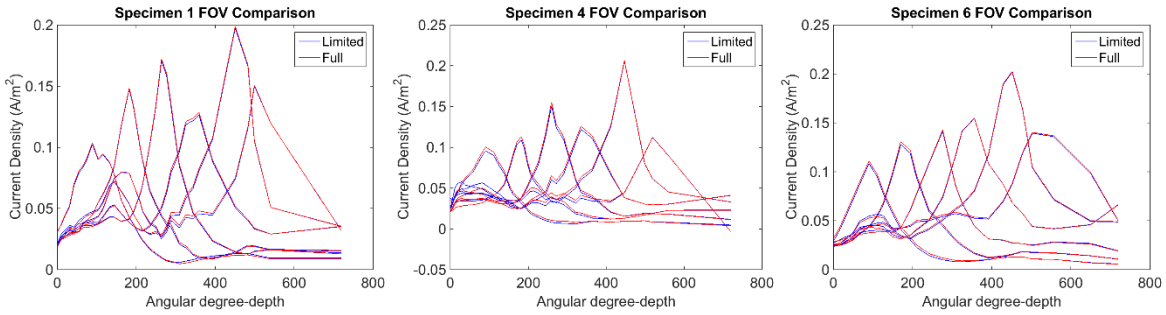

(a) (b) (c)

Figure 4.7. Current density profile comparison between full and limited FOV for three different specimens. Each peak corresponds to a different electrode location at 90, 180, 270, 360, 450 and 540 degree-depth. (a), (b), and (c) are current density profiles for specimen 1, specimen 4 and specimen 6, respectively.

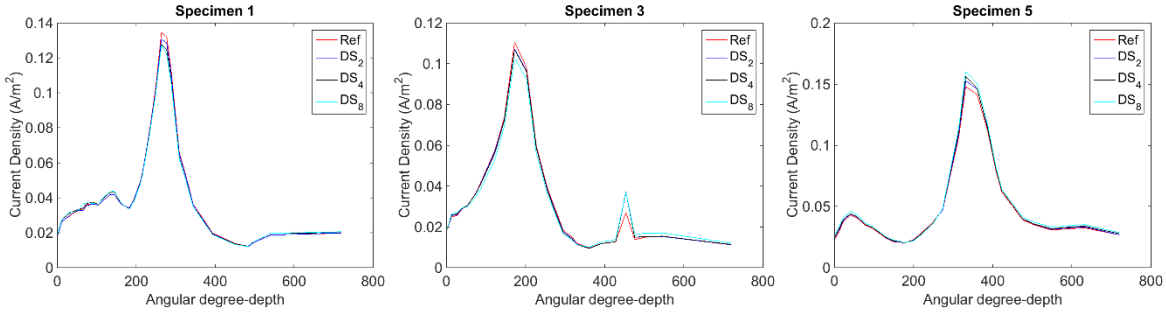

(a) (b) (c)

Figure 4.8. Comparison between different resolution levels for specimen 1, 3 and 5. Specimen 1 for an electrode located at 270 degree-depth (a), specimen 3 for an electrode located at 180 degree-depth (b), and specimen 5 for an electrode at 360 degree-depth (c).

4.3.3. Tissue resistivity analysis

Doubling bone resistivity will result in increased CDP along RC, given that the current follows a path with smaller resistivity. Increased bone resistivity means that less current will escape through bone and more current through modiolus, increasing the CDP. The same principle applies when fluid resistivity doubled and nervous tissue resistivity is halved. In order to quantify model sensitivity to different resistivity values, we first calculated the mean difference between CDPs using doubled and halved resistivity values with CDPs using default resistivity values. This is

shown in Table 4.3.

Table 4.3. The average percent differences in estimated current density profile along RC between default resistivity values and halved and doubled resistivity values. Coefficient of variation in mean difference within specimens is also included.

	Fluid halved	Fluid doubled	Nervous tissue halved	Nervous tissue doubled	Bone halved	Bone doubled
Mean difference %	-29.15	40.15	60.58	-39.59	-11.21	15.86
Coefficient of Variation	0.106	0.083	0.053	0.044	0.177	0.221

We then calculated COV values within mean difference across specimens, i.e., for doubled bone resistivity, COV is calculated using 9 different mean differences corresponding to 9 specimens as shown in Table 4.3. CDPs for specimen 4 for the different tissue resistivity conditions for an electrode located at 180 degree-depth are shown in Figure 4.9. These results show that the model is relatively insensitive to changes in the resistivity of bone but is sensitive to changes in fluid and nerve tissue resistivity.

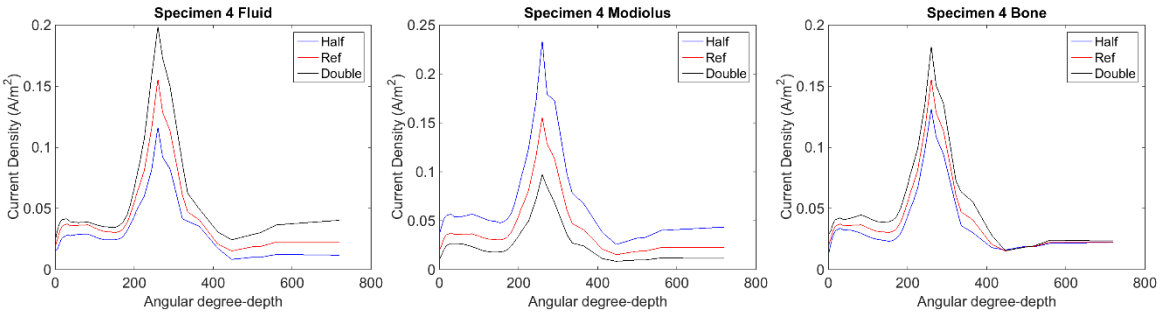

Figure 4.9. Comparison between different resistivity levels for specimen 4. Halved and doubled: Electrolytic fluid resistivity level (a), modiolus resistivity level (b), and bone resistivity level (c).

4.3.4. Evaluation of the patient-specific model

The accuracy of the patient-specific and generic models was quantified as (100% - *error*), where *error* is the absolute mean percent difference compared to the ground truth CDP. Table 4.4 shows the accuracy of the patient-specific and generic models created using manual anatomy localizations for model registration. As shown in the table, patient-specific models are relatively more accurate than generic models, demonstrated by a higher value of accuracy of 87.5% compared to 78.4%, respectively. Table 4.4 also presents the accuracy of patient-specific and generic models created using automatic landmark localization techniques. On average, patient-specific models are more accurate than generic models, 81.2% compared to 77.2%, respectively.

Table 4.4. Accuracy of the patient-specific and generic models created using manual and automatic landmarks.

		S1	*S2*	*S3*	*S4*	*S5*	*S6*	*S7*	*S8*	*S9*	*Average*
Manual landmarks	Patient-specific	87.3	87.1	91.1	88.6	83.3	87.9	92.2	85.5	84.5	87.5
	Generic	85.8	67.3	85.8	85.0	81.2	77.1	64.4	77.0	82.2	78.4
Automatic landmarks	Patient-specific	-	-	-	82.1	82.8	87.3	77.0	76.9	-	81.2
	Generic	-	-	-	83.3	81.4	77.9	66.8	76.4	-	77.2

In addition, the minimum accuracy of the patient-specific model 76.9% is relatively higher than that of the generic model, 66.8%. In general, models created using manual anatomy localizations are more accurate than those created using automatic anatomy localizations. A visual comparison between CDPs calculated from patient-specific, ground truth, and generic models for specimens 4 and 6, the cases where the patient-specific model is the least and the most accurate compared to the generic model, is shown in Figure 4.10.

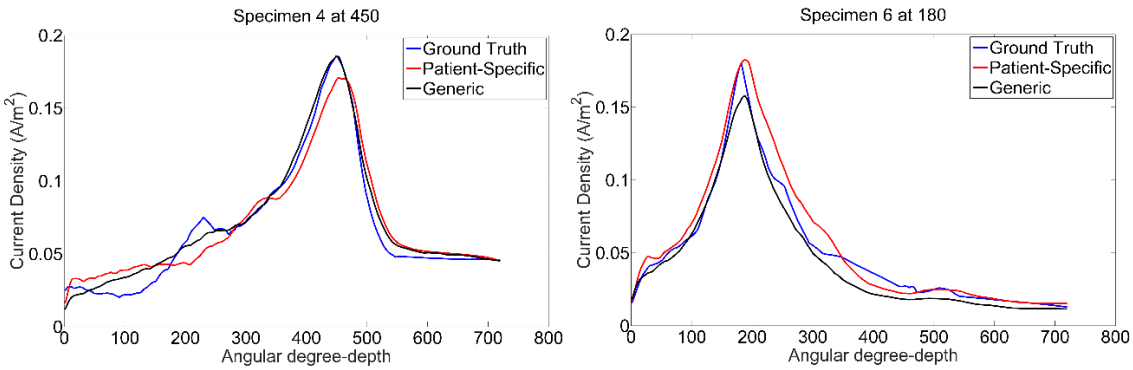

(a) (b)

Figure 4.10. A comparison of current density profiles (CDPs) between patient-specific, ground truth, and generic models. Specimen 4 (a) is stimulated with an electrode located at 450 degree-depth and, specimen 6 (b) with an electrode at 180 degree-depth.

4.4 Conclusion

To the best of our knowledge, this is the first time that a high resolution patient-specific model was created using CT images and the accuracy of such models was compared to that of generic models. Quantitative and qualitative analysis of the results indicate that improvements in landmark localization could lead to more accurate models and that patient-specific models are on average more accurate than generic models, which is currently the community standard approach. These results motivate the use of patient-specific models and represent a crucial step toward developing and validating the first in vivo patient-specific EAM, which will be used to better customize CI processor settings.

References

1. Wanna GB, Noble JH, Carlson ML, et al. Impact of electrode design and surgical approach on scalar location and cochlear implant outcomes. *Laryngoscope*. 2014;124 Suppl 6:S1-7. doi:10.1002/lary.24728

2. Noble JH, Gifford RH, Hedley-Williams AJ, Dawant BM, Labadie RF. Clinical evaluation of an image-guided cochlear implant programming strategy. *Audiol Neurootol*. 2014;19(6):400-411. doi:10.1159/000365273

3. Holden LK, Finley CC, Firszt JB, et al. Factors affecting open-set word recognition in adults with cochlear implants. *Ear Hear*. 2013;34(3):342-360. doi:10.1097/AUD.0b013e3182741aa7

4. Noble JH, Labadie RF, Gifford RH, Dawant BM. Image-guidance enables new methods for customizing cochlear implant stimulation strategies. *IEEE Trans Neural Syst Rehabil Eng*. 2013;21(5):820-829. doi:10.1109/TNSRE.2013.2253333

5. Noble JH, Hedley-Williams AJ, Sunderhaus L, et al. Initial Results With Image-guided Cochlear Implant Programming in Children. *Otol Neurotol*. 2016;37(2):e63-69. doi:10.1097/MAO.0000000000000909

6. Zhao Y, Dawant BM, Labadie RF, Noble JH. Automatic localization of cochlear implant electrodes in CT. *Med Image Comput Comput Assist Interv*. 2014;17(Pt 1):331-338.

7. Zhao Y, Dawant BM, Labadie RF, Noble JH. Automatic localization of closely spaced cochlear implant electrode arrays in clinical CTs. *Med Phys*. 2018;45(11):5030-5040. doi:10.1002/mp.13185

8. Zhao Y, Chakravorti S, Labadie RF, Dawant BM, Noble JH. Automatic graph-based method for localization of cochlear implant electrode arrays in clinical CT with sub-voxel accuracy. *Med Image Anal*. 2019;52:1-12. doi:10.1016/j.media.2018.11.005

9. Whiten DM (Darren M. Electro-anatomical models of the cochlear implant. 2007. http://dspace.mit.edu/handle/1721.1/38518. Accessed April 10, 2019.

10. Kalkman RK, Briaire JJ, Frijns JHM. Current focussing in cochlear implants: an analysis of neural recruitment in a computational model. *Hear Res*. 2015;322:89-98. doi:10.1016/j.heares.2014.12.004

11. Goldwyn JH, Bierer SM, Bierer JA. Modeling the electrode-neuron interface of cochlear implants: effects of neural survival, electrode placement, and the partial tripolar configuration. *Hear Res*. 2010;268(1-2):93-104. doi:10.1016/j.heares.2010.05.005

12. Hanekom T. Three-dimensional spiraling finite element model of the electrically stimulated cochlea. *Ear Hear*. 2001;22(4):300-315.

13. Avci E, Nauwelaers T, Lenarz T, Hamacher V, Kral A. Variations in microanatomy of the human cochlea. *J Comp Neurol*. 2014;522(14):3245-3261. doi:10.1002/cne.23594

14. Cakir A, Dawant BM, Noble JH. Evaluation of a μCT-based electro-anatomical cochlear implant model. In: Webster RJ, Yaniv ZR, eds. San Diego, California, United States; 2016:97860M. doi:10.1117/12.2217275

15. Malherbe TK, Hanekom T, Hanekom JJ. Constructing a three-dimensional electrical model of a living cochlear implant user's cochlea. *Int J Numer Method Biomed Eng*. 2016;32(7). doi:10.1002/cnm.2751

16. Geddes LA, Baker LE. The specific resistance of biological material--a compendium of data for the biomedical engineer and physiologist. *Med Biol Eng*. 1967;5(3):271-293.

17. Press WH, Teukolsky SA, Vetterling WT, Flannery BP. *Numerical Recipes 3rd Edition: The Art of Scientific Computing*. Cambridge University Press; 2007.

18. Kral A, Hartmann R, Mortazavi D, Klinke R. Spatial resolution of cochlear implants: the electrical field and excitation of auditory afferents. *Hear Res*. 1998;121(1-2):11-28.

19. Bookstein FL. Principal warps: thin-plate splines and the decomposition of deformations. *IEEE Transactions on Pattern Analysis and Machine Intelligence*. 1989;11(6):567-585. doi:10.1109/34.24792

20. Noble JH, Labadie RF, Majdani O, Dawant BM. Automatic segmentation of intracochlear anatomy in conventional CT. *IEEE Trans Biomed Eng*. 2011;58(9):2625-2632. doi:10.1109/TBME.2011.2160262

Chapter V

EVALUATION OF A HIGH-RESOLUTION PATIENT-SPECIFIC MODEL OF THE ELECTRICALLY STIMULATED COCHLEA

Ahmet Cakir[1], Robert T. Dwyer[2], Jack H. Noble[1]

[1]Department of Electrical Engineering and Computer Science, Vanderbilt University, Nashville, TN 37232

[2]Department of Hearing and Speech Sciences, Vanderbilt University Medical Center, Nashville, TN 37232

Abstract

Cochlear implants (CIs) are surgically-implanted medical devices used to treat individuals with sensorineural hearing loss who do not receive benefit from appropriately fit amplification. Although these devices have been remarkably successful at restoring audibility, many patients experience poor outcomes. Our group has developed the first image-guided CI programming (IGCIP) technique where the positions of the electrodes are found in CT images and used to estimate neural activation patterns, which is unique information that audiologists can use to define patient-specific processor settings. In our current system, neural activation is estimated using only the distance from each electrode to the neural activation sites. This approach might be less accurate than using a high-resolution electro-anatomical model (EAM) of the electrically stimulated cochlea to perform physics-based estimation of neural activation. In this work, we propose a patient-customized EAM approach where the EAM is spatially and electrically adapted to a patient-specific configuration. Spatial adaptation is done through non-rigid registration of the model with the patient CT image. Electrical adaptation is done by adjusting tissue resistivity parameters so that the intra-cochlear voltage distributions predicted by the model best match those

directly measured for the patient via their implant. We demonstrated our approach for N=7 patients. We found that our approach results in mean percent differences between direct and simulated measurements of voltage distributions of 11%. In addition, visual comparison shows the simulated and measured voltage distributions are qualitatively in good agreement. This represents a crucial step toward developing and validating the first in vivo patient-specific cochlea EAMs.

5.1 Introduction

Cochlear implants (CIs) are neural prosthetics that are used to treat sensory-based hearing loss. Each CI has an electrode array with a number of electrodes, ranging between 12 and 22, dependent upon the manufacturer. These electrodes are situated on a silicone electrode array that is surgically inserted into the cochlea. The electrodes stimulate spiral ganglion (SG) auditory nerve fibers in order to create the sensation of sound. After implantation, each CI is programmed by an audiologist to attempt to optimize CI settings that will lead to better hearing outcomes. The programming process includes determining which electrodes will be activated or deactivated, assigning stimulation levels to each electrode, assigning a sound frequency band for each electrode, and a number of other settings. Optimal settings depend on many factors, including the location of the electrodes within the cochlea[1,2]. The cochlea is composed of two principal intra-cochlear cavities called the scala tympani (ST) and scala vestibuli (SV). Inserted CI electrode arrays lie within either the ST or SV or can cross the thin membrane separating the two and lie in both cavities. The placement of the array in the scalas and the distance from each electrode to the SG nerve cells they stimulate are positional factors that affect hearing outcomes[1–3]. SG cells are located in the modiolus (MO), around which cochlea spirally wraps. 3D meshes of ST, SV, and MO are shown in Figure 5.1 in blue, yellow and red, respectively.

The intra-cochlear positioning of the electrodes is usually unknown since the electrode array is surgically inserted into the cochlea through a small opening and its intra-cochlear position cannot be seen. Lacking knowledge of the location of the electrodes, the audiologists have to entirely depend on patient feedback trying to optimize CI settings. As patients require weeks or months of experience with given settings for the hearing performance to stabilize, many programming sessions are required over the course of years and they may not result in optimal settings for many patients.

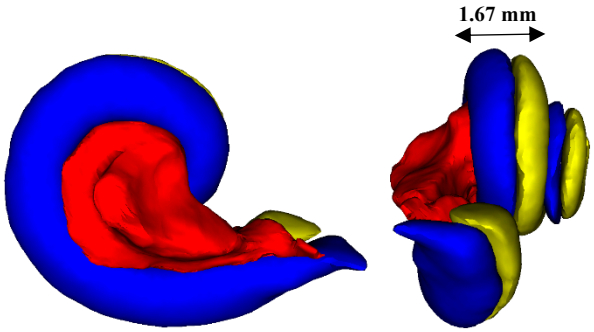

Figure 5.1. The 3D meshes of scala tympani (ST), scala vestibuli (SV) and, modiolus (MO) in blue, yellow and red, respectively. (a) is a posterior-to-anterior view. (b) is a lateral-to-medial view.

We have developed several image processing techniques that permit localization of CI electrodes in CT images with high accuracy[4–7]. Using these techniques, our group has developed the first image-guided CI programming (IGCIP) technique where electrode position is used to estimate the neural activation patterns created by the electrodes, which is unique information that audiologists can use to define patient-specific CI processor settings. It has been shown in a large clinical study that using IGCIP leads to improved average hearing outcomes[3]. Even though the clinical studies have shown that our IGCIP method leads to better hearing outcomes, it is possible that the method

could be improved with a better estimate of the electrodes' neural activation patterns. In our current system, neural activation is estimated using only the distance from each electrode to the neural activation sites. This approach might be less accurate than a high-resolution electro-anatomical model (EAM) of the electrically stimulated cochlea.

Several groups have used EAMs to study intra-cochlear voltage distribution and its effect on neural activation. Since one of the first volume conduction models created from an unrolled human cochlea using Finite Element Method[8], several methods have been adopted by different groups. Frijns et al. used a rotationally symmetric model of a guinea pig cochlea[9,10] and human cochlea[11] to solve for the voltage distribution using boundary element method (BEM). Whiten[12], and Kalkman et al.[13] created EAMs of human cochlea from histological images using Finite Difference Method and BEM, respectively. Although these models have been shown to be useful, they cannot be applied in vivo thus, patient-specific differences cannot be incorporated into these models. It has been shown that human cochleae differ not only in volume, but also in shape, number of turns, and length, etc[14,15]. Considering these anatomical differences, Malherbe et al.[16] used CT images acquired from 3 patients in order to construct three-dimensional patient-specific EAMs of CI users. However the model relies on manual point selection on the 2D CT image slices. Manually determining points using CT images alone is not only arduous, it is also difficult if not impossible to do so with fine scale intra-cochlear structures, such as the modiolar wall or the partition between the ST from the SV, because they are not directly visible due to the lack of adequate resolution of the CT. To overcome this, Malherbe et al. used a high-resolution photomicrograph of a single cochlea and rigidly registered it to the patient CT image in order to approximate the dimensions of such fine scale patient-specific structures, which we have shown to be a less accurate approach than a high-resolution non-rigid model to estimate patient-specific

anatomy[17].

In a previous study we developed a high resolution EAM created using μCT images of cochlea specimens[18]. Preliminary tests were conducted to show that the model is stable and can be made patient-specific by spatially adapting the model to patient CT data[19]. However, this model does not account for patient-specific electrical characteristics, i.e., the resistivity of different tissue types. This is important because the ultimate goal of the model is to use it to estimate neural stimulation patterns, and to do so accurately will require accurately estimating the voltage distribution in the cochlea. Thus, in this study, our goal is to develop a modeling approach that permits not only spatial adaptation but also electrical adaptation. This requires a sampling of the voltage distribution in the patient's cochlea. In the CI community, such a measurement is termed "electrical field imaging" (EFI). In this process, one electrode at a time is activated while voltage at each of the remaining electrodes in the cochlea is measured, thus sampling the intra-cochlear potentials at the sites where the electrodes sit. In this work, we propose a modeling approach that uses CT imaging to spatially adapt the model and EFI to electrically adapt the model to the patient. We demonstrate our approach for N=7 patients. Since our eventual goal is to estimate neural activation caused by the injected current, agreement between measured and simulated results in terms of voltage values at the electrodes would provide strong evidence that the estimated neural activations may be accurate.

5.2 Methods

5.2.1. Dataset

The μCT images of 9 cadaveric cochlea specimens that are used to create our model were acquired using a ScanCo scanner. These images had voxel size of approximately 0.036 mm isotropic. N =

7 patients, with 6 unilateral and 1 bilateral implants, who had undergone CI surgery were pre-operatively scanned using conventional radiological scanners with temporal bone imaging protocols and had voxel size of approximately 0.3 x 0.3 x 0.4 mm^3, and post-operatively scanned using Xoran XCAT fpVCT scanner. The voxel dimensions in these images are 0.4 mm isotropic.

In addition, EFI measurements were performed for the same patients using software provided by the CI manufacturer -- Advanced Bionics (Valencia, California USA). The EFI measurements were recorded for all of the 16 electrodes. Stimulation was performed at 32μA of current. The cochlear implant patients each had at least 6 months experience with their implants prior to the EFI measurements.

5.2.2. Patient-specific EAM

For each patient, pre- and post-implantation CT images were automatically segmented using previously published techniques[4,5] to localize the position of the electrodes and the anatomical structures that we use to create EAMs, including ST, SV, and MO. The 3D meshes of the anatomical structures are surfaces composed of a set of points, and they are created using an active-shape model approach[20]. High-resolution EAMs were created using μCT images of 9 cochlea specimens as previously described[18]. In brief, for each specimen a uniform 3D grid of nodes with spacing of 0.072 mm was defined over the field of view of the μCT image. Each node was assigned to a tissue class, including air, bone, soft tissue, neural tissue, and electrolytic fluid. Nodes that are enclosed by either ST or SV were assigned to electrolytic fluid tissue class, and nodes enclosed by MO were classified as neural tissue. For the remaining nodes, a simple thresholding of the μCT was applied in order to decide between air, bone, and soft tissue. The tissue classes correspond to different electrical resistivity values. The default values for these tissue classes are: ∞ Ωcm for air,

5000 Ωcm for bone, 300 Ωcm for soft tissue, 600 Ωcm for neural tissue, and 50 Ωcm for electrolytic fluid[20].

We warped each individual μCT to match the shape of the patient cochlea and combine the tissue segmentations using a voting scheme. To do this, the patient CT image was non-linearly registered to each of the high-resolution μCTs using thin-plate splines (TPS)[21]. The TPS formulation presented below is limited to 2D, but extension to the 3D formulation we use in this work is straightforward. TPS define a non-rigid transformation that minimizes the bending energy. The surface points of the segmented ST, SV, and MO were used as landmarks in the patient CT image. For a one-to-one point correspondence to exist between these surfaces and the manual segmentations of the ST, SV, and MO in the μCT images, the active shape model was registered to each of the μCT images. This was done in a semi-automated fashion where first, the active shape model was fit to the image, then visible errors between the active shape model and the manual segmentations were manually corrected using software designed for this purpose, and finally the closest points on the manual segmentation surfaces were found. These points were used as the landmarks in the μCT images for the TPS transformation. The TPS registration between the low-resolution patient CT image and high-resolution μCTs allows us to create a high-resolution resistivity map for each patient. The TPS mapping between two different spaces defined by two corresponding landmark point sets (x_i,y_i,z_i) and (x_i',y_i',z_i') has the form:

$$f(x,y) = a_0 + a_1 x + a_2 y + \sum_{i=1}^{n} w_i U(|(x_i', y_i') - (x,y)|) \tag{5.1}$$

where $U(r) = r^2 log r$ is the radial basis function, a_0, a_1, a_2 and a_3 are the affine coefficients, and the w_i is the weight vector. The coefficients and the weight vector are determined such that total bending energy, e.g. total curvature, is minimized while providing an exact transformation

between the two sets of landmark points.

The patient resistivity map is created in the region around the patient's cochlea and with the same resolution as the grids defined on the μCTs. The TPS registrations provide the non-linear mapping between the patient space and μCT spaces and were used to label each node in a new high-resolution patient resistivity map. For each node x in the patient resistivity map, the corresponding point y in a μCT can be found using the TPS registration. The tissue class of y is then stored as a candidate assignment for the tissue class of x. This procedure is followed for each μCT image, resulting in 9 different tissue candidates, z_i, $i = [1,2,\dots,9]$, for each node. A final resistivity map was achieved using a majority voting scheme between all of the 9 tissue candidates:

$$L = argmax_l \sum_{i=1}^{9} (z_i = l) \tag{5.2}$$

where Z is the final tissue class. Once the resistivity map is created, we use the position of the electrode array and electrodes found using post-implantation CT images to determine the location of the 16 stimulating electrodes and the silicone electrode array in the high-resolution resistivity maps. In Figure 5.2**,** the silicone electrode array, the stimulating electrodes and the MO are shown in gray, black, and red, respectively. The silicone electrode array is modeled as a perfectly resistive material. In cochlear implants, the ground electrode is located near surface of the skull adjacent to the ear to which the electrode array is implanted. Thus, the ground electrode is located relatively far from the stimulating electrodes and the SG nerve cells. Since our model only includes 5 mm of space around the cochlea, to simulate a distant ground we define the entire border of the model to be ground. Then, one of the stimulating electrodes is chosen as a current source whose current sinks to ground. We then define the system of linear equations defined by Poisson's equation for electrical current at each node:

$$\nabla \cdot J = -\sigma \nabla^2 \phi \quad (5.3)$$

where ∅ is the voltage. Solving this system of equations using the bi-conjugate gradient method[22], the final output of the model is the voltage map V, which contains the voltage at each of the nodes. This follows the approach proposed by Whiten[11].

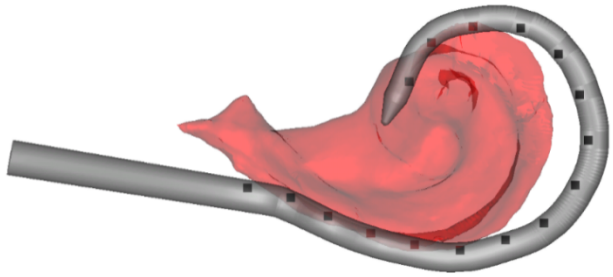

Figure 5.2. The 3D meshes of the modiolus (MO), the silicone array, and the stimulating electrodes, in red, gray, and black**.**

The second step of the approach we propose to creating patient-specific EAMs includes optimizing the resistivity values of different tissue classes to match the patient-specific values. Given that in-vivo measurements of the resistivity values of different tissue classes is not possible, a different approach was taken to try to adjust these parameters. This approach is as follows: Intra-cochlear potentials are calculated for a given patient with default tissue resistivity values for each of the 16 electrodes injecting 32 μA of current into the system. The simulated voltage distribution is then compared to the actual measured voltage distribution acquired from the patient, and new tissue resistivity values are selected to try to improve the agreement between the two. We have designed a heuristic search approach that leverages our knowledge of how changes in the resistivity values of different tissue types affect the simulated voltage distribution. We found that a change in the electrolytic fluid resistivity has negligible effects, whereas a change in the resistivity values of soft tissue and neural tissue have different effects as shown in Figure 5.3. The principal effect when

changing the soft tissue resistivity value is a change in the average value of the voltage distribution across electrodes while the shape of the voltage distribution maintains the same slope. Changing neural tissue resistivity value on the other hand sharpens or flattens the curve, i.e. a decrease in the neural tissue resistivity value will result in a flattening of the curve and vice versa.

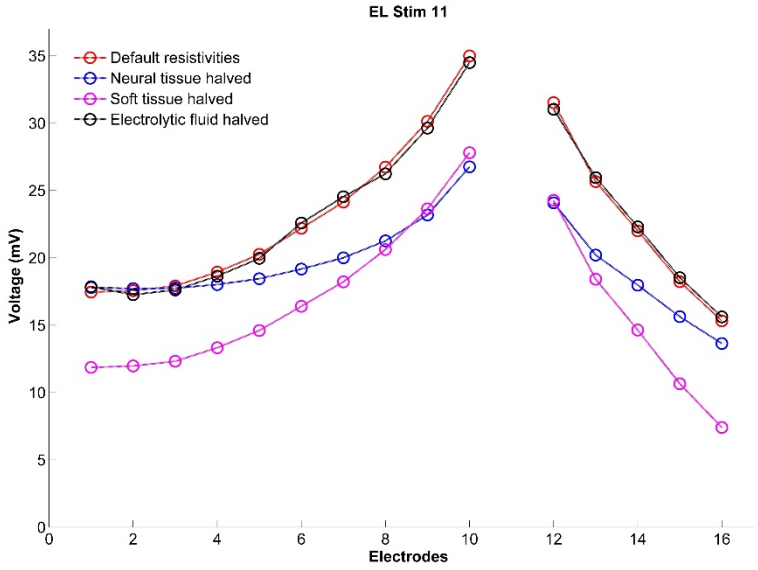

Figure 5.3. The effect of the change in the different tissue resistivity values**.**

Using this knowledge, we have developed an automatic heuristic search as shown in Algorithm 5.1. In this algorithm, the resistivity values of the soft and neural tissues are adjusted based on *average error*, which is the average normalized mean percent difference between simulation results and the acquired patient data computed as shown in the pseudocode. The algorithm first calculates the *error*, the normalized mean percent difference between simulation voltage distribution vector and the voltage distribution vector acquired from the patient for a stimulating electrode, for each of the 16 electrodes. It then checks whether those values have all the same sign, i.e. whether simulation results are either bigger or smaller than the acquired patient data for all of

the 16 active electrodes. If they all have the same sign, then it adjusts the soft tissue resistivity value multiplying it by 1 plus the *average error*. If the signs are different, then it calculates the slope of each curve and adjusts the neural tissue resistivity value by multiplying it by the ratio of the two slopes. The heuristic search runs until the change in the absolute value of the *average error* is less than a threshold value or a maximum number of iterations are completed. This heuristic search, rather than a generic search scheme, was adopted because the heuristic search uses a priori knowledge of the effect of the two parameters to converge more quickly than a generic search could, which is important due to the high computation time required for each iteration in the search.

Algorithm 5.1. Adjusting tissue resistivity values

Input: $\mathbf{V_{EFI}}$ = Patient EFI measurement, $\mathbf{V_S}$ = Simulation results, $\mathbf{R_{NT}}$ = Neural tissue resistivity, $\mathbf{R_{ST}}$ = Soft tissue resistivity,
$\mathbf{Slope_{EFI}}$ = Slope of the EFI measurement, $\mathbf{Slope_S}$ = Slope of the simulation
Initialize threshold, maxIteration, $\mathbf{R_{NT}}$, $\mathbf{R_{ST}}$ values
While Δ |*average error*| > threshold and counter < maxIteration
  Run simulation with $\mathbf{R_{NT}}$ and $\mathbf{R_{ST}}$
  For each electrode i = 1:16
    error[i] = mean(($\mathbf{V_{EFI}}$[i] - $\mathbf{V_S}$[i])/ $\mathbf{V_{EFI}}$[i])
  average error = mean(*error)*
  If *error* has the same sign for all 16 electrodes
    $\mathbf{R_{ST}}$ = $\mathbf{R_{ST}}$ * (**1** + *average error*)
  Else
    Find 6 closest (**Closest_6**) and 6 furthest (**Furthest_6**) electrode to the active electrode
    $\mathbf{Slope_{EFI}}$ = ($\mathbf{V_{EFI\_Closest\_6}}$ - $\mathbf{V_{EFI\_Furthest\_6}}$)/ $\mathbf{V_{EFI\_Closest\_6}}$
    $\mathbf{Slope_S}$ = ($\mathbf{V_{S\_Closest\_6}}$ - $\mathbf{V_{S\_Furthest\_6}}$)/ $\mathbf{V_{S\_Closest\_6}}$
    $\mathbf{R_{NT}}$ = $\mathbf{R_{NT}}$ * ($\mathbf{Slope_{EFI}}$/$\mathbf{Slope_S}$)
  counter++

5.2.3. Evaluation

A threshold value of 10^{-3} and a maximum number of iterations of 50 were used in the heuristic search. All the simulations were run on a special computer cluster, where the voltage distribution for each of the active electrodes can be calculated in parallel. We evaluated the accuracy of our EAM approach both qualitatively and quantitatively, in terms of the absolute value of the *average error*. A large difference between the initial and the final absolute value of the *average error* would

indicate that the electrical customization method provides a better fit between the simulation results and the EFI measurements.

5.3 Results

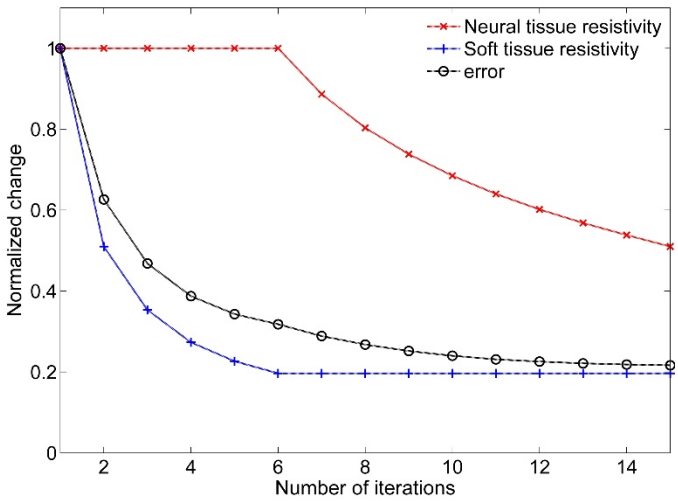

Figure 5.4. Normalized change, with respect to the default values, in soft tissue resistivity and neural tissue resistivity, and absolute value of the *average error* over number of iterations**.**

Table 5.1. Patient-specific neural and soft tissue resistivity values is shown for each ear. In addition, initial and final average error values as well as number of iterations that the heuristic search algorithm ran are shown**.**

	Average error Default tissue resistivity	*Average error Adjusted tissue resistivity*	*Number of iterations*	*Neural tissue Resistivity (Ωcm)*	*Soft tissue Resistivity (Ωcm)*
Ear 1	0.333	0.221	20	46	300
Ear 2	0.591	0.090	18	128	83
Ear 3	0.635	0.106	16	148	78
Ear 4	0.475	0.070	28	92	118
Ear 5	0.597	0.128	24	89	121
Ear 6	0.286	0.092	22	98	216
Ear 7	0.491	0.106	15	306	59
Ear 8	0.194	0.057	30	84	300
Average	0.45	0.11	22		

Each iteration takes on average an hour and a half to complete. The heuristic search algorithm was able to converge in 22 iterations on average. In Figure 5.4, the change in soft and neural tissue

resistivity values along with the absolute value of *average error* over number of iterations are shown. Final soft and neural tissue resistivity values as well as initial and final absolute value of the *average error*, and number of iterations for each ear is shown in Table 5.1. As can be seen in the table, the mean value of the *average error* when default resistivity values are used is 0.45 and it drops down to 0.11 when tissue resistivity values are customized, indicating that adjusting tissue resistivity values lead to more accurate simulation of the EFI measurements, and that our patient-specific electro-anatomical model is able to estimate patient EFI data with a high accuracy. The maximum absolute value of *average error* when tissue resistivity values are adjusted, is 0.22, as shown in the table. The algorithm was unable to find better resistivity values that will match the patient data for Ear 1 due to the noisiness of the acquired patient data (see Figure 5.5).

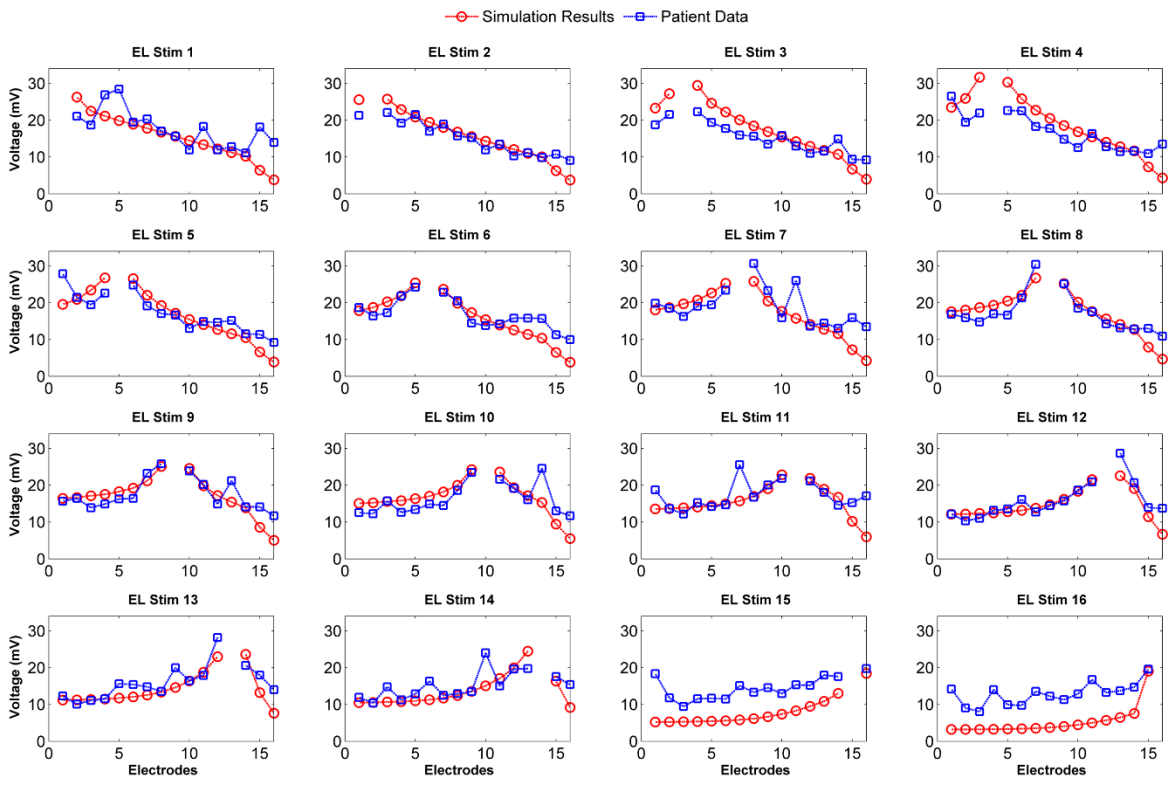

Figure 5.5. Comparison between acquired patient data and the simulation results for ear 1

In Figure 5.6, a comparison between the acquired patient data and the simulation results are shown for ear number 8. As shown in the figure, the simulated and measured results show a very similar trend, however, the model tends to overestimate the width of the region of high voltage gradient at neighboring electrodes near the stimulating electrode for certain active electrodes.

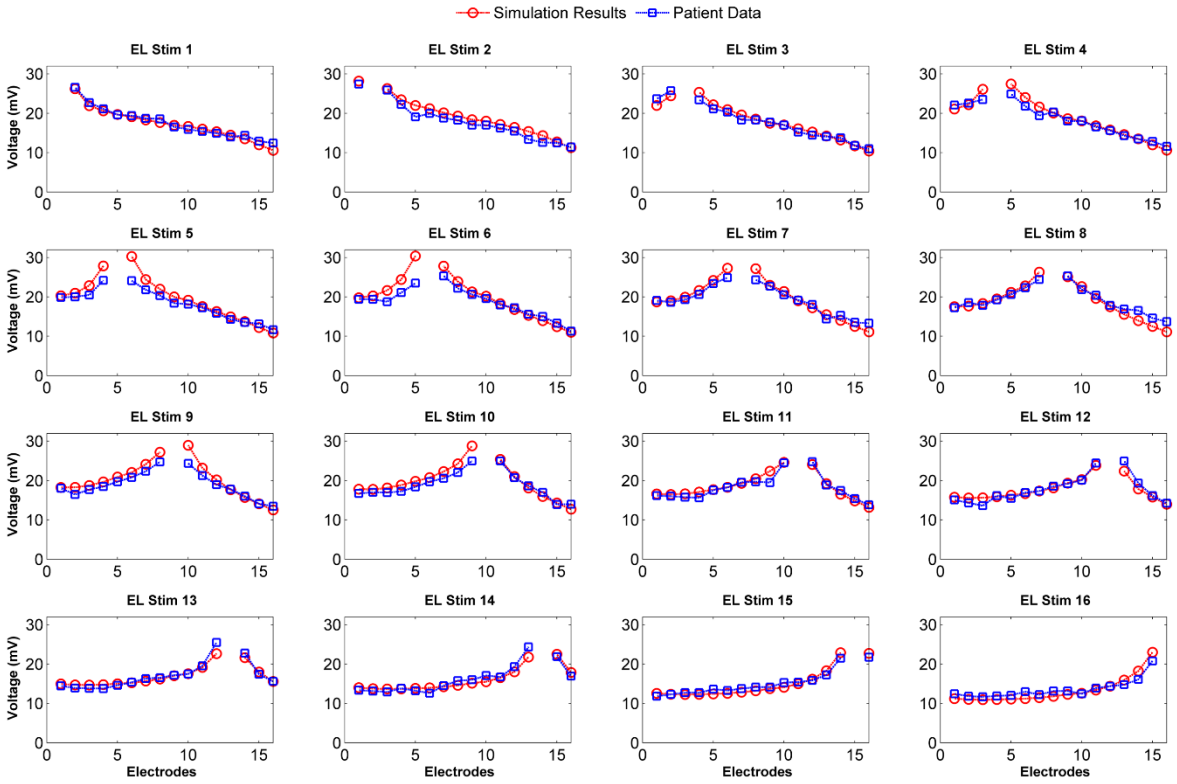

Figure 5.6. Comparison between acquired patient data and the simulation results for ear 8

5.4 Conclusion

To the best of our knowledge, this work presents the first time a high resolution patient specific model has been created for live CI recipients and compared to in vivo measurements. This represents a crucial step toward developing and validating the first in vivo patient-specific EAMs. Quantitative analysis of the results has shown that tuning resistivity values of different tissue types

for each patient increased the accuracy of our patient-specific EAMs by around 75%. However, it is important to note that currently we do not have an independent way to verify whether the simulation results are accurate or rather good fits. In the future, we plan to include a nerve model into which estimated voltage values will be input. Then, acquired electrically-evoked compound action potential measurements will be compared to the simulated action potentials in order to verify our results. Accurate in vivo patient-specific EAMs will permit more accurately estimating neural stimulation patterns and lead to selection of better CI mapping parameters, which will ultimately lead to better hearing outcomes with CIs.

References

1. Wanna GB, Noble JH, Carlson ML, et al. Impact of electrode design and surgical approach on scalar location and cochlear implant outcomes. *Laryngoscope*. 2014;124 Suppl 6:S1-7. doi:10.1002/lary.24728

2. Holden LK, Finley CC, Firszt JB, et al. Factors affecting open-set word recognition in adults with cochlear implants. *Ear Hear*. 2013;34(3):342-360. doi:10.1097/AUD.0b013e3182741aa7

3. Noble JH, Gifford RH, Hedley-Williams AJ, Dawant BM, Labadie RF. Clinical evaluation of an image-guided cochlear implant programming strategy. *Audiol Neurootol*. 2014;19(6):400-411. doi:10.1159/000365273

4. Noble JH, Labadie RF, Majdani O, Dawant BM. Automatic segmentation of intracochlear anatomy in conventional CT. *IEEE Trans Biomed Eng*. 2011;58(9):2625-2632. doi:10.1109/TBME.2011.2160262

5. Zhao Y, Dawant BM, Labadie RF, Noble JH. Automatic localization of cochlear implant electrodes in CT. *Med Image Comput Comput Assist Interv*. 2014;17(Pt 1):331-338.

6. Zhao Y, Chakravorti S, Labadie RF, Dawant BM, Noble JH. Automatic graph-based method for localization of cochlear implant electrode arrays in clinical CT with sub-voxel accuracy. *Med Image Anal*. 2019;52:1-12. doi:10.1016/j.media.2018.11.005

7. Zhao Y, Dawant BM, Labadie RF, Noble JH. Automatic localization of closely spaced cochlear implant electrode arrays in clinical CTs. *Med Phys*. 2018;45(11):5030-5040. doi:10.1002/mp.13185

8. Finley CC, Wilson BS, White MW. Models of Neural Responsiveness to Electrical Stimulation. In: Miller JM, Spelman FA, eds. *Cochlear Implants: Models of the Electrically Stimulated Ear*. New York, NY: Springer New York; 1990:55-96. doi:10.1007/978-1-4612-3256-8_5

9. Frijns JH, de Snoo SL, Schoonhoven R. Potential distributions and neural excitation patterns in a rotationally symmetric model of the electrically stimulated cochlea. *Hear Res*. 1995;87(1-2):170-186.

10. Frijns JH, de Snoo SL, ten Kate JH. Spatial selectivity in a rotationally symmetric model of the electrically stimulated cochlea. *Hear Res*. 1996;95(1-2):33-48.

11. Frijns JH, Briaire JJ, Grote JJ. The importance of human cochlear anatomy for the results of modiolus-hugging multichannel cochlear implants. *Otol Neurotol*. 2001;22(3):340-349.

12. Whiten DM (Darren M. Electro-anatomical models of the cochlear implant. 2007. http://dspace.mit.edu/handle/1721.1/38518. Accessed April 10, 2019.

13. Kalkman RK, Briaire JJ, Frijns JHM. Current focussing in cochlear implants: an analysis of neural recruitment in a computational model. *Hear Res*. 2015;322:89-98. doi:10.1016/j.heares.2014.12.004

14. Avci E, Nauwelaers T, Lenarz T, Hamacher V, Kral A. Variations in microanatomy of the human cochlea. *J Comp Neurol*. 2014;522(14):3245-3261. doi:10.1002/cne.23594

15. Erixon E, Högstorp H, Wadin K, Rask-Andersen H. Variational anatomy of the human cochlea: implications for cochlear implantation. *Otol Neurotol*. 2009;30(1):14-22. doi:10.1097/MAO.0b013e31818a08e8

16. Malherbe TK, Hanekom T, Hanekom JJ. Constructing a three-dimensional electrical model of a living cochlear implant user's cochlea. *Int J Numer Method Biomed Eng*. 2016;32(7). doi:10.1002/cnm.2751

17. Cakir A, Labadie RF, Zuniga MG, Dawant BM, Noble JH. Evaluation of Rigid Cochlear Models for Measuring Cochlear Implant Electrode Position. *Otol Neurotol*. 2016;37(10):1560-1564. doi:10.1097/MAO.0000000000001245

18. Cakir A, Dawant BM, Noble JH. Evaluation of a μCT-based electro-anatomical cochlear implant model. In: Webster RJ, Yaniv ZR, eds. San Diego, California, United States; 2016:97860M. doi:10.1117/12.2217275

19. Cakir A, Dawant BM, Noble JH. Development of a $$\upmu $$CT-based Patient-Specific Model of the Electrically Stimulated Cochlea. In: Descoteaux M, Maier-Hein L, Franz A, Jannin P, Collins DL, Duchesne S, eds. *Medical Image Computing and Computer Assisted Intervention − MICCAI 2017*. Lecture Notes in Computer Science. Springer International Publishing; 2017:773-780.

20. Cootes TF, Taylor CJ, Cooper DH, Graham J. Active Shape Models-Their Training and Application. *Computer Vision and Image Understanding*. 1995;61(1):38-59. doi:10.1006/cviu.1995.1004

21. Bookstein FL. Principal warps: thin-plate splines and the decomposition of deformations. *IEEE Transactions on Pattern Analysis and Machine Intelligence*. 1989;11(6):567-585. doi:10.1109/34.24792

22. Press WH, Teukolsky SA, Vetterling WT, Flannery BP. *Numerical Recipes 3rd Edition: The Art of Scientific Computing*. Cambridge University Press; 2007.

Chapter VI

AUDITORY NERVE FIBER SEGMENTATION METHODS FOR NEURAL ACTIVATION MODELING

Ahmet Cakir[1], Robert F. Labadie[2], Jack H. Noble[1]

[1]Department of Electrical Engineering and Computer Science, Vanderbilt University, Nashville, TN 37232

[2]Department of Otolaryngology-Head and Neck Surgery, Vanderbilt University Medical Center, Nashville, TN 37232

Abstract

Cochlear implants (CIs) are considered the standard-of-care treatment for severe-to-profound, sensorineural hearing loss. The positioning of the array within the cochlea affects which auditory nerve fibers are stimulated by which electrode and is known to affect hearing outcomes. Image-Guided CI Programming (IGCIP) techniques, where estimates of the position of the electrodes relative to the nerve fibers are provided to the programming audiologist, have been shown to lead to significantly improved hearing outcomes. With the current IGCIP approach, assumptions are made about electrical current spread to estimate which fiber groups are activated based on their distance to the electrode. To improve our estimates, we are developing an approach for creating patient-customized, high-resolution, electro-anatomical models of the electrically stimulated cochlea coupled with computational auditory nerve fiber models (ANFMs) to permit physics-based estimation of neural stimulation patterns. In this chapter, our goal is to evaluate semi- and fully-automatic techniques for segmenting auditory nerve fibers that will be used in creating ANFMs, as well as to quantify the effect of change in fiber location on the neural activation patterns. Our semi-automatic approach uses path finding algorithms to connect automatically

estimated landmarks, and our automatic approach is atlas-based. We found that repeatability in fiber localization with semi-automatic segmentation is 0.1 mm on average and results in modeled activation patterns that have 83% overlap. The difference between the semi-automatic and automatic segmentations led to higher average differences of 0.19 mm and lower activation pattern overlap of 74%.

6.1 Introduction

With over 700,000 recipients worldwide, cochlear implants (CIs) are considered the standard-of-care treatment for severe-to-profound sensoineural hearing loss[1]. Each CI has an array of 12 to 22 electrodes that is surgically inserted into the cochlea. These electrodes electrically stimulate the auditory nerve fibers to create the sensation of sound and restore the sense of hearing. After surgical insertion, each CI is programmed by an audiologist. Programming involves determining program parameters, e.g., which electrodes will be activated or deactivated, stimulation levels assigned to each active electrode, sound frequency bands assigned to each electrode, etc. The programming process is one of the elements that has a high impact on the effectiveness of the implant in accurately representing the audiological signal[2,3].

The cochlea is composed of three principal cavities called the scala tympani (ST), scala vestibuli (SV) and scala media (SM). The ST and SM are separated by the basilar membrane (BM) and the SM and SV are separated by Reissner's membrane. Anatomically, the SM is much smaller than the ST or SV, and, in practice, CI electrode arrays lie within either the ST or SV or cross the thin membranes and BM separating the two to lie partially in both cavities (e.g. one end will lie in ST and the other end will lie in ST). The placement of the array in the scalas and the distance from each electrode to the auditory nerve fibers they stimulate are positional factors that affect hearing

outcomes[2–5]. Since the electrode array is blindly threaded into the cochlea, with its location generally unknown, it has been difficult to determine how to optimize settings to account for variable intra-cochlear electrode position. Lacking an effective objective programming approach, audiologists typically make changes based entirely on subjective patient feedback. As weeks or months of experience with given settings can be required for hearing performance to stabilize with a given set of settings, the standard clinical approach can require many programming sessions over the course of years and does not result in optimal settings for many patients.

To assist audiologists in programming CIs, our group has been developing image-guided CI programming (IGCIP) techniques[3]. In IGCIP, neural stimulation patterns of the electrodes are automatically estimated based on intra-cochlear electrode position measured from CT images on which image processing has been performed to estimate the final location of the electrode array and proximity to the neurons each electrode is intended to stimluate[6]. This information is provided to the audiologist to assist with programming. We have shown in a large clinical study that using IGCIP leads to improved hearing outcomes[3]. However, in the current implementation of IGCIP, neural stimulation patterns of the electrodes are estimated in a coarse manner using only the distance from each electrode to the neural activation sites. We hypothesize that this approach might be less accurate than a physics-based model.

Several methods have been developed allowing the creation of physics-based electro-anatomical models (EAMs) of the electrically stimulated cochlea coupled with computational auditory nerve fiber models (ANFMs). EAMs allow a physics-based estimation of the voltage distribution within a given anatomical structure, and ANFMs permit estimation of neural stimulation patterns due to the electric field along the nerve fibers. We believe that such techniques may be more accurate than our current methods for estimating neural stimulation patterns as they

directly simulate current spread within the cochlea and the resulting neural activation. Several works from other groups have studied the effect of simulated intra-cochlear voltage distribution on auditory nerve fiber activation, ranging from using guinea pig cochleae[7–9] and simplified approximations of human cochleae shape[10–13]to creating models from high-resolution histological[14,15] as well as μCT images of individual human cochleae[16,17]. It has been shown by several studies that patient-specific cochlear geometry affects model predictions and thus must be addressed for the model to provide realistic results[14]. In light of such findings, several groups have studied the effects of individual morphologies on pitch placement[18] as well as estimated neural activation[19], strengthening the initial findings that computational models should incorporate the anatomical variances across individuals to offer better clinical predictions. Thus, more recent studies created EAMs using patient CT images, which enables the creation of patient-customized models[20]. In Malherbe et al.[21], the creation of the EAM model relies on manual point selection on the two-dimensional (2-D) CT image slices, which do not have the adequate resolution to accurately visualize the fine intra-cochlear structures. To overcome this, a high-resolution image of a single cochlea was rigidly registered to the patient CT image, which we have shown to be a less accurate approach than a high-resolution non-rigid model for estimating patient specific anatomy[19].

We are developing an approach for creating patient-customized, high-resolution EAMs and ANFMs, which have the potential to provide a more accurate estimation of neural stimulation patterns for CI patients than has ever before been achievable. We have reported previously on the creation of EAMs in order to calculate the electric field along the auditory nerve fibers[19,20]. In this chapter, our goal is to evaluate techniques for segmenting auditory nerve fibers to enable neural stimulation modeling and estimation of neural stimulation patterns, and to quantify the effect of

fiber segmentation accuracy on neural activation.

6.2 Methods

EAMs were created for 5 CI users using previously described techniques[19,20]. The EAMs were constructed using CT images acquired with a Xoran XCAT scanner with voxel size of 0.4 mm isotropic. In this dataset, we localized the fibers using a semi-automated technique. Since CT images do not have adequate resolution to directly visualize nerve fibers, which are approximately 2 μm in width, we must rely on a priori knowledge of the morphology of the fibers to estimate their position. We assume that (1) the unmyelinated terminal of the fiber is located where the osseous spiral lamina (OSL) meets the basilar membrane between the ST and SV, (2) the fiber proceeds through the OSL into the modiolus and then posteriorly to the nerve body (a.k.a. the soma) which is located within Rosenthal's canal (RC) adjacent to the ST within the modiolus, and (3) the fiber proceeds radially outward from the modiolus into the internal auditory canal (IAC) where the auditory nerve is formed by the collection of nerve fibers and ultimately proceeds to the auditory cortex (see Figure 6.1)[22,23].

We aim to model the section of the fibers from the unmyelinated terminal to the IAC. We treat the fiber localization problem as a path-finding problem, where the aim is to find a path connecting the terminal to the soma to the IAC endpoint and with a shape that matches the expected shape of the fiber. To do this, first, using active-shape model-based methods we have previously developed and validated, we accurately localize the ST, SV, and modiolus[24]. These structures provide excellent landmarks for the fibers because, as shown in Figure 6.1, the fibers terminate between the ST and SV, proceed around the ST into RC within the modiolus, and then proceed out of the modiolus into the IAC. Within each of 9 cochleae that were used to construct the active-

shape model, we also have defined a curve representing RC and another curve representing the location where OSL meets the BM (termed the OSL curve). We then project each reference RC curve onto the patient image through a thin-plate spline[25] (TPS) that registers the reference ST surface to the one found by the active shape model search in the patient. We define final RC curves as the average of the 9 non-rigidly registered ones. The RC curve is used to define the soma location. The OSL curve, on the other hand, is determined using the ST mesh created as a result of the active shape model search and is used to define the terminal locations. Next, to define IAC endpoints we make a copy of RC, flatten the points to a plane, and automatically translate it into the IAC using the mid-modiolar axis (see Figure 6.2).

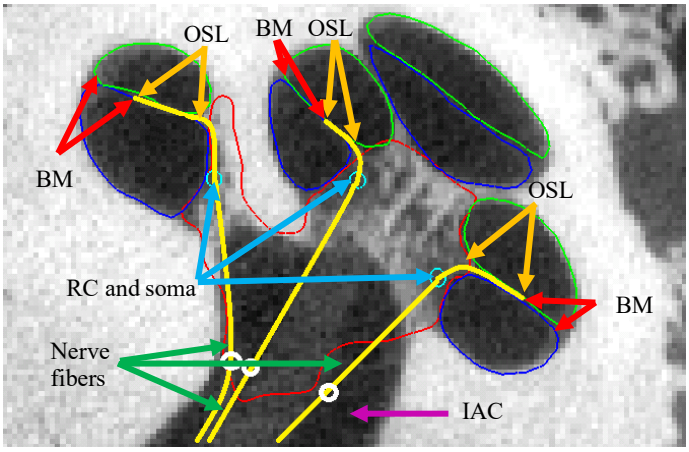

Figure 6.1. A 2D view of a µCT image where scala tympani, scala vestibuli and modiolus are shown with blue, green, and red contours; RC and IAC endpoints are shown with light blue and white circles; and nerve fibers are shown with yellow lines, respectively.

Next, we construct paths representing 75 fiber bundles that are evenly spaced along RC. For each fiber, we find the point on the OSL curve that falls in the plane normal to the RC at that fiber's RC point. We use graph search techniques to find the shortest path around the ST that connects these two points[26]. Finally, we complete the fiber by similarly using graph search

techniques to find the shortest path through the modiolus connecting the RC point and its corresponding IAC endpoint. Because the paths are computed independently and are in close proximity, sometimes they overlap or cross. As a post-processing step, we manually edit paths where this occurs to obtain a more realistic representation of the auditory nerve fibers. Each of the resulting 75 nerve fiber paths represents a bundle of roughly 400 fibers, as it is thought that normal ears have around 30,000 auditory nerve fibers.

We completed this semi-automated fiber localization process twice for each dataset in order to quantify the effect of nerve fiber angle on voltage gradient along the nerve fiber, and consequently, the effect of small differences in fiber shape on neural activation. To do this, we have moved the endpoints in IAC in a random direction that is perpendicular to the mid-modiolar axis for each patient (see Figure 6.2). The amount by which the endpoints were moved were chosen such that the endpoints were located as close as possible to the bony structure while still being located within the IAC (between 0.15 and 0.5 mm). As we do not have any a priori information on the exact location of the endpoints, this allows us to quantify the effect of choosing arbitrary endpoints on neural activation.

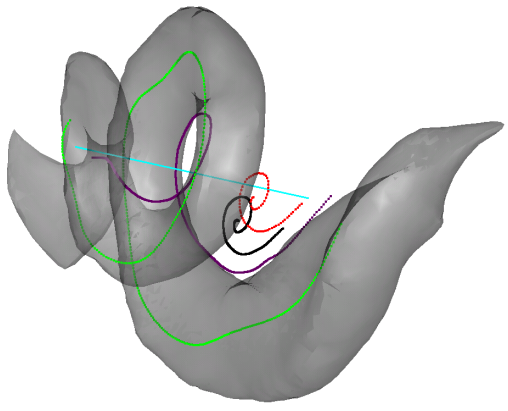

Figure 6.2. A 3D view of Scala Tympani (in grey), mid-modiolar axis (in cyan), the two different endpoints used in semi-automatic nerve fiber segmentation, shown in black and red, and the mid-point between basilar membrane and osseous spiral lamina (in green).

We also evaluated a method for fully automatic localization of the fibers by using the TPS discussed above to project fibers from a reference case onto the target cases. To evaluate our fiber localization results, we measure mean Euclidean distances between the different sets of nerve fibers, the percent difference between the gradient of the calculated voltage values measured at the active parts of the fiber, and differences in activation patterns produced when ANFM models are executed using the localized fibers. To measure activation patterns, a nerve model was created following the work done by Rattay et al.[12] using the Neuron package[27]. Briefly, a compartmental nerve model consisting of several different subunits—nodes, internodes, soma, and pre- and post-somatic regions—was created. The activation due to the voltage changes at nodes of Ranvier was modeled using the "warm" Hodgkin-Huxley (HH) model where the gating processes are accelerated compared to the original HH model. Activation patterns were determined as the *states* of nerve fibers; active or non-active. A nerve fiber is active when the changes in the voltage values along the fiber cause an action potential which is then propagated along the nerve fiber. When an action potential occurs, the potassium and sodium gates located at the nodes of Ranvier open causing changes in the inter-node voltage values.

6.3 Results

A visual comparison of localized fibers for one of the patients is shown in Figure 6.3 where only 15 out of 75 nerve fibers are shown. Each color represents a different set of auditory nerve fibers; black and red are semi-automatically segmented nerve fibers and cyan are automatically segmented nerve fibers using TPS. As shown in the figure, the differences between the different sets of nerve fibers are relatively small.

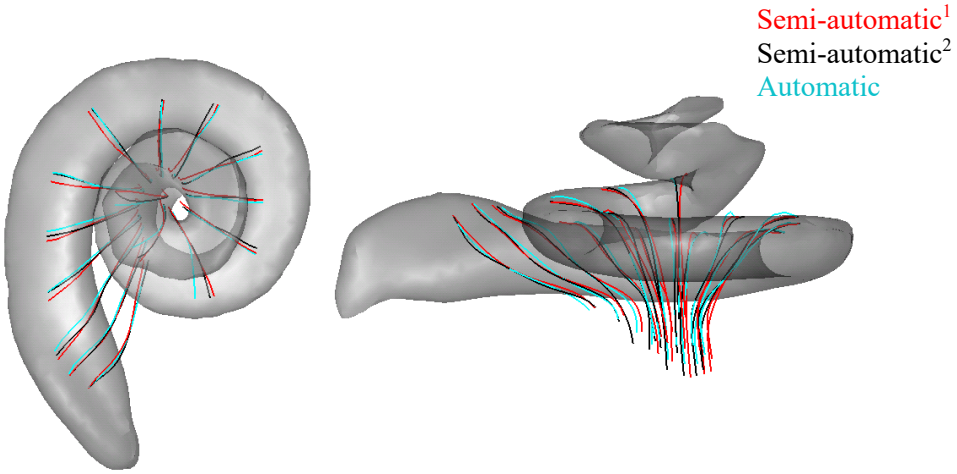

Figure 6.3. A 3D mesh of scala tympani, shown in gray, as well as different sets of auditory nerve fibers, shown in cyan, black and red.

In order to quantify the difference, we measured the Euclidian distances between each of the active compartments, namely nodes of Ranvier, and averaged them. These measurements are as follows: *semi-auto difference* is the average distance between the semi-automatically segmented nerve fibers; *auto$_1$ difference* is the distance between the automatic and one of the semi-automatic nerve fibers; and finally, *auto$_2$ difference* is the distance between the automatic and the other semi-automatic nerve fibers. The results are shown in Table 6.1. Semi-auto localization #1 in Patient 1 was used to define the reference for the automatic TPS results, and thus there is no automatic localization for this patient.

Table 6.1. The average Euclidian distance (mm) between different sets of nerve fibers**.**

Euclidian distance (mm)	Patient 1	Patient 2	Patient 3	Patient 4	Patient 5
semi-auto difference	0.08±0.06	0.10±0.08	0.09±0.05	0.06±0.04	0.15±0.11
auto$_1$ difference	N/A	0.18±0.08	0.11±0.05	0.16±0.10	0.27±0.17
auto$_2$ difference	N/A	0.20±0.11	0.13±0.07	0.18±0.11	0.29±0.21

Additionally, we have quantified the difference across voltage gradient values for each patient as percent mean differences as shown in Table 6.2. A qualitative comparison between the gradients created by electrode number 1 between the semi-automatic segmentations are shown in Figure 6.4.

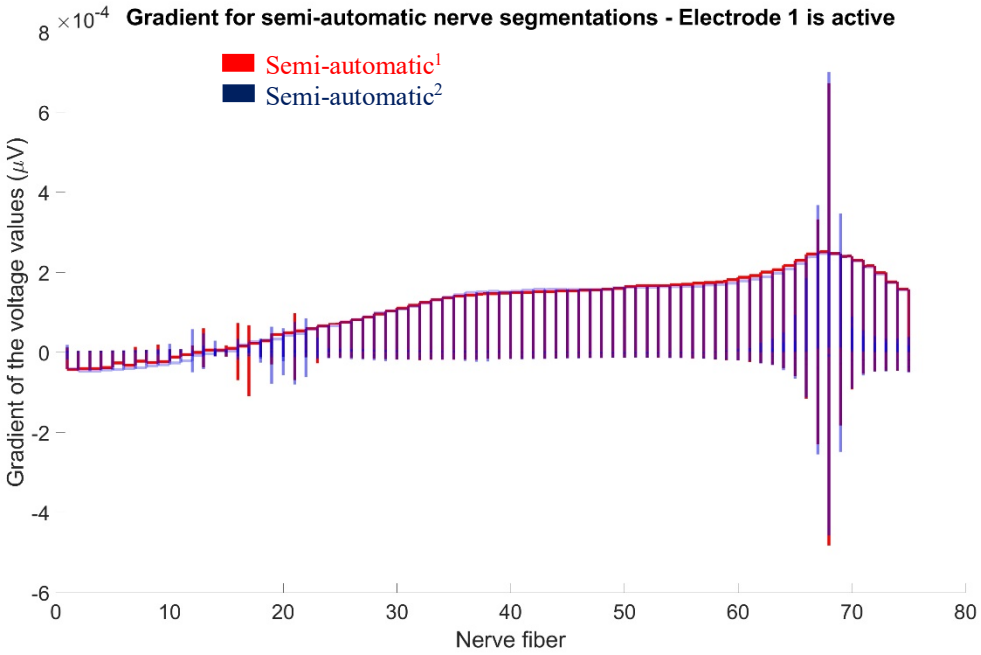

Figure 6.4. A comparison of the voltage gradient caused by electrode

Table 6.2. The average percent difference between gradient of the voltage values for different sets of fibers**.**

Gradient difference (%)	Patient 1	Patient 2	Patient 3	Patient 4	Patient 5
semi-auto difference	28.1±33.5	25.8±32.7	29.7±35.6	26.5±32.1	31.0±32.9
auto$_1$ difference	N/A	33.7±32.3	28.6±34.2	37.8±34.1	37.8±34.7
auto$_2$ difference	N/A	37.6±36.8	31.6±36.3	38.4±34.7	39.7±36.4

The similarities between neural activation patterns across different sets of segmented nerve fibers are quantified as the fraction of fibers across two sets that lead to the same states, active vs. non-active, when the ANFM is executed simulating stimulation by each of the electrodes injecting 600 μA. These results are shown in Table 6.3, and a qualitative comparison for patient 4, where electrode 3 (located at 360 degree-depth) was used as the active electrode is shown in Figure 6.5.

Table 6.3. Agreement between neural activation patterns of different sets of nerve fibers.

Similarity (%)	Patient 1	Patient 2	Patient 3	Patient 4	Patient 5
semi-auto difference	81±12	87±9	83±10	88±9	76±14
auto$_1$ difference	N/A	78±12	77±12	69±22	85±10
auto$_2$ difference	N/A	80±11	74±15	60±21	66±13

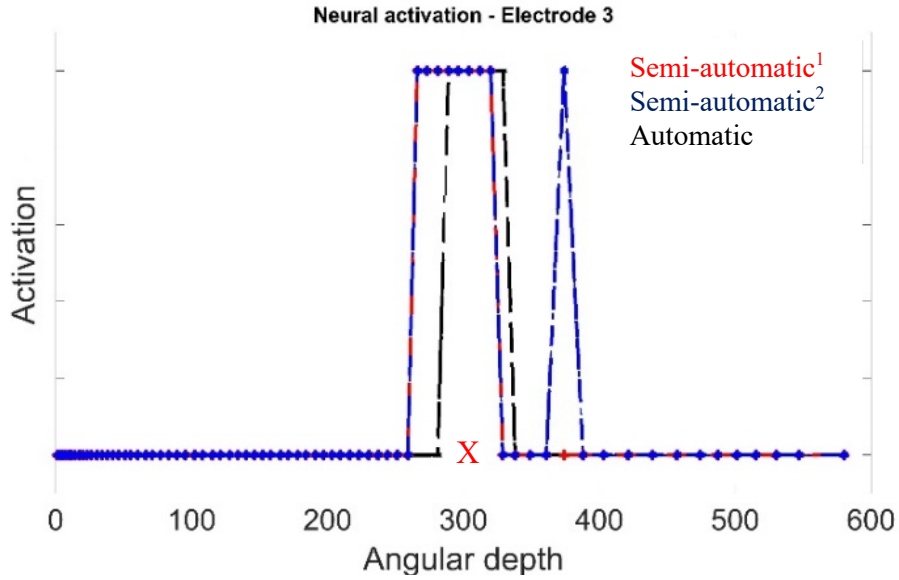

Figure 6.5. Neural activation comparison. The angular depth of the electrode is shown with X in red.

6.4 Conclusion

As shown in Table 6.3, the agreement in neural activation patterns between semi-automatically segmented nerve fibers is high, indicating that neural activation modeling estimates are not sensitive to moderate changes in fiber shape. Even in the case where the endpoints in IAC are translated by 0.5 mm, as done for patient 5, the neural activation similarity is relatively high ~76%. The similarities in neural activation patterns between the automatically and semi-automatically segmented nerve fibers were not as high. We believe that this could be due to errors in the automatic fiber localization that occur in the IAC. Since we are only using the ST to drive the TPS registration, it is effectively an extrapolating transformation far from the ST in the region of the

IAC and likely inaccurate. We are currently investigating whether the TPS accuracy can be improved in this region by designing a process to automatically segment the walls of the IAC, which are well visible in CT, and including the resulting segmentation as a landmark in the TPS transformation.

References

1. Clark G. Cochlear Implants. In: Greenberg S, Ainsworth WA, Popper AN, Fay RR, eds. *Speech Processing in the Auditory System*. Springer Handbook of Auditory Research. New York, NY: Springer New York; 2004:422-462. doi:10.1007/0-387-21575-1_8

2. Rubinstein JT. How cochlear implants encode speech: *Current Opinion in Otolaryngology & Head and Neck Surgery*. 2004;12(5):444-448. doi:10.1097/01.moo.0000134452.24819.c0

3. Noble JH, Gifford RH, Hedley-Williams AJ, Dawant BM, Labadie RF. Clinical evaluation of an image-guided cochlear implant programming strategy. *Audiol Neurootol*. 2014;19(6):400-411. doi:10.1159/000365273

4. Wanna GB, Noble JH, Carlson ML, et al. Impact of electrode design and surgical approach on scalar location and cochlear implant outcomes. *Laryngoscope*. 2014;124 Suppl 6:S1-7. doi:10.1002/lary.24728

5. Holden LK, Finley CC, Firszt JB, et al. Factors affecting open-set word recognition in adults with cochlear implants. *Ear Hear*. 2013;34(3):342-360. doi:10.1097/AUD.0b013e3182741aa7

6. Zhao Y, Dawant BM, Labadie RF, Noble JH. Automatic localization of cochlear implant electrodes in CT. *Med Image Comput Comput Assist Interv*. 2014;17(Pt 1):331-338.

7. Frijns JH, de Snoo SL, Schoonhoven R. Potential distributions and neural excitation patterns in a rotationally symmetric model of the electrically stimulated cochlea. *Hear Res*. 1995;87(1-2):170-186.

8. Malherbe TK, Hanekom T, Hanekom JJ. Can subject-specific single-fibre electrically evoked auditory brainstem response data be predicted from a model? *Med Eng Phys*. 2013;35(7):926-936. doi:10.1016/j.medengphy.2012.09.001

9. Wong P, George S, Tran P, Sue A, Carter P, Li Q. Development and Validation of a High-Fidelity Finite-Element Model of Monopolar Stimulation in the Implanted Guinea Pig Cochlea. *IEEE Trans Biomed Eng*. 2016;63(1):188-198. doi:10.1109/TBME.2015.2480601

10. Frijns JH, Briaire JJ, Grote JJ. The importance of human cochlear anatomy for the results of modiolus-hugging multichannel cochlear implants. *Otol Neurotol*. 2001;22(3):340-349.

11. Hanekom T. Three-dimensional spiraling finite element model of the electrically stimulated cochlea. *Ear Hear*. 2001;22(4):300-315.

12. Rattay F, Lutter P, Felix H. A model of the electrically excited human cochlear neuron. I. Contribution of neural substructures to the generation and propagation of spikes. *Hear Res*. 2001;153(1-2):43-63.

13. Snel-Bongers J, Briaire JJ, van der Veen EH, Kalkman RK, Frijns JHM. Threshold Levels of

Dual Electrode Stimulation in Cochlear Implants. *J Assoc Res Otolaryngol*. 2013;14(5):781-790. doi:10.1007/s10162-013-0395-y

14. Whiten DM (Darren M. Electro-anatomical models of the cochlear implant. 2007. http://dspace.mit.edu/handle/1721.1/38518. Accessed April 10, 2019.

15. Kalkman RK, Briaire JJ, Frijns JHM. Current focussing in cochlear implants: an analysis of neural recruitment in a computational model. *Hear Res*. 2015;322:89-98. doi:10.1016/j.heares.2014.12.004

16. Ceresa M, Mangado N, Andrews RJ, Gonzalez Ballester MA. Computational Models for Predicting Outcomes of Neuroprosthesis Implantation: the Case of Cochlear Implants. *Mol Neurobiol*. 2015;52(2):934-941. doi:10.1007/s12035-015-9257-4

17. Dang K, Clerc M, Vandersteen C, Guevara N, Gnansia D. In situ validation of a parametric model of electrical field distribution in an implanted cochlea. In: *2015 7th International IEEE/EMBS Conference on Neural Engineering (NER)*. ; 2015:667-670. doi:10.1109/NER.2015.7146711

18. Kalkman RK, Briaire JJ, Dekker DMT, Frijns JHM. Place pitch versus electrode location in a realistic computational model of the implanted human cochlea. *Hear Res*. 2014;315:10-24. doi:10.1016/j.heares.2014.06.003

19. Cakir A, Dawant BM, Noble JH. Development of a $$\upmu $$CT-based Patient-Specific Model of the Electrically Stimulated Cochlea. In: Descoteaux M, Maier-Hein L, Franz A, Jannin P, Collins DL, Duchesne S, eds. *Medical Image Computing and Computer Assisted Intervention − MICCAI 2017*. Lecture Notes in Computer Science. Springer International Publishing; 2017:773-780.

20. Cakir A, Dwyer RT, Noble JH. Evaluation of a high-resolution patient-specific model of the electrically stimulated cochlea. *J Med Imaging (Bellingham)*. 2017;4(2):025003. doi:10.1117/1.JMI.4.2.025003

21. Malherbe TK, Hanekom T, Hanekom JJ. Constructing a three-dimensional electrical model of a living cochlear implant user's cochlea. *Int J Numer Method Biomed Eng*. 2016;32(7). doi:10.1002/cnm.2751

22. Gray H, Carter HV. *Anatomy of the Human Body*. 20th ed. / thoroughly rev. and re-edited by Warren H. Lewis. Philadelphia: Lea & Febiger; 1918.

23. Spoendlin H, Schrott A. Analysis of the human auditory nerve. *Hear Res*. 1989;43(1):25-38.

24. Noble JH, Labadie RF, Majdani O, Dawant BM. Automatic segmentation of intracochlear anatomy in conventional CT. *IEEE Trans Biomed Eng*. 2011;58(9):2625-2632. doi:10.1109/TBME.2011.2160262

25. Bookstein FL. Principal warps: thin-plate splines and the decomposition of deformations. *IEEE Transactions on Pattern Analysis and Machine Intelligence*. 1989;11(6):567-585.

doi:10.1109/34.24792

26. Dijkstra EW. A note on two problems in connexion with graphs. *Numer Math*. 1959;1(1):269-271. doi:10.1007/BF01386390

27. Carnevale NT, Hines ML. The NEURON Book by Nicholas T. Carnevale. Cambridge Core. doi:10.1017/CBO9780511541612

Chapter VII

AUDITORY NERVE FIBER HEALTH ESTIAMTION USING PATIENT-CUSTOMIZED MODELS

Ahmet Cakir[1], Robert T. Dwyer, Katelyn Berg[2], René H. Gifford[2], Jack H. Noble[1]

[1]Department of Electrical Engineering and Computer Science, Vanderbilt University, Nashville, TN 37232

[2]Department of Hearing and Speech Sciences, Vanderbilt University Medical Center, Nashville, TN 37232

Abstract

Cochlear implants (CIs) are considered the standard-of-care treatment for severe-to-profound sensorineural hearing loss. Studies have shown that hearing outcomes with CIs are dependent on several factors, including the health of the auditory nerve fibers. We have developed a model-based approach to estimate the health of auditory nerve fibers (ANFs) by: (1) parameterizing our ANF models according to neural health; and (2) using a constrained optimization algorithm to tune the neural health of the ANFs in order to minimize the sum of squared differences between simulated and the measured physiological measurements available via patients' CIs. We refer to this process as Auditory Neural Health Imaging (ANHI). We have evaluated our ANHI approach with 5 patients. Since a comparison of monopolar and tripolar thresholds has been proposed as a surrogate for neural health, linear regression models (LRMs) were created in order to determine the correlation of clinically measured tripolar thresholds with electrode distance, monopolar thresholds, ANF model tripolar thresholds, and ANHI. LRMs revealed monopolar thresholds to be uncorrelated with tripolar thresholds. However, electrode distance, ANF model tripolar thresholds and ANHI were found to be significantly associated with tripolar thresholds with strong

LRM average correlation of R=0.81 across the 5 cases. This work represents the first clinical validation of our patient-specific EAMs. Our results demonstrate the validity of our ANHI estimates and confirm that tripolar thresholds contain neural health information. However, unlike raw tripolar threshold data, ANHI provides an estimate of which specific fiber bundles are healthy. Ultimately, we envision these models will not only permit design and implementation of novel patient-customized programming strategies, but also may provide further insight into factors that affect patient outcomes.

7.1 Introduction

Hearing is the outcome of a series of complex steps that translate sound wave signals into electrical signals. Incoming sound waves traveling through the ear canal reach the cochlea, which is the snail-shaped fluid-filled cavity. These sound waves cause a ripple effect within the cochlea which results in movement of the hair cells that correspond to the frequencies of the received sound. The hair cells are tonotopically mapped, e.g. they are fine-tuned to respond to different frequency levels. The hair cells located within the lower part of the cochlea correspond to higher frequency of sounds, and those that correspond to lower frequency sounds are located in the upper part of the cochlea. The movement of the corresponding hair cells releases chemicals into the ear inner electrically activating the spiral ganglion nerve cells. This electrical stimulation is propagated along the auditory nerve fiber traveling through the brain stem and finally reaching the auditory cortex allowing the brain to process and hear the sound.

The inner ear performs a frequency spectrum decomposition of incoming signals, and the auditory nerve fibers send this information to the brain for further processing. In patients suffering from sensorineural hearing loss caused by abnormalities in hair cells, direct electrical stimulation

of auditory nerve fibers is possible. This is done with a neural prosthesis called a cochlear implant (CI)[1]. The main components of a CI are an electrode array with up to 22 contacts that is surgically implanted into the cochlea, an externally-worn processor with microphone that picks up and decomposes the incoming signals, and a stimulator that transforms the output of the processor into biphasic electrical pulses that are sent to the appropriate contact in the electrode array.

With over 700,000 recipients worldwide and significant speech understanding benefits in the majority of those recipients, CIs are arguably the most successful neural prostheses to date. Yet, a significant number of recipients achieve poor outcomes and restoration to normal fidelity is rare even among the best performers. This is due, in part, to difficulties associated with selection of optimum stimulation parameters. Patient-specific parameter values for the processor are set by an audiologist in a series of audiological visits, resulting in a so-called MAP. Mapping involves determining program parameters, e.g., which electrodes will be activated or deactivated, stimulation levels assigned to each active electrode, sound frequency bands assigned to each electrode, etc. The mapping process is one of the elements that has a high impact on the effectiveness of the implant in accurately representing the audiological signal. However, the process has not fundamentally changed since CIs first became available and relies heavily on subjective patient feedback. Without access to objective information that can help the mapping process, audiologists go through a trial-and-error process that can take weeks or months and often leads to sub-optimal solutions.

Our group has been developing image-guided CI programming (IGCIP) techniques in order to provide objective information that can assist audiologists in mapping, which includes scalar, i.e. whether the electrode lies within the ST or SV, and angular location as well as estimated neural stimulation patterns of each electrode[2–4]. Angular location of an electrode is measured as the angle

along the spiral of the cochlea, where the round window (RW) corresponds to zero degrees (0°). Neural stimulation patterns are automatically estimated based on intra-cochlear electrode position with respect to the neurons each electrode is intended to stimulate. However, in the current implementation of IGCIP, neural stimulation patterns of the electrodes are estimated in a coarse manner using only the distance from each electrode to the neural activation sites. We hypothesize that this approach might be less accurate than a physics-based model.

Several groups have worked on predicting neural activation caused by electrical stimulation. In one of the earliest works, Rattay[5] used a current term generated from an EAM which is proportional to the second spatial derivative of the extracellular field and concluded that the activity of the axon depends on the second derivative of the extracellular medium, denoted as the "activating function". This was the method of choice in [6–8]. However, the activating function is a first approximation which assumes that the axon is infinitely long and thus, in a resting state[9] when stimulated by a constant source, which would not hold true for a finite length axon placed in a non-uniform extracellular field.

Most common models that are integrated into non-uniform electro-anatomical models (EAMs), which allow a physics-based estimation of the voltage distribution within a given anatomical structure, are physiologically-based active membrane nerve models. The potential at the active sites calculated by the EAMs are used to predict the activation of auditory nerve fibers. Such models were employed by several different groups in their studies[7,10–14]. In a 2000 study, Rattay developed a compartmental auditory nerve fiber model using a modified Hodgkin-Huxley (HH)[15] formulation and used this model to study the influence of the effect of different nerve subunits on the excitation of the nerve fibers[7]. Frijns et al. modified Schwarz-Eikhof formulation to develop so-called generalized Schwarz-Eikhof-Frijns (gSEF) model[16] and integrated into a 3-D

EAM in order to predict excitation thresholds and spatial selectivity[17], and to calculate electrically evoked compound action potentials (eCAPs)[18]. eCAPs are far-field measurements of the response of multiple auditory nerve fibers to an electrical stimulation measured via intra-cochlear electrodes. The amplitude of an eCAP is measured as the difference between the negative and positive voltage peaks that result due to the generated activation potential[19]. Malherbe et al.[20] also used the gSEF model and integrated into a patient-specific EAM constructed from clinical CT image data in order to study the difference in neural activation not only between different individuals but also right and left ear.

The methods developed in the aforementioned studies either lack the capacity to be applied in-vivo[7,10–14,16] or only confine themselves to anatomical customization[20] and do not make use of the physiological measurements that are clinically available to construct both anatomically and electrically customized models. It is possible that these models need to be fully customized in order to prove useful for clinical use. Such models might not only allow a better understanding of the patient-specific differences in CI recipients' performances, but also a prediction of certain factors such as neural survival, which is currently not possible to correctly estimate. Thus, in this work we are proposing an approach for creating patient-customized, computational auditory nerve fiber models (ANFMs) coupled with high-resolution electro-anatomical models (EAM) of the electrically stimulated cochlea. These models can be used to simulate physiological measurements available via CIs as well as to estimate the heath of auditory nerve fibers along the length of the cochlea. The methods developed to create EAMs have already been published in several conference and journal articles[21,22]. In this study, our goal is to develop methods that enable customization of ANFMs and clinically verify model findings.

7.2 Methods

7.2.1. Overview

An overview of the method presented in this chapter is shown in Figure 7.1. We have developed a model-based approach for estimating the health of auditory nerve fibers as it varies along the length of the cochlea. Our models include a physics-based patient-specific EAM of current spread induced by the electrodes coupled with ANFMs. Our EAMs were geometrically customized using patient CT images, and the electrical properties were customized using EFI measurements (see Figure 7.1). Patient-specific ANFMs were created by segmenting the auditory nerve fibers within the EAM space and modeling auditory fiber activation using active membrane models similarly to Rattay et al. 2001[7]. In this work, we represent 30,000 auditory nerve fibers that exist in a healthy human cochlea[23] by 75 distinct auditory nerve bundles that are segmented along the length of the cochlea, each of which roughly represents 400 fibers. Due to this simplification, our ANFMs can only determine whether a nerve bundle is activated or not but not how many nerve fibers are activated. Thus, we make the assumption that the model threshold level at which a nerve bundle is activated is the 50% activation level, e.g. 50% of the fibers in the said bundle is activated. Even though, this approach significantly reduces the computational cost of our approach, it also renders it impossible to determine clinical thresholds and requires us to rely on clinically measured monopolar thresholds, which are used as the model monopolar thresholds.

We estimate the ANHI by: (1) parameterizing our ANFMs according to neural health; and (2) using a constrained optimization algorithm to tune the neural health of the ANFMs in order to minimize the sum of squared differences between simulated and the measured physiological measurements available via patients' CIs. We refer to this process of estimating neural health for

fibers along the length of the cochlea as Auditory Neural Health Imaging (ANHI), an example result of which is shown in Figure 7.1.

7.2.2. Dataset

N = 7 patients with unilateral implants, who had undergone CI surgery, were preoperatively scanned using conventional radiological scanners with temporal bone imaging protocols with a voxel size of ~0.3x0.3x0.4 mm^3 and postoperatively scanned using a Xoran XCAT fpVCT scanner. The voxel dimensions in these images were 0.4 mm isotropic.

Electric field imaging (EFI)[23] measurements were performed for the same patients using software provided by the CI manufacturer— Advanced Bionics (Valencia, California). EFI is the simultaneous measurement of voltage values at every other electrode relative to a far field ground when one electrode at a time is activated to inject 32 μA of current into the cochlea. The EFI measurements were recorded for all of the 16 electrodes.

The amplitude of an eCAP is expected to increase with increased amounts of current[19,24–26]. The amplitude of an eCAP can be plotted with respect to the amount of current injected into the cochlea resulting in an amplitude growth function (AGF). The amount of the injected current is increased at each step and the time intervals are chosen such that the activated auditory nerve fibers can return to their resting state between measurements. eCAPs can also be used to measure spread of excitation (SOE) which allows the study of the overlapping excitation fields between different electrodes. The SOE measurements represent the relative amount of overlapping auditory nerve fibers that are activated by two electrodes, denoted as the masker and the probe. SOE is expected to be the maximum when the masker and the probe electrodes are the same and to be the minimum when two different electrodes with the highest spatial distance are used. AGF and SOE

measurements were collected for the same 7 patients, and an example of these measurements for representative electrodes is shown in Figure 7.1.

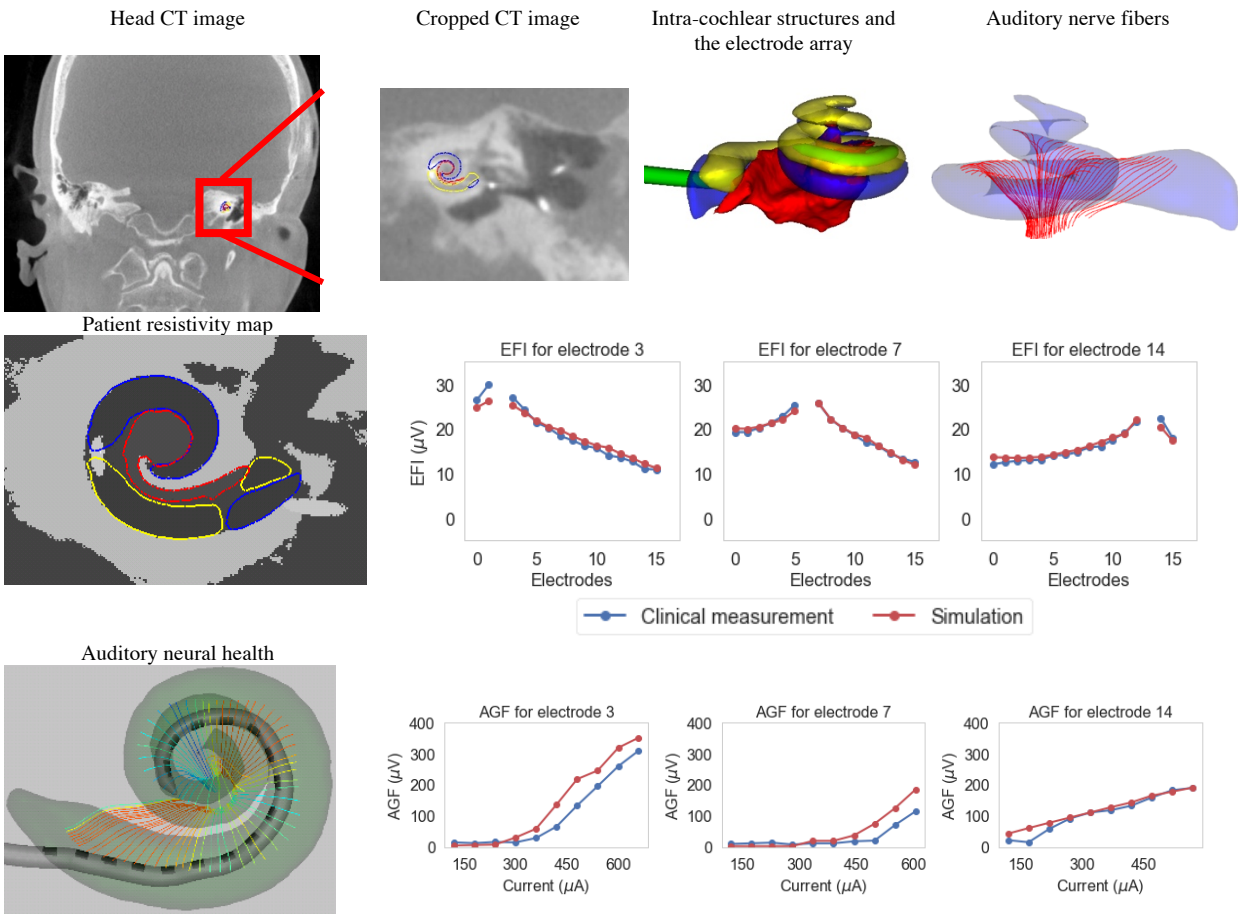

Figure 7.1. An overview of the construction of patient-specific electro-anatomical and auditory nerve fiber models. The first row demonstrates the segmentation of intra-cochlear structures as well as auditory nerve fibers. The second and third rows are example results after customizing the electro-anatomical and auditory nerve fiber models, respectively.

7.2.3. Electro-anatomical model customization

We created physics-based EAMs to determine the patient-specific voltage profiles caused by the current injected via intra-cochlear electrodes. This was achieved by first constructing an active shape model (ASM) using the structures, i.e. scala tympani (ST), scala vestibuli (SV), and modiolus (MO), that were manually segmented in high-resolution μCT images[27]. ST and SV are

fluid-filled cavities and together form the cochlea. MO, on the other hand, is the bony region that encases the spiral ganglion nerve cells. The ASM is automatically fitted to the external boundary of the cochlea that is visible in conventional CT images. This procedure is used to segment the intra-cochlear structures in a new patient image[27] with a Dice similarity score of 0.8. We have shown in Chapter 4 that that improvements in intra-cochlear structure segmentation can lead to more accurate models. Patient-specific models created from manually segmented cochleae in high-resolution images had a higher accuracy of 87.5% compared to an accuracy of 81.2% when the same models were created from automatically segmented intra-cochlear structures using the aforementioned methods.

High-resolution EAMs were created using patient CT images as previously published[21,22]. Briefly, high resolution resistivity maps, which are tissue class label maps used to define the electrical resistivity of the tissue in the image, were created from μCT images of ex-vivo specimens and were projected onto the patient CT image through a thin-plate spline (TPS)[28] transformation that registers segmentations in the new patient image with segmentations in the μCTs. A combined resistivity map is created using a majority voting scheme between all of the 9 possible resistivity maps. A node was defined at the center of each voxel representing the tissue type to which the voxel belongs. These tissue types are electrolytic fluid, neural tissue, soft tissue, bone, and air. The voxels enclosed within ST and SV were assigned to electrolytic fluid class, and those within MO were assigned to neural tissue class. A decision between soft tissue, bone and air was performed following a thresholding procedure. Voxels with a Hounsfield unit of over 1200 and less than -800 were assigned to bone and air classes, respectively. The remaining voxels were assigned to soft tissue class. Finally, spatially customized EAMs were used to solve the Poisson's equation for electrostatics, which is given by:

$$\nabla \cdot J = -\sigma \nabla^2 \Phi \tag{7.1}$$

Where Φ is the potential, J is the current density and σ is the conductivity. This system of equations was solved using the bi-conjugate gradient method[29]. The final output of the model is the voltage map Φ, which contains the voltage at each of the nodes. This follows the approach proposed by Whiten[24].

Electrical customization is achieved by optimizing the resistivity values used in creating the EAMs so that the difference between the measured EFI and the simulated EFI values is minimized. We have extended the previously published method[22] by including the bone and electrolytic fluid tissue classes into the customization process. A grid search algorithm was used in order to find the resistivity values that minimize the difference between the measured and simulated EFI, denoted as *average error,* which is defined as:

$$average\ error = \frac{\sum_{i=1}^{M} \sum_{j=1, j \neq i}^{M} \left| 1 - \frac{EFI_{S_{i,j}} / \sum EFI_S}{EFI_{C_{i,j}} / \sum EFI_c} \right|}{M * (M-1)} \tag{7.2}$$

where EFI_C is the clinically measured EFI, EFI_S is the simulated EFI, and M is the number of electrodes. The *average error* value was calculated after normalizing the EFI values, which allows us to determine the scaling factor of the resistivity values after the optimization step reducing the number of search parameters by 1. 4D grid consisting of the resistivity values for soft, neural, bone and electrolytic fluid was created. For each tissue class, values ranging from 50 to 150% of the default resistivity value with a uniform step of 25% were chosen. Default resistivity values for soft, electrolytic fluid, neural tissue, and bone are 300, 50, 600, and 5000 Ωcm, respectively. The air on the other hand was modeled as perfectly resistive rather than with a high resistivity value in order to eliminate the rounding off errors that occur due to high order difference between the

resistivity values of air and other tissue types. After the grid search is completed, the final resistivity set with the lowest *average error* was scaled by $\sum EFI_C / \sum EFI_S$.

Additionally, we compute the difference between the measured and the simulated EFI values for each electrode in order to determine the electrodes around which fibrous tissue might have grown by assuming that the higher differences seen between the measured and the simulated EFI values are only due to tissue growth phenomenon. This is a phenomenon seen with CI users, where after the insertion the body treats the electrode array as a foreign object and starts forming scar/fibrous tissue around it[30–33]. It has also been shown that the efficiency of CIs is affected by such tissue growths consisting of inflammation or fibrosis[34]. In order to capture the changes in electrical impedances caused by tissue growth, we first optimize the set of resistivity values that minimize the *average error* aforementioned above. We then determine the electrodes for which the difference between the simulated and measured EFI values are more than thrice the *average error* calculated using the optimized resistivity values. We chose this value because the optimized soft tissue resistivity values were at least three-folds the optimized electrolytic fluid resistivity value. We then automatically create a 'tissue growth region' by dilating the electrode array. It is important to note here that it is not possible to determine the thickness of the tissue growth region from patient CT images because the metallic electrodes distort the intensity around the electrode array due to the beam hardening artifacts. Thus, we assume a uniform tissue growth region thickness across patients and dilate the electrode array by 2 voxels in each direction. The scar tissue region was assumed to span the halfway points between the electrode itself and the neighboring electrodes, i.e., the scar tissue growth for electrode x is assumed to be between $\frac{\varphi_x + \varphi_{x+1}}{2}$ and $\frac{\varphi_x + \varphi_{x-1}}{2}$ where φ is the angular depth of electrodes. Angular depth of an electrode is measured as the angle along the spiral of the cochlea, where the round window (the entrance of the cochlea)

corresponds to zero degrees (0°). For the most basal electrode, the scar tissue growth region is assumed to be between the electrode and the round window. Finally, the grid-search optimization algorithm is then rerun including the tissue growth region which is parameterized as soft tissue. Another approach would be to leave the soft tissue parameter fixed and change the scar tissue thickness to optimize the EFI fit, which will be evaluated in future work.

7.2.4. Nerve Model

We followed the work done by Rattay et al.[7] to compute patient-specific neural response from 75 auditory nerve bundles to the current injected by the CI contacts. For each fiber bundle, we follow the approach of Rattay et al., where the 'warmed' HH (wHH) model was used. With wHH, the gating processes are accelerated compared to the original HH model. wHH includes sodium, potassium and leakage currents and has the following form[15]:

$$\frac{dV}{dt} = [-g_{Na}m^3h(V - V_{Na}) - g_K n^4(V - V_K) - g_L(V - V_L) + i_{stimulus}]/c \tag{7.3}$$

$$\frac{dm}{dt} = [-(\alpha_m + \beta_m)m + \alpha_m]k \tag{7.4}$$

$$\frac{dh}{dt} = [-(\alpha_h + \beta_h)h + \alpha_h]k \tag{7.5}$$

$$\frac{dn}{dt} = [-(\alpha_n + \beta_n)n + \alpha_n]k \tag{7.6}$$

$$k = 3^{T-6.3} \tag{7.7}$$

$$V = V_i - V_e - V_{rest} \tag{7.8}$$

where V, V_i, V_e and V_{rest} are the membrane, internal, external and resting voltages, and V_{Na}, V_K and V_L are the sodium, potassium and leakage battery voltages, respectively. g_{Na}, g_K, g_L are the maximum conductance and m, h, n are probabilities with which the maximum conductance is

reduced with respect to measured gating data, for sodium, potassium and leakage, respectively. Finally, α and β are voltage dependent variable that were fitted from measured data and k is the temperature coefficient, which is required in the original HH model. The original experiment temperature was 6.3 °C, which is modified to 29.0 °C as done in Rattay[7].

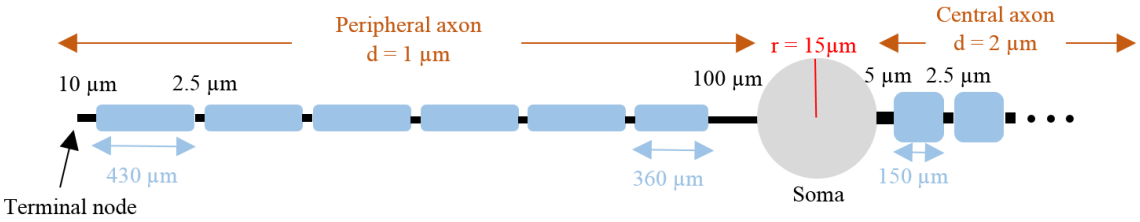

Figure 7.2. The geometrical properties of the auditory nerve fiber.

The geometry of the auditory nerve fiber used in this study is shown in Figure 7.2. As shown in the figure, a nerve fiber consists of several different subunits which are peripheral nodes and internodes, somatic, pre- and post-somatic regions, and central nodes and internodes. Each of these subunits can be thought as a compartment that is modeled by an electrical circuit with distinctive electrical properties. In our study, we have used the same electrical and geometrical properties as Rattay did in his work[7]. Briefly, the peripheral part of the axon contains an unmyelinated terminal, 5 nodes of Ranvier, 6 internodes and a presomatic region and has a diameter of 1 µm. The central part of the axon contains the postsomatic region, 16 internodes and 15 nodes of Ranvier and has a diameter of 2 µm. The peripheral internodes have a length of 430 µm, with the exception of the last internode, whereas the central internodes have a length of 150 µm. The terminal, presomatic and postsomatic regions are 100, 10 and 5 µm long, respectively. Both peripheral and central nodes of Ranvier are 2.5 µm long. The peripheral internodes are covered with 40 shielding layers, whereas the central ones are covered with 80 layers. Finally,

soma is modeled as a perfect circle with a diameter of 30 μm and is covered with 3 shielding layers.

The original electrical properties of the HH model were modified in order to compensate for the lower temperature, which was assumed to be 6.3 °C at the original HH model, and to reach 10-fold channel density. Thus, the gating variables associated with sodium channel activation/inactivation and potassium channel activation, m, h, and n respectively, were multiplied by a factor of k as defined in Equation 7.7 where T is temperature in Celsius. Additionally, g_{Na}, g_K, g_L which are the maximum conductances for sodium, potassium and leakage, respectively, were multiplied by a factor of 10.

7.2.5. Nerve segmentation

Auditory nerve fibers along the cochlea are segment using the method explained in Chapter 6. The segmentation of the section of the fibers from the unmyelinated terminal to the internal auditory canal (IAC) were carried out relying on the *a priori* knowledge of the morphology of the fibers as well as the accurate localization of the landmarks that provide useful information with respect to the location of the nerve fibers. The unmyelinated terminals are located between the basilar membrane and the osseous spiral lamina (OSL), which will be referred to as the OSL curve. The fiber then proceeds into the MO where the nerve body cells, namely soma, are located within Rosenthal's Canal (RC). It then radially proceeds outwards into the internal auditory canal (IAC) passing through what we refer to as IAC end points[35,36]. The location of the OSL curve as well as RC can be accurately localized using the methods that we have previously developed[21]. The location of the IAC endpoints on the other hand were estimated by flattening the points that make up the RC curve onto a plane located along the mid-modiolar axis around which the cochlea spirals.

We have shown in our previous studies that the model output is insensitive to moderate changes in the location of the IAC endpoints[37]. The fiber segmentation is treated as a path-finding problem, where the aim is to find a path connecting the unmyelinated terminal to the soma to the IAC endpoint with a shape that matches the expected shape of the fiber. Using Dijkstra's algorithm[37], the paths connecting the corresponding points on the OSL, RC and IAC endpoint curves were found. Finally, a spline was fit to the path in order to create a shape that matches the anatomically expected shape of the nerve fibers. Segmented nerve bundles are shown in red in Figure 7.3.

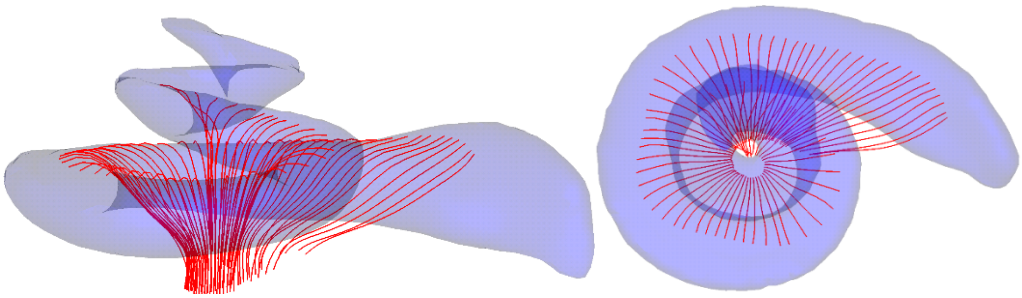

Figure 7.3. Scala tympani (ST) and segmented auditory nerve fibers are shown in blue and red, respectively.

7.2.6. Physiological CI measurements

The amplitude of an eCAP is measured by the difference between the negative and positive peaks. There are several methods to measure eCAPs using cochlear implants, the first of which is the alternating polarity (AP) method where eCAP is measured as the average response from the auditory nerves when both cathodic and anodic current pulses are used. The AGF measurements were collected using the AP method (see Figure 7.4). An intra-cochlear electrode is chosen as the active electrode that injects both cathodic and anodic pulses. The amplitude of the injected current is increased at each step and the step intervals are chosen such that the activated auditory nerve fibers can return to their resting state. For each patient, AGF measurements were taken for all the

active electrodes, and 10 current levels increasing incrementally were injected into the cochlea ranging from 20 μA to maximum amount of current deemed comfortable but loud by the patient.

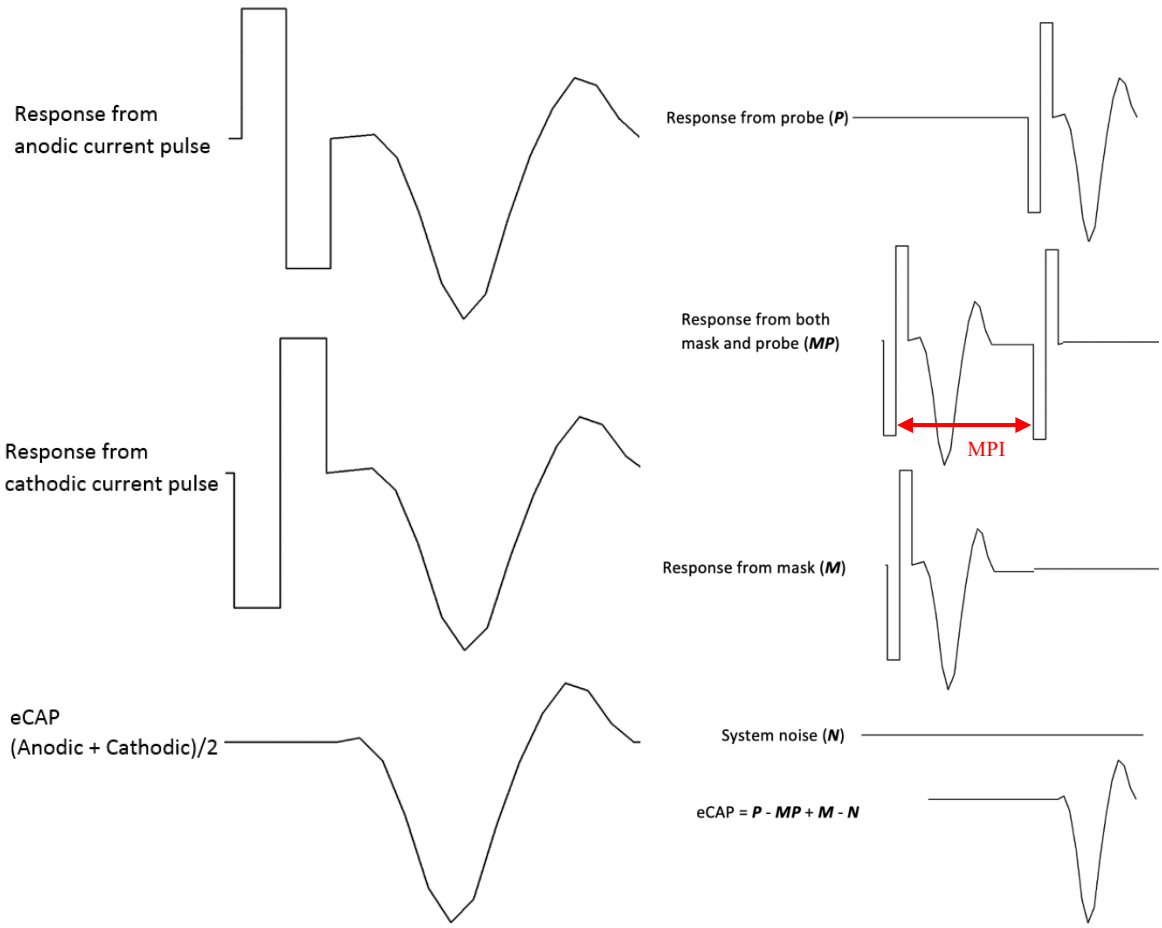

(a) (b)

Figure 7.4. Explanation of the forward-masking subtraction (FMS — (a)), and the alternating polarity (AP — (b)) method. Figures extracted from [19].

These levels were clinically chosen by the audiologists. Finally, eCAP measured at each step as the difference between the negative and the positive peaks, is plotted with respect to the injected amount of current at that step (see Figure 7.5).

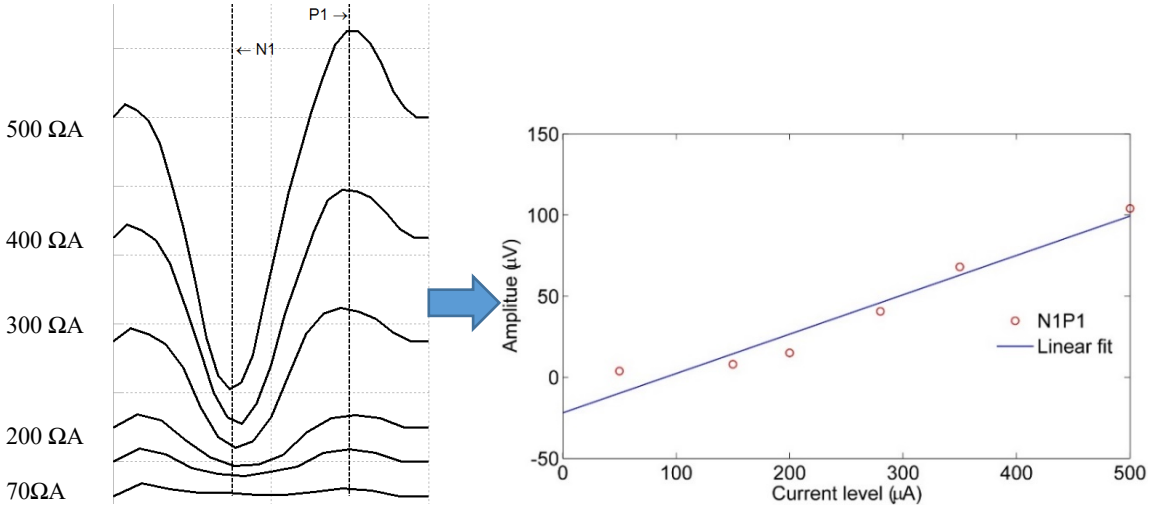

Figure 7.5. An example of amplitude growth function (AGF).

Another method that is used to measure eCAPs is the forward-masking subtraction (FMS) method which takes advantage of the physiological properties of the auditory nerves in order to extract eCAP data (see Figure 7.4). In FMS, two distinct pulses are used, namely masker and probe pulses, which are injected into the cochlea with a masker-probe interval (MPI – see Figure 7.4). When the MPI is sufficiently short, the nerve fibers that are activated by the masker will be in refractory state when the probe pulse is injected. In order to extract the neural response data created by the probe, the recorded responses from the individual masker and probe pulses will be added from which the recorded data for when masker and probe are used together as well as the system noise will be subtracted, resulting in the eCAP signature. By keeping the probe electrode constant and varying the masker electrode, the overlapping excitation fields between different electrode pairs can be calculated, which is referred to as the spread of excitation (SOE) function. The SOE function represents the relative amount of overlapping auditory nerve fibers that are activated by both the masker and the probe. SOE function is expected to increase as the spatial distance between the masker and the probe electrode decrease and vice versa (see figure 7.6) The SOE data were

measured for each pair of active electrodes injecting an amount of current deemed comfortable but loud by the patient while being within the compliance limits.

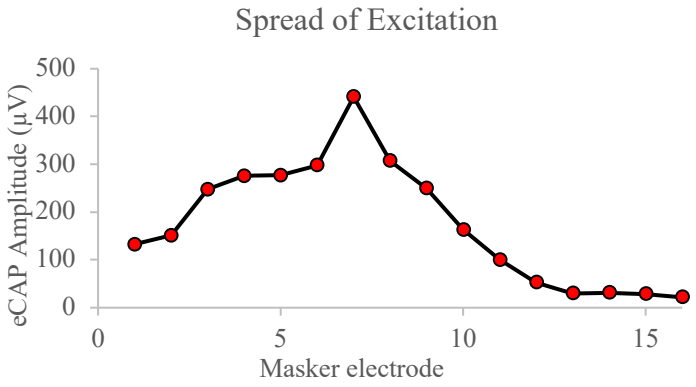

Figure 7.6. Spread of excitation (SOE) function for probe electrode number 7.

7.2.7. Nerve model customization

A healthy human being is assumed to have around 30,000 auditory nerve fibers[35], which are represented with 75 nerve bundles in our ANFM. Thus, for a healthy human being, each of these nerve bundles roughly contain 400 fibers. We can model the health of each nerve bundle by varying the number as well as the ratio of myelinated vs unmyelinated fibers a bundle contains. The myelination ratio is defined as the ratio of the fibers in a bundle with myelinated peripheral axons to those with unmyelinated peripheral axons (see Figure 7.2) We refer to this process of determining the health of an auditory nerve bundle as auditory nerve health imaging (ANHI) and propose to calculate it as shown below:

$$ANHI_i = N_{i_{Healthy}} * \left[0.5 + {Ratio_{i_{Myelinated}}}/{2}\right] \tag{7.9}$$

where N_i and $Ratio_i$ are the number and ratio of nerve fibers in a given bundle i. The Equation

7.9 indicates that when the number of healthy fibers in a bundle is bigger than 0, the estimated ANHI is the average of the total and myelinated number of fibers in that bundle. However, when the number of healthy fibers is 0, then the estimated ANHI will be 0 regardless of the myelination ratio.

The health of such bundles can be parameterized in order to minimize the difference between simulated and measured AGF and SOE values. Auditory neural survival has been shown to be highly variable among subjects with profound hearing loss[38–41]. Thus, we customize each nerve model to the patient in order to estimate patient-specific ANHI. We define n+1 control points along the cochlea where n is the total number of active electrodes. One control point is placed at the basal part and another is placed at the apical part of the cochlea. The remaining n-1 points are placed midway between every consecutive electrode pair. In [23] Spoendlin et al. found that for a healthy human cochlea, average number of fibers can vary between 500 fibers per millimeter (mm) to 1400 fiber per mm depending on the location within the cochlea. Given that a nerve bundle in our model can represent a region as wide as 0.4 mm, we have set the boundary values for number of healthy nerve fibers to be between 0 (completely dead) and 550 (completely healthy). The n+1 control points were initially randomly assigned weights between 0 and 550 and myelination ratios between 0 and 1. The weight of each control point corresponds to the number of nerve fibers within a bundle, and the myelination ratio corresponds to the ratio of the fibers whose axons are myelinated. The weight and myelination ratio of each nerve bundle is linearly interpolated along the length of the cochlea using the n+1 control points. The summary of the algorithm is shown in Algorithm 7.1.

As shown in the algorithm above, we use a modified version of the unconstrained Nelder-Mead optimization algorithm[42]. The cost function is calculated as the mean of the sum of the

difference between the simulated and measured AGF values and the measured and the simulated SOE values only for when the probe and the masker are the same electrodes. We chose to use SOE as well as AGF measurements in our cost function because the AGF and SOE data are calculated using two different methods, AP and FMS, respectively. Thus, using the SOE measurement provides information that is not available only with AGF. We chose to use the SOE data points only for when the masker and the probe are the same so that the remaining SOE data points can be used to test and quantify the accuracy of our optimization algorithm.

Algorithm 7.1. Estimate the patient specific ANHI

Input: $\mathbf{P_{AGF}}$ = Patient AGF measurement, $\mathbf{P_{SOE}}$ = Patient SOE measurement
Variables: $\mathbf{S_{AGF}}$ = Simulated AGF data, $\mathbf{S_{SOE}}$ = Simulated SOE data, $\mathbf{H_{NB}}$ = Number of nerve fibers within bundles, $\mathbf{M_{NB}}$ = Myelination ratio of fibers within bundles
Output: $\mathbf{WC_{NB}}$ = Weight assigned to each control point, $\mathbf{MC_{NB}}$ = Myelination ratio assigned to each control point
Start: Assign threshold and maxIteration, randomly assign $\mathbf{WC_{NB}}$ and $\mathbf{MC_{NB}}$
While Δ | *error*| > threshold and counter < maxIteration
  Interpolate $\mathbf{H_{NB}}$ and $\mathbf{M_{NB}}$ using $\mathbf{WC_{NB}}$ and $\mathbf{MC_{NB}}$
  Calculate $\mathbf{S_{AGF}}$ and $\mathbf{S_{SOE}}$ using $\mathbf{H_{NB}}$ and $\mathbf{M_{NB}}$
  For each electrode i = 1:16
    $error_{\mathbf{AGF}}$ [i] = mean(abs($\mathbf{P_{AGF}}$ [i] - $\mathbf{S_{AGF}}$ [i]))
    $error_{\mathbf{SOE}}$ [i] =abs*(* $\mathbf{P_{SOE}}$ [i][i] - $\mathbf{S_{SOE}}$ [i][i])
  error = mean($error_{\mathbf{AGF}} + error_{\mathbf{SOE}}$*)*
  Optimize $\mathbf{WC_{NB}}$ and $\mathbf{MC_{NB}}$ using a constrained nonlinear search algorithm based on Nelder-Mead simplex
  counter++

AGF values that were less than 50 μA were not included in the training process because low AGF values tend to be noisy and are usually excluded from clinical threshold calculations. Given that AGF and SOE responses carry information regarding two different stimuli, i.e. cathodic and anodic, equal weights were assigned to these measurements in the training process. For each patient, the neural optimization step is run 250 times each time with a different starting point. The final weight and the myelination ratio for each nerve bundle is determined as the median values using the results with the 10 lowest *average error*. This procedure diminishes the likelihood of

choosing a sub-optimal local minima over another given that there can be several local minima that equally minimize the difference between the simulated and measured data.

7.2.8. Clinical ANFM verification

In order to test the validity of our patient-specific EAM, we have clinically conducted a channel discriminability task and compared the results to our simulation results. Channels are created such that when a sound from a pre-determined filter bank is received, the corresponding channel is activated. In CIs, different stimulation techniques can be used to create different channels, such as monopolar, bipolar, tripolar, virtual, etc[43–45]. In the case of monopolar channel, a single electrode is used to inject current into the cochlea, whereas in bipolar and tripolar channels, in addition to the current injecting electrode, one or two neighboring electrodes are used to pull current from the system, respectively. Virtual channels (VC) on the other hand differ from other stimulation techniques in that two electrodes rather than one are used to inject current into the system. Different virtual channels assumed to activate different regions of the cochlea can be created by changing the ratio of currents injected from two neighboring electrodes. It has been shown that as many as 7 *virtual channels* could be created between each pair of intra-cochlear electrodes using Advanced Bionics CI[46]. An example explaining different stimulation techniques is shown in Figure 7.7.

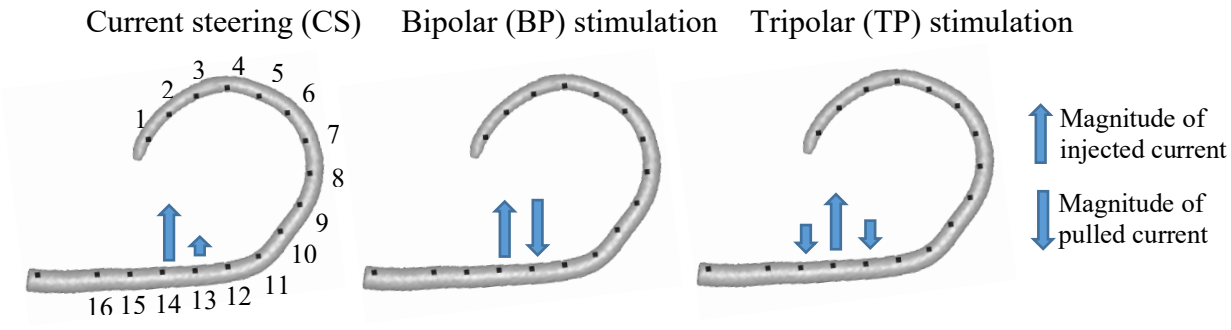

Figure 7.7. Comparison between different stimulation methods.

The goal in performing the channel discrimination test is to determine how difficult it is for a patient to discriminate the perceived sounds created by two distinct neighboring electrodes. In order to clinically measure the discriminability of electrode *x* from electrode *x*+1 or *x*-1, we first created 15 virtual channels between the two neighboring electrodes. These virtual channels were created such that the volume of the perceived sound across different channels is constant and that the region activated by both electrode *x* and VCs is expected to decrease as the channel number increases. Thus, discriminating electrode *x* from VCs gets more difficult as we move from VC #15 to VC #1. The test we have set up is as follows: The patient is presented with 4 'beep' sounds one after the other created using two distinct channels; one being the monopolar channel *x* and the other is one of the VCs. Three out of the 4 sounds have the same pitch and, the patient is asked to find the sound with the different pitch, which is always either the 2nd or the 3rd sound presented. The number of the VC against which the discriminability of monopolar channel *x* is being tested is changed based on the answer of the patient. If the patient is successful twice in a row in identifying the sound with the different pitch, then the number of the VC is decreased, making the discrimination task more difficult. If the patient is unsuccessful, the number of the VC is then increased making the task easier. The task is repeated in an adaptive way with the goal of finding the number of the VC *y* from which the patient has successfully discriminated the monopolar channel *x* with a 67% ratio[48]. The adaptive test is repeated 3 times for each electrode pairs and the final discriminability ratio is calculated as the mean value across all 3 trials. A total of *15* electrode pairs for 4 patients was clinically tested.

The discriminability of different channels is also estimated using the ANFMs. The model estimated discriminability ratio between neighboring electrodes were calculated as follows:

$$D_{x,y} = \frac{\sum_{i=1}^{75} nA_{x,y}^{i}}{\sum_{i=1}^{75} nA_{x}^{i}} \tag{7.10}$$

where $D_{x,y}$ is the discriminability of monopolar channel x from monopolar channel y, nA_x^i is the number of activated nerve fibers in bundle i by monopolar channel x, and $nA_{x,y}^i$ is the number of activated nerve fibers in bundle i by monopolar channels x and y both.

Additionally, neural health estimation of our ANMs were tested. In CI community, the ratio of monopolar to tripolar channel thresholds has been proposed as a surrogate for neural health[47–50]. The higher the ratio between tripolar and monopolar channel thresholds, the lower the number of healthy SG nerve cells located around the active electrode. Thus, linear regression models (LRMs) were created in order to determine the correlation of clinically measured tripolar thresholds with model tripolar thresholds, number of healthy fibers, and myelination ratio.

7.3 Results

7.3.1. Tissue growth

The *average error* for scar tissue growth correction is shown in Table 7.1. As shown in the table, our optimization algorithm did not reveal any tissue growth region for Patient 1 and Patient 4. For the remaining patients, including tissue growth in optimizing the resistivity values lead to either lower (Patient 2, 3, 6, and 7) or equal (Patient 5) *average errors.* Comparisons between the simulated and measured EFI data for Patient 5 before and after the tissue growth correction are shown in Figure 7.8 and 7.9, respectively. The optimization algorithm revealed a relatively large tissue growth region for Patient 5, from electrode 9 to 16. The assumption that the tissue that forms around the electrode array is homogenous might be the reason why the algorithm could not further reduce the *average error* for Patient 5.

Table 7.1. *average error* calculated as the mean difference between simulated and measured EFI values before and after tissue growth correction is shown.

	average error before tissue growth (%)	*average error* after tissue growth correction (%)
Patient 1	4.3	NA
Patient 2	5.1	4.6
Patient 3	9.8	9.5
Patient 4	3.9	NA
Patient 5	6.6	6.6
Patient 6	4.1	3.7
Patient 7	8.2	7.9

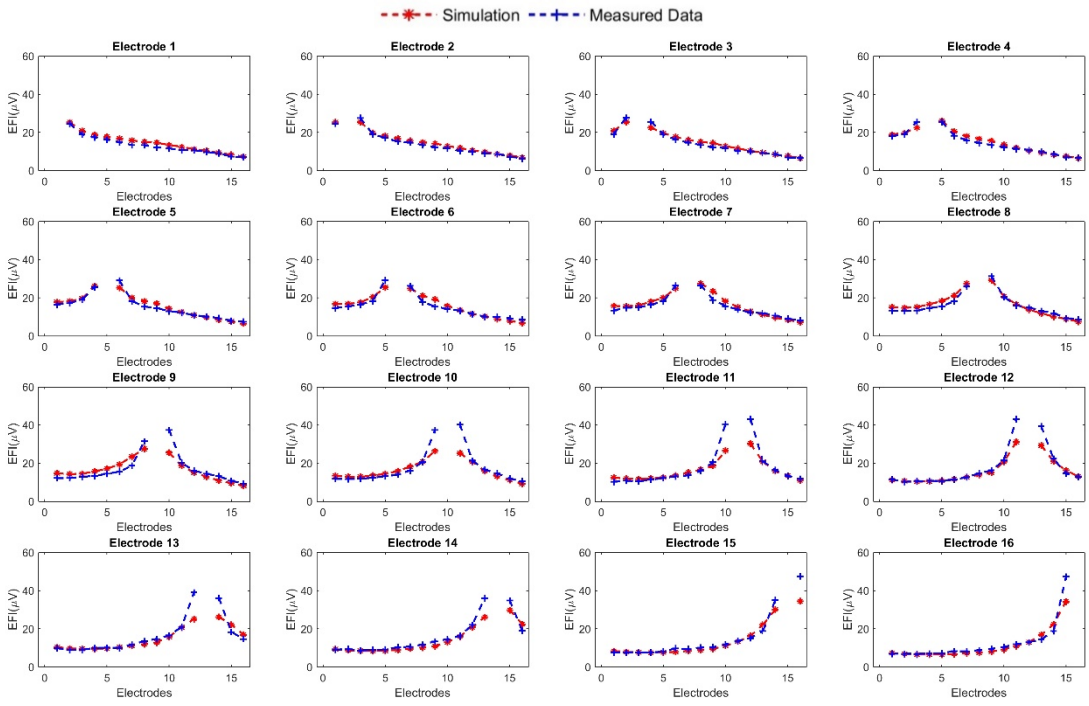

Figure 7.8. Comparison between simulated and measured EFI data before tissue growth correction

In addition, increasing the resolution of the grid might further improve the results. However, our

algorithm is already able to produce results with low *average errors*, and increasing the grid resolution would lead to a quartic increase of the computational cost.

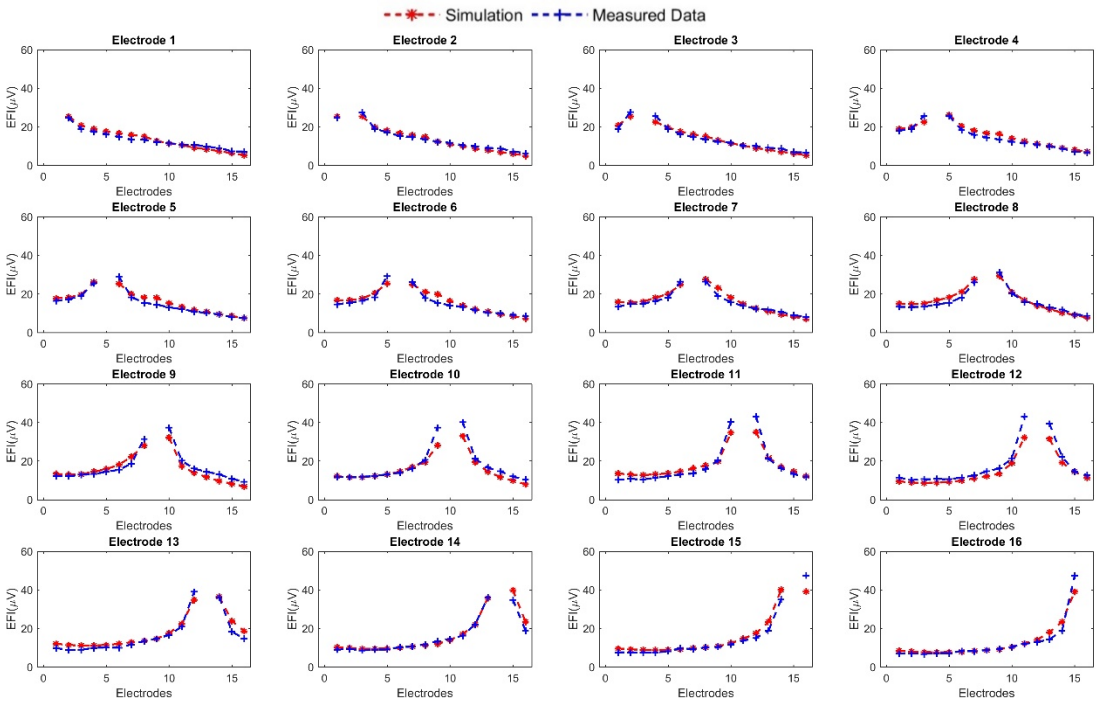

Figure 7.9. Comparison between simulated and measured EFI data after tissue growth correction

7.3.2. Auditory neural health imaging

The average absolute differences between the simulated and measured AGF and SOE values are shown below. It is important to remember that all the available AGF data and the SOE data only for when the same electrode is used to inject both the masker and probe pulses were used in the optimization process. Thus, the average absolute difference between the simulated and the measured AGF values could be interpreted as the *training error,* whereas the error between the simulated and the measured SOE can be interpreted as the *testing error.*

Table 7.2. Average mean absolute difference between simulated and measured training and testing data, AGF and SOE, respectively.

	AGF error - *before customization* (μV)	AGF error - *training* (μV)	SOE error - *testing* (μV)
Patient 1	131	11	29
Patient 2	187	19	32
Patient 3	58	16	33
Patient 4	66	37	44
Patient 5	299	39	37
Patient 6	78	14	35
Patient 7	124	22	52
Average	134.7	22.6	37.4

As shown in the table above, the average difference across all patients for AGF and SOE optimization are 22.6 and 37.4 μV, respectively. A qualitative comparison between simulated and measured training and testing data are shown in Figure 7.10 and Figure 7.11, respectively. Both quantitative and qualitative comparisons show good agreement between the simulated and measured AGF and SOE values. Our optimization algorithm is able to optimize the neural health information and minimize the mean difference between the simulated and measured training AGF data from as high as 187.34 μV to 18.93 μV for Patient 2 (see Table 7.2). Similar results are also found for the testing SOE data, around 90% reduction in mean difference between measured and simulated results for Patient 2. These results are especially remarkable because even though the training data does not contain any information with respect to the overlapping excitation fields

between different electrodes, our model is able to accurately estimate the SOE measurements.

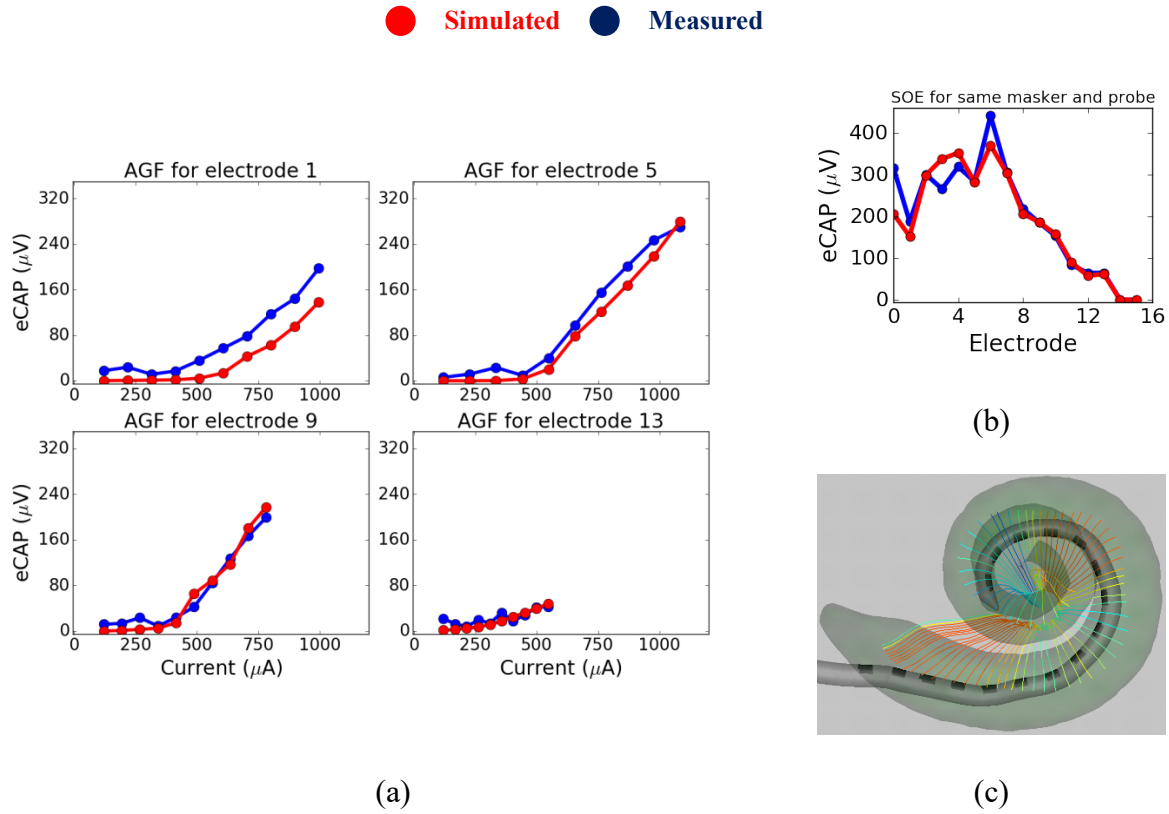

Figure 7.10. Comparison between simulated and measured training data for Patient 1; amplitude growth function (AGF – (a)) and spread of excitation (SOE – (b)). The ANHI estimates are shown in (c). The health of each nerve bundle is color-coded ranging from red (healthy) to blue (unhealthy).

7.2.3. Clinical verification

The resulting clinical discriminability levels, model discriminability ratio as well as average modiolar distance for each pair are shown in Table 7.3. The lower the average clinical discriminability ratio, the less difficult it is for the patient to discriminate $Electrode_1$ from $Electrode_2$. The same principal applies to model discriminability ratio $D_{Electrode_1 Electrode_2}$ as well average modiolar distance. It has been shown in the CI community that the electrode distance is positively correlated with spread of excitation[2]. A correlation coefficient (CC) value was calculated between model estimated and clinically measured discriminability level as well as

average modiolar distance and the clinically measured levels.

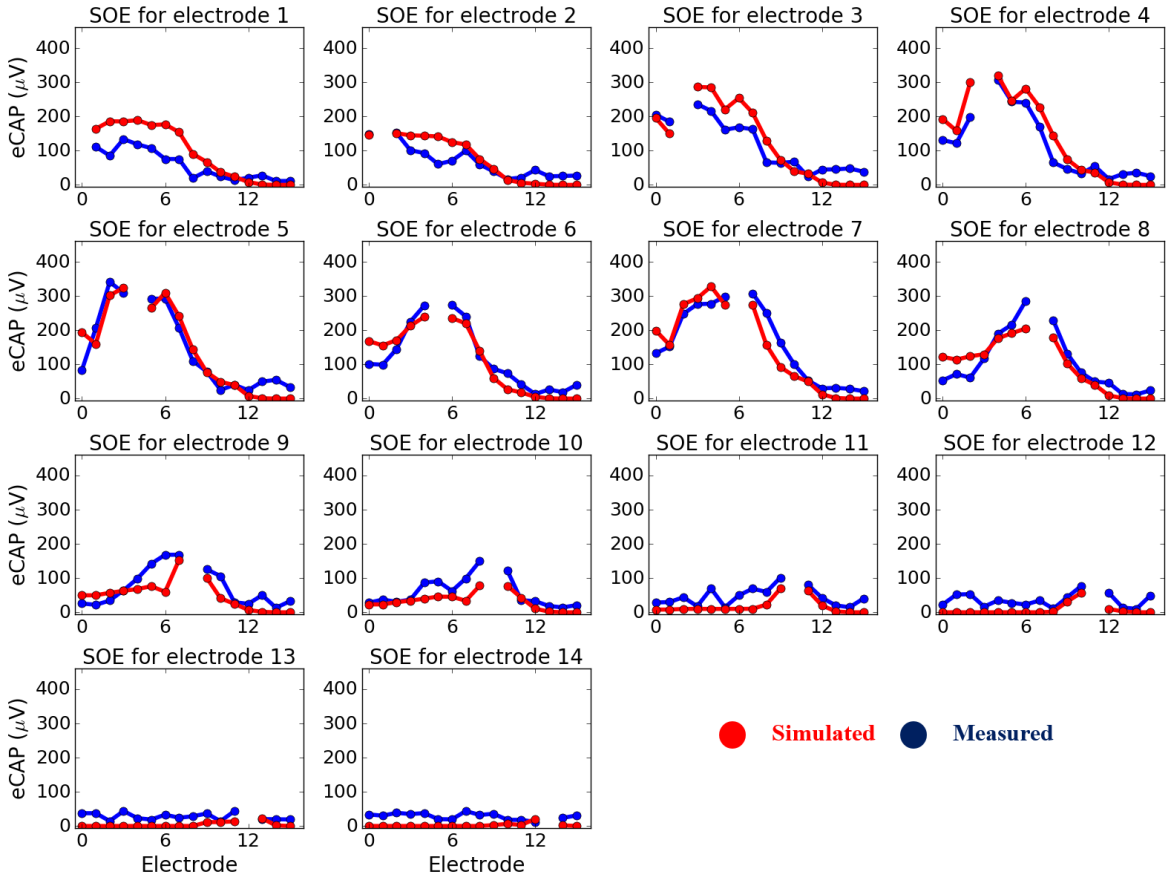

Figure 7.11. Comparison between simulated and measured testing data for Patient 2.

All data were zero centered before the CCs were computed. CC values of *0.69* and *0.4* were found between the model estimates and clinical measurements and between average modiolar distance and clinical measurements, respectively (see Figure 7.12). It has already been showed by Noble et al.[2] that electrode distance can be used as a surrogate in estimating neural activation patterns, which in turn can be used to determine channel interaction artifacts. Electrode pairs with high discriminability ratios are expected to have higher channel interaction artifacts. Clinical studies conducted by the same group have shown that turning off electrodes with high channel interaction artifacts calculated based on the modiolar distance leads to higher hearing outcomes[2]. Our results

indicate that our model discriminability ratio is a better estimate for channel interaction than modiolar distance.

Table 7.3. The resulting clinical discriminability levels, model discriminability ratio as well as average modiolar distance for 15 pairs of clinically tested electrodes.

Patients	Eletrode$_1$	Electrode$_2$	1st trial	2nd trial	3rd trial	Average	$D_{Electrode_1,Electrode_2}$	Average modiolar distance (mm)
Patient 1	7	6	9	7	11	9.0	0.657	0.723
	7	8	5	8	8	7.0	0.717	0.811
	14	13	4	2	2	2.7	0.262	0.432
Patient 2	3	4	2	4	5	3.7	0.949	0.560
	8	9	5	3	2	3.3	0.605	0.825
	10	11	2	4	2	2.7	0.440	0.576
Patient 3	4	3	3	2	3	2.7	0.229	0.082
	7	8	2	2	2	2.0	0.543	0.409
	8	9	5	7	2	4.7	0.639	0.480
	9	8	2	2	4	2.7	0.404	0.480
	9	10	2	3	2	2.3	0.265	0.585
	10	9	2	5	3	3.3	0.639	0.585
Patient 4	3	4	7	11	8	8.7	0.906	0.509
	11	12	12	2	9	7.7	0.468	0.812
	12	13	8	5	5	6.0	0.344	0.542

Thus, we believe that IGCIP techniques would lead to even better hearing scores when model discriminability ratio instead of modiolar distance is used to determine channel interaction artifacts. We have evaluated our ANHI approach using clinical measurements from $N = 5$ patients with varying number of electrodes (see Table 7.4). Data plots revealed a small but consistent shift (1 mm) in the ANHI data relative to the tripolar thresholds, likely due to small inaccuracies in how the model permits flow of electrical current through the round window (see Figure 7.13). In CIs,

the current injected by an intra-cochlear electrode flows to the far ground located by the patient's ear. In our EAM, we simulate the far ground by modeling the entire border of the EAM as ground. The border of an EAM is approximately 5 mm away from the cochlea in each direction (see section 4.3.2). It is possible that the far ground in our model biases the current path toward the apex of the cochlea causing more current than what realistically plausible to escape the cochlea toward the apical end, creating the bias shown in Figure 7.13.

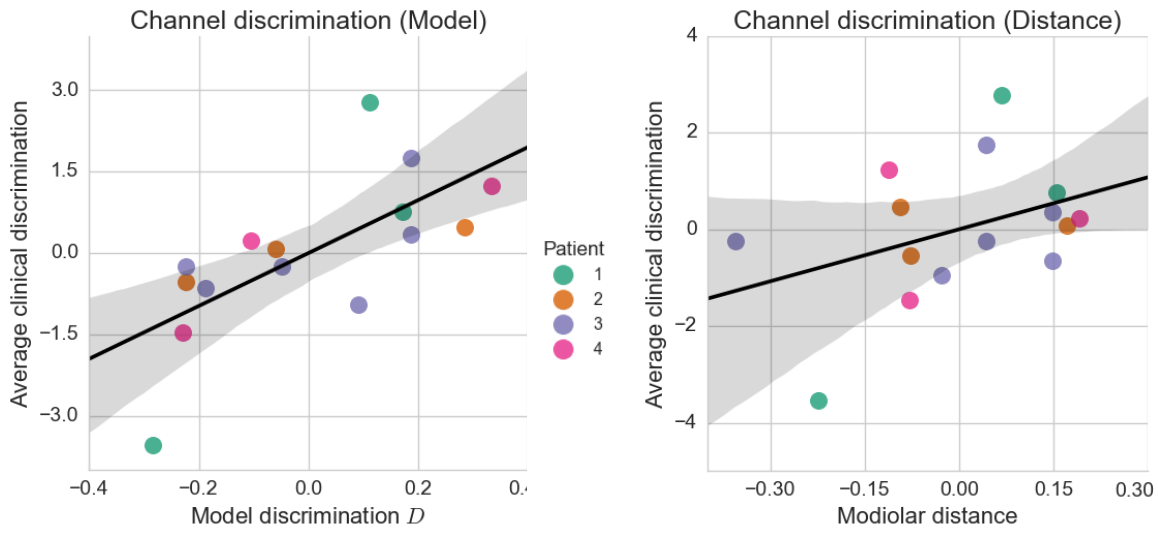

Figure 7.12. Comparison between clinical discriminability levels and model discriminability ratio (left) as well as average modiolar distance (right).

These shifts were corrected in the ANHI data prior to the following analyses. The amount of the shift (1.2 mm) was kept consistent among all patients. An LRM was created using the zero-centered aggregate data in order to determine the correlation of clinically measured tripolar thresholds with modiolar distance, ANHI, model tripolar thresholds, and monopolar thresholds. It has been shown in other clinical studies[49,50,53] that the ratio of tripolar thresholds to monopolar thresholds were correlated with electrode modiolar distance. We also included our ANHI estimates because clinical tripolar thresholds are thought to contain auditory neural health information.

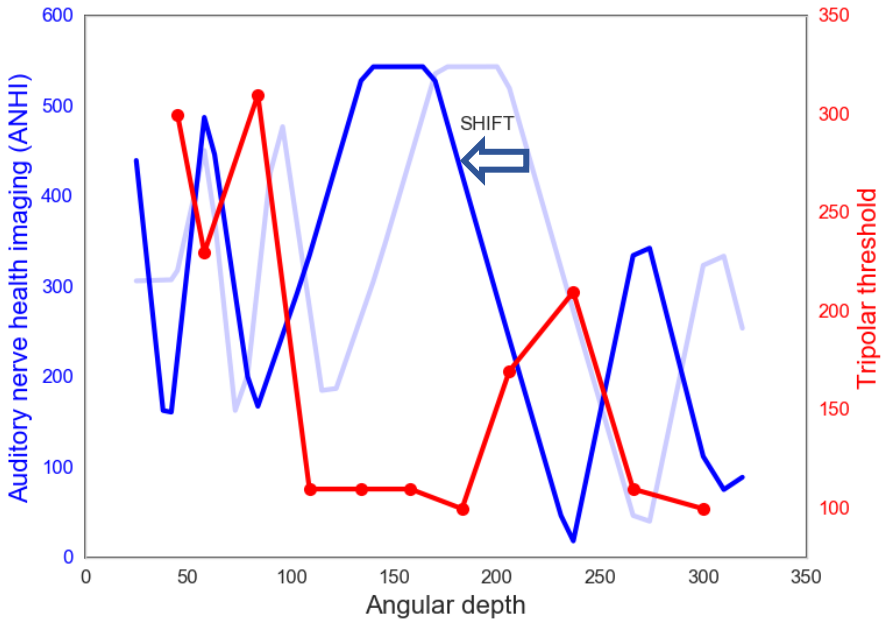

Figure 7.13. ANHI estimates before and after the 1 mm shift correction (blue) as well clinical tripolar thresholds (red) are shown.

Additionally, model tripolar thresholds were included as they provide information that might not otherwise be available via other factors such as voltage profile the along auditory nerve fibers and electrode distance to nodes of Ranvier (see Figure 7.14 – (a)). The correlation of the LRM with aggregated data was $R = 0.28$, and both modiolar distance and ANHI were statistically significant ($p < 0.05$). It is not unexpected that this LRM with only four variables was not able to capture a high degree of variance that exist between different patients. Differences in auditory nerve fiber physiology as well as demographics might be some of such factors that contribute to this variance. Thus, we instead created individual LRMs for each of the patients. The monopolar thresholds were not included in the final LRMs as they were not found to be statistically significant for any of the patients. The LRMs were initially created with factors outlined above, and the factors with *p-values* less than 0.05 were eliminated using backward elimination. For patients where the correlation coefficients between the number of nerve fibers and the myelination ratios were less

than 0.5, these two factors were used instead of ANHI as the two factors might provide more information that is otherwise unavailable with solely ANHI. In addition, the number of nerve fibers and the myelination ratio may be independent for cases where some damage occurred to the peripheral part of the auditory nerve fibers either during or after the insertion and dependent otherwise. The *R* values listed below are the final *R* values computed with only statistically significant factors are shown Table 7.4.

Table 7.4. Final LRMs for all 5 patients after the shift was corrected is shown. * is used to indicate statistically significant factors.

Patients	Number of electrodes tested	p_{ANHI}	$p_{Number\ of\ fibers}$	$p_{Myelination\ ratio}$	$p_{Modiolar\ distance}$	$p_{Model\text{-}threshold}$	R
Patient 1	15	NA	2.4e-02*	2.9e-05*	7.1e-10*	4.4e-01	0.95
Patient 2	13	NA	1.2e-04*	1.1e-01	1.9e-01	7.6e-01	0.50
Patient 3	11	1.8e-09*	NA	NA	1.3-e14*	8.9e-01	0.89
Patient 4	11	2.0e-05*	NA	NA	8.4e-04*	3.2e-02*	0.78
Patient 6	11	NA	1.4e-10*	2.7e-15*	7.5e-08*	2.1e-01	0.93

As expected, either ANHI or number of fibers and/or myelination ratio estimates were negatively correlated with clinical tripolar thresholds for all patients except for Patient 2. The model tripolar threshold as well as modiolar distance on the other hand were not as consistent.

Out of the 5 patients listed above, Patient 1 and Patient 2 had scalar translocations, e.g. the electrode array translocated from the ST into the SV. The translocation occurred around 180-degree depth for both Patient 1 and 2. Patient 1 has 9 electrodes and Patient 2 has 7 electrodes located in the SV. However, these two patients have highly contrasting tripolar threshold profiles (see Figure 7.14). For Patient 1, out of 15 electrodes, we were unable to measure a tripolar threshold for 6 electrodes, from electrode 6 to 11, within the current limitation set by the manufacturer. Thus, these electrodes were not included in the linear regression analyses. As seen

in the figure below, the biggest difference in clinical tripolar thresholds between Patient 1 and 2 occurs around the region where the translocation occurs. For Patient 1, the electrodes that sit in that region have the highest thresholds compared to the other electrodes, whereas for Patient 2, electrodes that sit at where the translocation occurs have the lowest thresholds. This difference might be due to two reasons: (1) Even though both electrode arrays have translocated around the same region, the closest distance from the electrodes around the translocation region to the auditory nerve fibers are relatively different with average distances of 0.49 and 0.37 mm for Patient 1 and 2, respectively. (2) The trauma caused by the electrode array insertion might be different for Patient 1 and 2. Our hypothesis is that the peripheral part of the auditory nerve fibers located between the ST and SV were damaged during or after the insertion for Patient 1 but not for Patient 2. These differences in clinical tripolar thresholds for electrodes around the translocation region were captured by our ANFM where the model tripolar thresholds are highly correlated with clinical thresholds. In addition, our neural health estimate for Patient 1 shows a fairly large region of the cochlea (between 180 and 300 degree-depth) with a low ANHI estimate, whereas the ANHI estimate for Patient 2 is relatively consistent except around 180 degree-depth, which is where the translocation as well as the lowest ANHI estimate occur (see Figure 7.14). As shown in Figure 7.14, the ANHI estimate for Patient 2 between 30 and 150 degree-depth is noisy even though the clinical tripolar thresholds are relatively consistent for when the closest distance to the auditory nerve fibers is controlled. The closest distance from the electrodes to the auditory nerve fibers is the lowest for the 8^{th} electrode sitting at 144 degree-depth and gradually increases for the electrodes sitting more apically and basally. Controlling for the smoothness of the ANHI estimate would allow us to more consistently estimate the auditory health in such regions where the neural health is relatively consistent, and might increase the variance explained by our LRM for Patient 2. For

Patient 1, our model estimates that there is a 'dead region' where the 2 most apical electrodes sit. Less accurate results are expected here because we do not have any clinically measured AGF data for these electrodes. Thus, our algorithm could find many different solutions around the last 3 electrodes and in this case likely erroneously found these apical 2 electrodes to sit near a dead region.

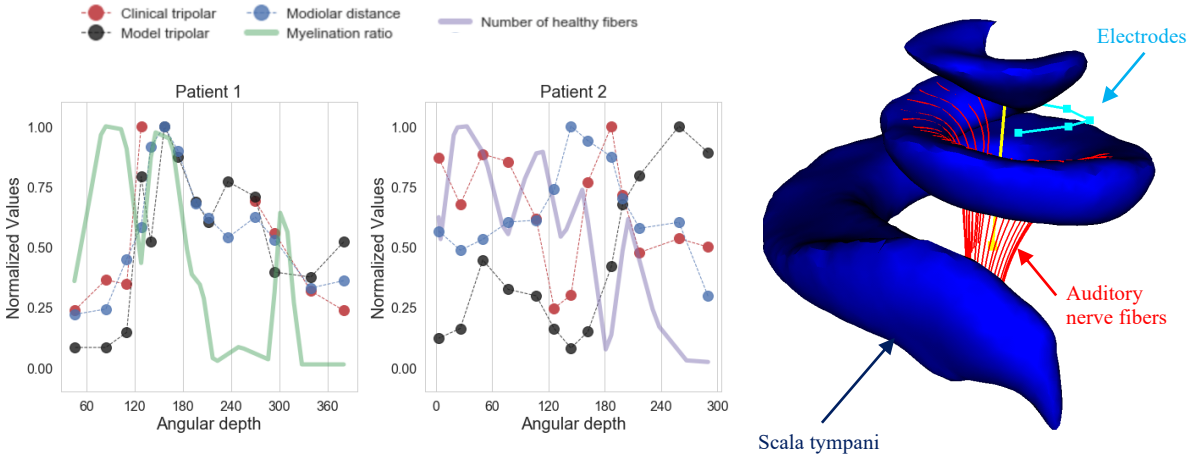

(a) (b)

Figure 7.14. Comparison between different factors as well as clinical tripolar thresholds are shown in for Patient 1 and 2 in (a). The scala tympani, electrodes and auditory nerve fibers are shown in blue, cyan and red in (b). Additionally, an example of the auditory fiber with the shortest distance to the most apical electrode is shown in yellow.

For both Patient 1 and 2, correlation between the model tripolar thresholds and the clinical measurements is lower for the 2 most apical electrodes. This could be because the auditory nerve fibers in our model are only segmented to be between the RW and the 2nd turn of the cochlea (720 degree-depth). In the case of a translocation, a more extreme version of a cross-turn stimulation might occur, e.g. an electrode located at the 1st turn of the cochlea (360 degree-depth) might stimulate auditory nerve fibers that sit beyond the 2nd turn of the cochlea, given that the closest SG

nerve cells to the translocated most apical electrodes would be located within the bundles that sit closer to the third turn of the cochlea.

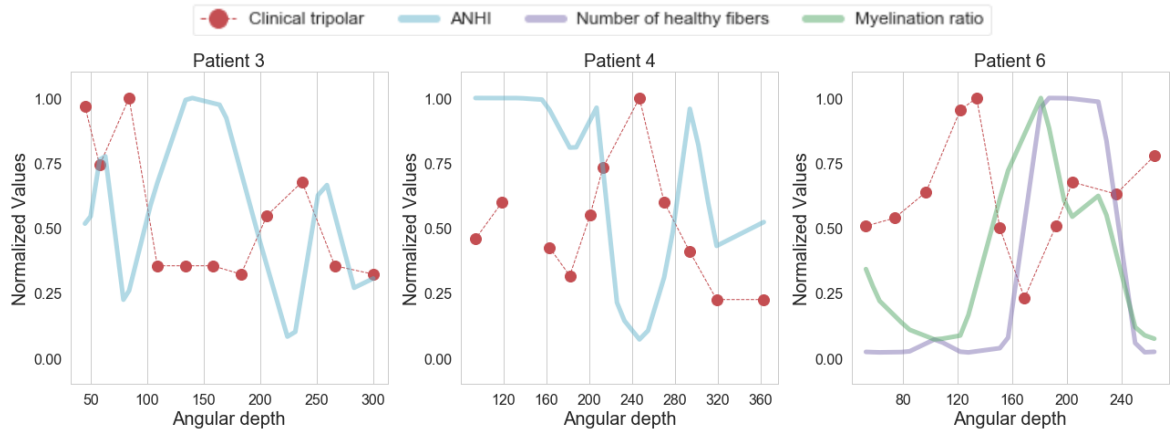

Figure 7.15. Comparison between estimated auditory health information and clinical tripolar thresholds for Patient 3, 4, and 6.

Clinical tripolar thresholds as well as ANHI estimates for Patient 3, 4, and 6 are shown in Figure 7.15. As shown in the figure above, there is a high correlation between the model neural health estimate and the clinical tripolar thresholds. As expected, when the model neural health estimate is low, the measured tripolar thresholds are high, and vice versa. We have omitted the clinical tripolar threshold for Patient 4 electrode #11 from LR analyses as it was not possible to measure the threshold within the current limits set by the manufacturer. And, as shown in the figure, our model is not able to accurately predict the possible neural dead spot located around 11th electrode. In addition, this difference in thresholds between the 11th and its neighboring electrode was not captured by the ANFM model. Thus, the linear model's predictability would be slightly worse were we to include a high threshold for electrode #11.

7.2.3. Sensitivity of ANHI to EAM resistivity values

The grid search algorithm used in optimizing the resistivity values of different tissue types produces several local minima that provide a good fit between simulated and measured EFI values. We examined the effect of choosing different sets of resistivity values on ANHI by randomly choosing 5 out of 30 sets of resistivity values with the lowest *average error,* and comparing the estimated ANHI across these different sets. Coefficient of variation (CoV) between the ANHI estimates are shown in the table below:

Table 7.5. Coefficient of variation (CoV) values between the ANHI estimates for when 5 different sets of resistivity values were used in creating the electro-anatomical models (EAMs).

	Patient 1	Patient 2	Patient 3	Patient 4	Patient 5	Patient 6	Patient 7
CoV	0.299	0.257	0.199	0.197	0.313	0.358	0.269

As shown in the Table 7.5, the CoV values between the different sets of resistivity values are relatively low. In addition to calculating the CoV values, we also created LRMs using ANHI estimates when different sets of resistivity values were used. The results for Patient 6 where the CoV value is the highest is shown in Figure 7.16 and in Table 7.6. These results indicate that our ANHI estimates are relatively insensitive to the selection of resistivity values. However, as shown on the figure, the ANHI estimate between 200 and 400 degree-depth is noisy. Thus, adding a smoothness factor to the optimization step would further lower the CoV values between the different sets of resistivity values and increase the consistency amongst different ANHI estimates.

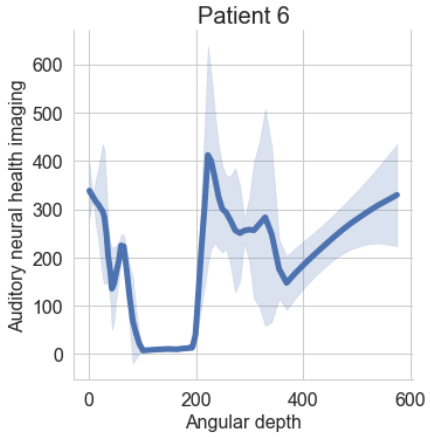

Figure 7.16. Mean and standard deviation ANHI estimates are shown in solid blue line and shaded region, respectively.

Table 7.6. 5 different sets of resistivity values used in creating electrode-anatomical models (EAMs) as well as the *R* values for LRMs created with 1 mm shift is shown.

	Soft tissue (Ωcm)	Electrolytic fluid (Ωcm)	Bone (Ωcm)	Neural tissue (Ωcm)	*R*
Set #1	61	25	3071	676	0.78
Set #2	64	25	3181	509	0.91
Set #3	58	23	3476	463	0.82
Set #4	82	29	2881	391	0.83
Set #5	101	20	2520	554	0.76

7.4 Conclusion

This work represents the first approach for *in-vivo* estimation of the health of auditory nerve fiber bundles for cochlear implant recipients. Our clinical validation results demonstrate the validity of our ANHI estimates and confirm that tripolar thresholds contain neural health information. After integrating neural health, our models permit accurate prediction of psychophysical measurements with an average CC of R=0.81 for the first five subjects we have evaluated. In addition, our results show that the model discriminability ratios that we propose in this chapter has a higher CC with clinically measured discriminability ratios (R = 0.69) than average modiolar distances (R = 0.4*)*, which has been the standard factor used thus far enabling patient-specific programming parameters that lead to better hearing outcomes.

ANHI provides an estimate of which specific fiber bundles are healthy. Further, our models can estimate which fiber bundles are activated for any electric stimulus, permitting comprehensive CI simulation. This breakthrough could provide an unprecedented window into the health of the inner ear, opening the door for studying population variability and intra-subject neural health

dynamics. It could further potentially transform the CI rehabilitation process by permitting comprehensive subject-specific simulation and optimization of the neural stimulation strategy based on the health of the electro-neural interface. Ultimately, we envision these models will not only permit design and implementation of novel patient-customized programming strategies, but also may provide further insight into factors that affect patient outcomes.

References

1. Clark G. Cochlear Implants. In: Greenberg S, Ainsworth WA, Popper AN, Fay RR, eds. *Speech Processing in the Auditory System*. Springer Handbook of Auditory Research. New York, NY: Springer New York; 2004:422-462. doi:10.1007/0-387-21575-1_8

2. Noble JH, Labadie RF, Gifford RH, Dawant BM. Image-guidance enables new methods for customizing cochlear implant stimulation strategies. *IEEE Trans Neural Syst Rehabil Eng*. 2013;21(5):820-829. doi:10.1109/TNSRE.2013.2253333

3. Noble JH, Gifford RH, Hedley-Williams AJ, Dawant BM, Labadie RF. Clinical evaluation of an image-guided cochlear implant programming strategy. *Audiol Neurootol*. 2014;19(6):400-411. doi:10.1159/000365273

4. Noble JH, Hedley-Williams AJ, Sunderhaus L, et al. Initial Results With Image-guided Cochlear Implant Programming in Children. *Otol Neurotol*. 2016;37(2):e63-69. doi:10.1097/MAO.0000000000000909

5. Rattay F. Analysis of models for external stimulation of axons. *IEEE Trans Biomed Eng*. 1986;33(10):974-977. doi:10.1109/TBME.1986.325670

6. Finley CC, Wilson BS, White MW. Models of Neural Responsiveness to Electrical Stimulation. In: Miller JM, Spelman FA, eds. *Cochlear Implants: Models of the Electrically Stimulated Ear*. New York, NY: Springer New York; 1990:55-96. doi:10.1007/978-1-4612-3256-8_5

7. Rattay F, Lutter P, Felix H. A model of the electrically excited human cochlear neuron. I. Contribution of neural substructures to the generation and propagation of spikes. *Hear Res*. 2001;153(1-2):43-63.

8. Nicoletti M, Wirtz Chr, Hemmert W. Modeling Sound Localization with Cochlear Implants. In: Blauert J, ed. *The Technology of Binaural Listening*. Modern Acoustics and Signal Processing. Berlin, Heidelberg: Springer Berlin Heidelberg; 2013:309-331. doi:10.1007/978-3-642-37762-4_12

9. Hanekom T. Three-dimensional spiraling finite element model of the electrically stimulated cochlea. *Ear Hear*. 2001;22(4):300-315.

10. Frijns JH, de Snoo SL, ten Kate JH. Spatial selectivity in a rotationally symmetric model of the electrically stimulated cochlea. *Hear Res*. 1996;95(1-2):33-48.

11. Kalkman RK, Briaire JJ, Frijns JHM. Current focussing in cochlear implants: an analysis of neural recruitment in a computational model. *Hear Res*. 2015;322:89-98. doi:10.1016/j.heares.2014.12.004

12. Kalkman RK, Briaire JJ, Dekker DMT, Frijns JHM. Place pitch versus electrode location in a realistic computational model of the implanted human cochlea. *Hear Res*. 2014;315:10-24.

doi:10.1016/j.heares.2014.06.003

13. Cartee LA. Spiral ganglion cell site of excitation II: numerical model analysis. *Hear Res*. 2006;215(1-2):22-30. doi:10.1016/j.heares.2006.02.011

14. Cartee LA. Evaluation of a model of the cochlear neural membrane. II: comparison of model and physiological measures of membrane properties measured in response to intrameatal electrical stimulation. *Hear Res*. 2000;146(1-2):153-166.

15. Hodgkin AL, Huxley AF. The components of membrane conductance in the giant axon of Loligo. *J Physiol*. 1952;116(4):473-496.

16. Frijns JHM, Briaire JJ, Schoonhoven R. Integrated use of volume conduction and neural models to simulate the response to cochlear implants. *Simulation Practice and Theory*. 2000;8(1):75-97. doi:10.1016/S0928-4869(00)00008-2

17. Frijns JH, de Snoo SL, Schoonhoven R. Potential distributions and neural excitation patterns in a rotationally symmetric model of the electrically stimulated cochlea. *Hear Res*. 1995;87(1-2):170-186.

18. Briaire JJ, Frijns JHM. Unraveling the electrically evoked compound action potential. *Hear Res*. 2005;205(1-2):143-156. doi:10.1016/j.heares.2005.03.020

19. Hughes M. *Objective Measures in Cochlear Implants*. Plural Publishing; 2012.

20. Malherbe TK, Hanekom T, Hanekom JJ. Constructing a three-dimensional electrical model of a living cochlear implant user's cochlea. *Int J Numer Method Biomed Eng*. 2016;32(7). doi:10.1002/cnm.2751

21. Cakir A, Dawant BM, Noble JH. Development of a $$\upmu $$CT-based Patient-Specific Model of the Electrically Stimulated Cochlea. In: Descoteaux M, Maier-Hein L, Franz A, Jannin P, Collins DL, Duchesne S, eds. *Medical Image Computing and Computer Assisted Intervention − MICCAI 2017*. Lecture Notes in Computer Science. Springer International Publishing; 2017:773-780.

22. Cakir A, Dwyer RT, Noble JH. Evaluation of a high-resolution patient-specific model of the electrically stimulated cochlea. *J Med Imaging (Bellingham)*. 2017;4(2):025003. doi:10.1117/1.JMI.4.2.025003

23. Spoendlin H, Schrott A. Analysis of the human auditory nerve. *Hear Res*. 1989;43(1):25-38.

24. Mens LHM. Advances in cochlear implant telemetry: evoked neural responses, electrical field imaging, and technical integrity. *Trends Amplif*. 2007;11(3):143-159. doi:10.1177/1084713807304362

25. Whiten DM (Darren M. Electro-anatomical models of the cochlear implant. 2007. http://dspace.mit.edu/handle/1721.1/38518. Accessed April 10, 2019.

26. Eisen MD, Franck KH. Electrically evoked compound action potential amplitude growth functions and HiResolution programming levels in pediatric CII implant subjects. *Ear Hear*. 2004;25(6):528-538.

27. Cohen LT. Practical model description of peripheral neural excitation in cochlear implant recipients: 1. Growth of loudness and ECAP amplitude with current. *Hear Res*. 2009;247(2):87-99. doi:10.1016/j.heares.2008.11.003

28. Noble JH, Labadie RF, Majdani O, Dawant BM. Automatic segmentation of intracochlear anatomy in conventional CT. *IEEE Trans Biomed Eng*. 2011;58(9):2625-2632. doi:10.1109/TBME.2011.2160262

29. Bookstein FL. Principal warps: thin-plate splines and the decomposition of deformations. *IEEE Transactions on Pattern Analysis and Machine Intelligence*. 1989;11(6):567-585. doi:10.1109/34.24792

30. Press WH, Teukolsky SA, Vetterling WT, Flannery BP. *Numerical Recipes 3rd Edition: The Art of Scientific Computing*. Cambridge University Press; 2007.

31. Choi C-H, Oghalai JS. Predicting the effect of post-implant cochlear fibrosis on residual hearing. *Hearing Research*. 2005;205(1):193-200. doi:10.1016/j.heares.2005.03.018

32. Hanekom T. Modelling encapsulation tissue around cochlear implant electrodes. *Med Biol Eng Comput*. 2005;43(1):47-55. doi:10.1007/BF02345122

33. Wilk M, Hessler R, Mugridge K, et al. Impedance Changes and Fibrous Tissue Growth after Cochlear Implantation Are Correlated and Can Be Reduced Using a Dexamethasone Eluting Electrode. *PLoS ONE*. 2016;11(2):e0147552. doi:10.1371/journal.pone.0147552

34. Keithley EM, Chen MC, Linthicum F. Clinical diagnoses associated with histologic findings of fibrotic tissue and new bone in the inner ear. *Laryngoscope*. 1998;108(1 Pt 1):87-91.

35. Kamakura T, Nadol JB. Correlation between word recognition score and intracochlear new bone and fibrous tissue after cochlear implantation in the human. *Hear Res*. 2016;339:132-141. doi:10.1016/j.heares.2016.06.015

36. Gray H, Carter HV. *Anatomy of the Human Body*. 20th ed. / thoroughly rev. and re-edited by Warren H. Lewis. Philadelphia: Lea & Febiger; 1918.

37. Cakir A, Labadie RF, Noble JH. Auditory nerve fiber segmentation methods for neural activation modeling. In: *Medical Imaging 2019: Image-Guided Procedures, Robotic Interventions, and Modeling*. Vol 10951. International Society for Optics and Photonics; 2019:109511K. doi:10.1117/12.2513006

38. Dijkstra EW. A note on two problems in connexion with graphs. *Numer Math*. 1959;1(1):269-271. doi:10.1007/BF01386390

39. Linthicum FH, Fayad J, Otto SR, Galey FR, House WF. Cochlear implant histopathology.

Am J Otol. 1991;12(4):245-311.

40. Nadol JB, Shiao JY, Burgess BJ, et al. Histopathology of cochlear implants in humans. *Ann Otol Rhinol Laryngol*. 2001;110(9):883-891. doi:10.1177/000348940111000914

41. Nadol JB. Patterns of neural degeneration in the human cochlea and auditory nerve: Implications for cochlear implantation. *Otolaryngology - Head and Neck Surgery*. 1997;117(3):220-228. doi:10.1016/S0194-5998(97)70178-5

42. Nadol JB, Young Y-S, Glynn RJ. Survival of Spiral Ganglion Cells in Profound Sensorineural Hearing Loss: Implications for Cochlear Implantation. *Ann Otol Rhinol Laryngol*. 1989;98(6):411-416. doi:10.1177/000348948909800602

43. Lagarias JC, Reeds JA, Wright MH, Wright PE. Convergence Properties of the Nelder-Mead Simplex Method in Low Dimensions. *SIAM Journal of Optimization*. 1998;9:112–147.

44. Zhu Z, Tang Q, Zeng F-G, Guan T, Ye D. Cochlear-implant spatial selectivity with monopolar, bipolar and tripolar stimulation. *Hearing Research*. 2012;283(1):45-58. doi:10.1016/j.heares.2011.11.005

45. Bierer JA, Middlebrooks JC. Cortical Responses to Cochlear Implant Stimulation: Channel Interactions. *JARO*. 2004;5(1):32-48. doi:10.1007/s10162-003-3057-7

46. Landsberger DM, Srinivasan AG. Virtual channel discrimination is improved by current focusing in cochlear implant recipients. *Hearing Research*. 2009;254(1):34-41. doi:10.1016/j.heares.2009.04.007

47. Berenstein CK, Mens LHM, Mulder JJS, Vanpoucke FJ. Current steering and current focusing in cochlear implants: comparison of monopolar, tripolar, and virtual channel electrode configurations. *Ear Hear*. 2008;29(2):250-260.

48. Zwolan TA, Collins LM, Wakefield GH. Electrode discrimination and speech recognition in postlingually deafened adult cochlear implant subjects. *J Acoust Soc Am*. 1997;102(6):3673-3685. doi:10.1121/1.420401

49. Bierer JA. Threshold and channel interaction in cochlear implant users: evaluation of the tripolar electrode configuration. *J Acoust Soc Am*. 2007;121(3):1642-1653.

50. Bierer JA, Faulkner KF. Identifying cochlear implant channels with poor electrode-neuron interface: partial tripolar, single-channel thresholds and psychophysical tuning curves. *Ear Hear*. 2010;31(2):247-258. doi:10.1097/AUD.0b013e3181c7daf4

51. Goldwyn JH, Bierer SM, Bierer JA. Modeling the electrode-neuron interface of cochlear implants: effects of neural survival, electrode placement, and the partial tripolar configuration. *Hear Res*. 2010;268(1-2):93-104. doi:10.1016/j.heares.2010.05.005

52. Bierer JA, Nye AD. Comparisons between detection threshold and loudness perception for individual cochlear implant channels. *Ear Hear*. 2014;35(6):641-651.

doi:10.1097/AUD.0000000000000058

53. Long CJ, Holden TA, McClelland GH, et al. Examining the electro-neural interface of cochlear implant users using psychophysics, CT scans, and speech understanding. *J Assoc Res Otolaryngol*. 2014;15(2):293-304. doi:10.1007/s10162-013-0437-5

Chapter VIII

SUMMARY AND FUTURE WORK

This dissertation introduces several innovative biomedical modeling and image processing techniques in order to develop patient-specific electro-anatomical models (EAMs) and auditory nerve fiber models (ANFMs) and clinically verify them. Prior to this dissertation, neural health could only be estimated using generic biomedical models, which we have shown to be less accurate, or by using raw clinical measurements used as a surrogate for neural health, which can only provide information with respect to the region around an electrode unlike bundle-specific estimate our models can provide. This is significant because it could provide an unprecedented window into the health of the inner ear, opening the door for studying population variability and intra-subject neural health dynamics. Further, unlike clinical measurements, our models can estimate which fiber bundles are activated for any electric stimulus, permitting comprehensive CI simulation. This could potentially transform the cochlear implant rehabilitation process by permitting comprehensive subject-specific simulation and optimization of the neural stimulation strategy based on the health of the electro-neural interface. Ultimately, we envision these models will not only permit design and implementation of novel patient-customized programming strategies, but also may provide further insight into factors that affect patient outcomes. In this dissertation we have made several different contributions: (1) we have shown that non-rigid variations in the cochlea across individuals exist and significantly affect electrode localization measurements as shown in Chapter II[1]. Quantifying electrode position accurately is important not only for studying the relationship between electrode positions and hearing outcomes but also for image-guided cochlear implant programming techniques as well as constructing accurate patient-

specific models as they rely on measurements of electrode positions. We have also shown that, as described in Chapter III, manually measuring cochlea length leads to high variance across measurements and significantly impact electrode choice, whereas the automatic method we propose is less time consuming and generates repeatable results[2]. (2) We developed an automatic method to create both anatomically and electrically customized electro-anatomical models which are a necessary step in constructing auditory nerve fiber models[3,4]. These methods are described in Chapter IV and V. (3) Finally, we proposed several methods to create patient-specific auditory nerve fiber models, as described in Chapter VI and VII[5,6]. We use a set of physiological measurements to customize our model to each patient parameterizing neural health and use a different set of measurements to verify our results. We also clinically verify the model estimations.

In Chapter II, we propose a method to quantify the effect of non-rigid variations on electrode localization. First, we create seven rigid models by manually segmenting μCT images of seven different ex-vivo specimens. We also localize the intra-cochlear structures like scala tympani (ST), scala vestibuli (SV) and modiolus in the pre-implantation CT images of 93 patients using the approach described in[7]. We then fit individual rigid models of cochlear anatomy we have created from seven different cochleae to each of the CI ears using well known point-based registration techniques[8]. Finally, we measure the relative position of the electrodes with respect to basilar membrane, which allows us to determine both the scala, either scala tympani or scala vestibuli, in which the electrode is located as well as the proximity of the electrode to the neural activation sites. Standard deviations of electrode position measures across rigid models are relatively high (0.11 mm relative to basilar membrane and 0.15 mm relative to neural activation sites), and lead to potentially different findings regarding the scalar position of electrodes and their proximity to the modiolus depending on which rigid model is used. The rigid models disagreed on

scalar position for 19% of the electrodes in our dataset and on modiolar proximity for 50% of the electrodes. These results motivate the use of non-rigid models of cochlear anatomy and indicate the importance of capturing non-rigid variations.

In Chapter III, we describe two different automatic methods we developed to measure cochlea duct length and compare the results to other measurement techniques. Briefly, the first method involves directly measuring the cochlea duct length at two turns, denoted as $CDL_{Direct\text{-}Auto}$. We map the cochlea duct points defined along the outer wall of the cochlea in a cochlea model to each patient then measure the length of the curve from round window to two-turns. The second method involves measuring the length *A*, defined as the length of the line from the center of the round window through the modiolus to the farthest point on the lateral wall of the basal turn of the cochlea. The Equation 3.1, proposed by Escude et al.[9], can be used to calculate the length of the cochlear duct along the outer wall from the center of round window to a specific angular depth. We have measured length *A* both automatically, denoted as A_{Auto}, and manually, performed by two trained neurotologists denoted as A_{S1} and A_{S2}. In addition to comparing direct and indirect cochlear duct length measurements, we also investigated the effect of these measurement techniques on electrode array selection. We found significant differences between different measurements of length *A* as well as cochlear duct length. On the other hand, our analyses showed that the difference between $CDL_{Direct\text{-}Auto}$ and indirect cochlear duct length measurement is minimum when A_{Auto} is used, denoted as $CDL_{A\text{-}Auto}$, resulting in a mean and maximum difference of 0.27 and 1.35 mm, respectively. The same measurements between $CDL_{Direct\text{-}Auto}$ and indirect measurements when either A_{S1} or A_{S2} is used, denoted as CDL_{S1} and CDL_{S2}, on the other hand, have relatively high values, with mean absolute differences greater than 1.4 mm. $CDL_{Direct\text{-}Auto}$ or $CDL_{A\text{-}Auto}$ measurements resulted approximately in the same electrode array type selections, with the biggest

difference of 38 ears out of 309 occurring when a threshold value of 9.74 mm was used to choose between two different electrode array types. Manual measurements by the first and second surgeon, on the other hand, led to a larger number of differences in the selected electrode array type between each other and the automated measures. Measuring *A* and CDL automatically is less time consuming and generates more repeatable results. Our automatic approach could make the use of CDL for patient-customized treatment more clinically adoptable.

In Chapter IV, we propose our method that could be used to create electro-anatomical models (EAMs) of electrically stimulated cochlea from μCT images of ex-vivo specimens[10] and then extend this method by projecting such high-resolution EAMs to patient CT space[4]. This allows us to create *in-vivo* EAMs from patient CT images that are anatomically customized to the shape of individual cochlea. Briefly, we use μCT images of ex-vivo specimens to create high resolution resistivity maps, which are tissue class label maps used to define the electrical resistivity of the tissue in the image, which are then projected onto the patient CT image using thin-plate splines (TPS)[11]. A combined resistivity map is created using a majority voting scheme between all of the possible resistivity maps. Using the combined resistivity map and the patient's known electrode position, a patient-specific model is created. A system of linear equations was created to solve Poisson's equation for electrical current, as shown in Equation 4.1. Finally, patient-specific neural activation is estimated as the current density profile (CDP) along Rosenthal's Canal (RC), which is where spiral ganglion nerve cells are located. In order to evaluate the accuracy of our patient-specific models, we also created generic models using leave-one-out strategy and compared the patient-specific and generic CDPs to the ground truth CDPs. The average accuracy of our patient-specific model was found to be 81.2% compared to 77.4% for the generic models. In addition, the minimum accuracy of the patient-specific model 76.9% was relatively higher than

that of the generic model, 66.8%. In general, models created using manual anatomy localizations were more accurate than those created using automatic anatomy localizations. Quantitative analysis of the results indicate that patient-specific models are on average more accurate than generic models, which is currently the community standard approach. These results motivate the use of patient-specific models.

In Chapter V, we extend our patient-specific EAM by developing an optimization algorithm that customizes the resistivity values assigned to different tissue classes in order to minimize the difference between simulated and measured physiological measurements, namely electric field imaging (EFI). EFI is the simultaneous measurement of the voltage values across the electrode array when one electrode at a time is used to inject current into the cochlea. In this chapter, we present an automatic heuristic search algorithm which leverages our knowledge of how changes in the resistivity values of different tissue types affect the simulated voltage distribution. We found that a change in the electrolytic fluid resistivity has negligible effects, whereas a change in the resistivity values of soft tissue and neural tissue have different effects. The principal effect when changing the soft tissue resistivity value is a change in the average value of the voltage distribution across electrodes while the shape of the voltage distribution maintains the same slope. Changing neural tissue resistivity value on the other hand sharpens or flattens the curve, i.e., a decrease in the neural tissue resistivity value will result in a flattening of the curve and vice versa. Using this information, the resistivity values assigned to soft tissue and neural tissue are adjusted based on *average error*, which is the average normalized mean difference between simulation results and the acquired patient data. We have demonstrated our approach for $N = 7$ patients with 6 unilateral and 1 bilateral implants. The search algorithm was able to converge in 22 iteration on average, and the mean *average error* dropped from 45.0% to 10.9%.

In Chapter VI, we introduce a graph-based search algorithm to segment the auditory nerve fibers. Our goal was to evaluate techniques for segmenting auditory nerve fibers to enable neural stimulation modeling and estimation of neural stimulation patterns, and to quantify the effect of fiber segmentation accuracy on neural activation. For this purpose, we developed semi- and fully-automatic techniques for segmenting auditory nerve fibers that will be used in creating ANFMs. Our semi-automatic approach uses path finding algorithms to connect automatically estimated landmarks and models the section of the fibers from the unmyelinated terminal to the internal auditory canal (IAC). Using scala tympani (ST), scala vestibuli (SV) and modiolus, certain structures that provide excellent landmarks for fibers, such as osseous spiral lamina and Rosenthal's Canal, can be determined. The location of IAC endpoints, through which auditory nerve fibers proceed into the IAC, on the other hand cannot be determined using such structures like ST or SV and need to be estimated. Since the location of IAC endpoints will affect the shape of auditory nerve fibers, we completed the semi-automated fiber localization process twice where the IAC endpoints were moved in between trials in a random direction by a maximum amount that still leaves the points within IAC. This allows us to quantify the effect of fiber shape on neural activation. We found that neural activation modeling estimates were not sensitive to moderate changes in fiber shape. The two different sets of auditory fibers had an average Euclidian distance of 0.15 mm, and a neural activation similarity of 83%.

In Chapter VII, we introduce our patient-specific auditory nerve fiber models (ANFMs). The activation of the auditory nerve fibers in our ANFMs is modeled similarly to Rattay et al[12]. Using these models, we can simulate any electric stimulus delivery as well as acquisition of objective measurements, such as electrically evoked compound action potential (ECAP), which allowed us to simulate physiological measurements such as amplitude growth functions (AGFs)

as well as spread of excitations (SOEs). We estimate the health of the ANFs by: (1) parameterizing our ANF models according to neural health; and (2) using a constrained optimization algorithm to tune the neural health of the ANFs in order to minimize the sum of squared differences between simulated and the measured AGFs. We refer to this process of estimating neural health for fibers along the length of the cochlea as Auditory Neural Health Imaging (ANHI). We have evaluated our ANHI approach with 5 patients. Since a comparison of monopolar and tripolar thresholds has been proposed as a surrogate for neural health, linear regression models (LRMs) were created in order to determine the correlation of clinically measured tripolar thresholds with modiolar distance, monopolar thresholds, ANHI, and model tripolar thresholds. LRMs revealed monopolar thresholds to be uncorrelated with tripolar thresholds. However, modiolar distance and ANHI were found to be significantly associated with tripolar thresholds with high LRM average correlation of $R = 0.81$ across the 5 cases. The correlation between modiolar distance alone and tripolar thresholds is $R = 0.48$ on average. In addition, a total of 15 electrode pairs for 4 patients were tested to determine the channel discriminability between each pairs. An average correlation coefficient (CC) of 0.69 was found between the estimated and clinically measured discriminability ratios. The average CC values between the clinically measured discriminability ratios and the average electrode pair distance to the neural activation sites, on the other hand, were 0.4. This work represents the first clinical validation of our patient-specific EAMs. Ultimately, we envision these models will not only permit design and implementation of novel patient-customized programming strategies, but also may provide further insight into factors that affect patient outcomes.

Even though we have made substantial progress in creating patient-specific EAMs and ANFMs, further improvements and clinical verifications are possible. As explained in Chapter VII, data plots revealed a small but consistent shift of around ~1 mm in the ANHI data relative to

the tripolar thresholds. We believe that this is likely due to small inaccuracies in how the model permits flow of electrical current through the round window. In CIs, the current injected by an intra-cochlear electrode flows to the far ground located by the patient's ear. In our EAM, we simulate the far ground by modeling the entire border of the EAM as ground. The border of an EAM is approximately 5 mm away from the cochlea in each direction (see section 4.3.2). It is possible that the far ground in our model biases the current path toward the apex of the cochlea causing more current than what realistically plausible to escape the cochlea toward the apical end, creating the bias shown in Figure 7.13. Another potential cause for the small shift could be the way in which we determine air voxels around the round window unrelated to the surgical procedure. Given that a simple thresholding was used to determine air voxels, which were modeled as perfectly resistive, better segmentations of these voxels might help get rid of the small bias in current paths that seem to be present in our results.

When creating EAMs as explained in Chapter 7.2.3, we have assumed that the only cause to the relatively higher disagreements seen between the measured and simulated EFI values is the tissue growth phenomenon. However, this remains an assumption and the only way to prove it is a post-mortem analysis. In order to independently verify whether our estimate of tissue growth regions is accurate, it would be ideal if patients studied in this thesis were asked to donate their temporal bones to the temporal bone registries at the time of death for a post-mortem histopathology analysis[13,14].

We have verified our EAM and ANFM approach by both comparing simulated physiological measurements, such as EFI, AGF, and SOE, to the measured patient data as well as performing two different clinical tests. We have so far created models for $N = 7$ patients, 5 of whom were clinically tested. Even though we have found relatively high correlations between

different clinical tests and our results, it is imperative that models for new patients be created and clinically tested. Additionally, it is important to note that neither the SOE measurements used to test the accuracy nor the clinical measurements used to quantify the validity our models are completely independent from the AGF and SOE measurements used in the training process. We did not have access to any independent information that can be used as a ground truth against which the model results can be tested. As a future work, we propose to create the models outlined in this dissertation for unique patient populations as a way to independently test the validity of such models. One such patient population is those with residual hearing after the implantation. It could be assumed with a high confidence that the regions of the cochlea that correspond to the frequencies for which the patients have residual hearing are intact and healthy. Thus, future work could include verifying whether the neural health estimates agree with high neural health in aforementioned cochlea regions. The inverse which states that no residual hearing implies poor neural health, on the other hand, would be inaccurate given that the hearing loss might be due to the damage to hair cells rather than the auditory fibers. Finally, there are known genetic types of hearing loss where the neural survival pattern is known, an example of which is the hearing loss caused by TMPRSS3 genetic mutations. Thus, the models could be created for such patients, and the models' estimates can be compared to known neural survival patterns.

In addition, different clinical tests such as investigating neural response via different stimulation techniques, can be performed. The patient-specific EAMs and ANFMs created in this thesis could be used to develop new model-based CI programming techniques that exploit other settings made available via patients' CIs. CIs attempt to reproduce the original sound spectrum (~30,000 different channels) with at most 22 different electrodes, which limits the spectral selectivity[13]. In current clinical programs, CIs typically use a monopolar (MP) configuration, i.e. an electrode is chosen as the current source injecting certain amount of current into the cochlea

while an extra-cochlear electrode, typically the casing of the CI, is chosen as the ground electrode to which the current sinks. In such clinical programs, electrodes are activated one after the other and the activation order of the electrodes is not optimized. We have shown in Chapter VII that our patient-specific models can simulate SOE measurements with a high accuracy. These measurements include information about the overlapping regions that are activated by two potentially distinct electrodes. Thus, using the patient-specific ANFMs, we can optimize the activation order of electrodes in such a way that the fibers that are activated by a previously activated electrode can go back to its resting state before another nearby electrode is activated. This could significantly reduce the channel interaction artifacts[14,15] and increase hearing outcomes.

In MP configurations, the current path between the source and the ground is largely uncontrolled as the distance between an active intra-cochlear electrode and the CI case ring is relatively larger. This might cause neural activations in sites that do not correspond to the selected channel of the active electrode[16]. A technique that could be used to minimize activation in mismatching channels is current steering (CS), which has been widely studied in the CI community[17,18]. The idea in CS is to stimulate adjacent intra-cochlear electrodes so that "*virtual channels*" in between two or more fixed channels can be created[13]. It has been shown that as many as 7 *virtual channels* could be created between each pair of intra-cochlear electrodes using Advanced Bionics CI[16]. CS might also further improve spectral resolution as the neural activation is expected to occur at sites located in between the stimulated adjacent electrodes. Even though it has been shown that spectral resolution on average is increased with CS, no significant improvement in speech recognition compared to the monopolar configuration was found[16]. In other studies conducted, CS was found to increase hearing performances for some patients while decreasing for others[19–21]. In such studies, CS technique was applied blindly, i.e. *virtual channels*

were created between each pair of electrodes with the goal of increasing spectral selectivity as much as possible. However, using CS between electrodes that have a high degree of stimulation overlap might be counterproductive as the nerve fibers that sit in between the two electrodes suffer from spectral smearing. We hypothesize that model-guided CS could increase spectral resolution and be more beneficial than blindly applying CS to each pair of electrodes. This could be achieved by enabling CS only between neighboring electrodes that stimulate groups of nerves that are as independent from each other as possible, and such pairs of electrodes could easily be determined using the electro-anatomical and auditory nerve fiber models as presented in Chapter VII. Current focusing (CF) is another technique that could improve spectral resolution. In CF, an intra-cochlear electrode is used to deliver current to the neural activation sites while one or more neighboring electrodes are chosen as the ground. Even though CF has great potential for increasing the number of possible channels, it has been shown to lead to both positive and negative outcomes in CI patients[16,22–25]. We believe that this might be due to blindly implementing CF with the assumption of ideal electrode placement and the use of symmetrically distributed signal levels. We believe that the effectiveness of CF could also be improved with model-guidance because we have shown in Chapter VII that our patient-specific models enable estimation of neural activation.

This dissertation presents methods that can be used to create patient-specific electro-anatomical and auditory nerve fiber models as presented in Chapter IV, V, VI and VII and outlines a possible future use as described in this chapter. The model estimates have already been clinically tested, however more clinical verification is imperative. Even though the techniques developed herein may not be the final solutions for creating models of electrically stimulated cochlea, we believe this work has made valuable contributions towards improving hearing outcomes for CI recipients and that it provides efficient tools for future research related to programming.

References

1. Cakir A, Labadie RF, Zuniga MG, Dawant BM, Noble JH. Evaluation of Rigid Cochlear Models for Measuring Cochlear Implant Electrode Position. *Otol Neurotol*. 2016;37(10):1560-1564. doi:10.1097/MAO.0000000000001245

2. Rivas A, Cakir A, Hunter JB, et al. Automatic Cochlear Duct Length Estimation for Selection of Cochlear Implant Electrode Arrays. *Otol Neurotol*. 2017;38(3):339-346. doi:10.1097/MAO.0000000000001329

3. Cakir A, Dwyer RT, Noble JH. Evaluation of a high-resolution patient-specific model of the electrically stimulated cochlea. *J Med Imaging (Bellingham)*. 2017;4(2):025003. doi:10.1117/1.JMI.4.2.025003

4. Cakir A, Dawant BM, Noble JH. Development of a $$\upmu $$CT-based Patient-Specific Model of the Electrically Stimulated Cochlea. In: Descoteaux M, Maier-Hein L, Franz A, Jannin P, Collins DL, Duchesne S, eds. *Medical Image Computing and Computer Assisted Intervention − MICCAI 2017*. Lecture Notes in Computer Science. Springer International Publishing; 2017:773-780.

5. Cakir A, Labadie R, Noble J. Auditory nerve fiber segmentation methods for neural activation modeling. *JMI*. Under review.

6. Cakir A, Dwyer RT, Katelyn B, Gifford RH, Noble J. Auditory neural health imaging (ANHI) using patient-customized models. *PNAS*. Under review.

7. Noble JH, Labadie RF, Majdani O, Dawant BM. Automatic segmentation of intracochlear anatomy in conventional CT. *IEEE Trans Biomed Eng*. 2011;58(9):2625-2632. doi:10.1109/TBME.2011.2160262

8. Wahba G. A Least Squares Estimate of Satellite Attitude. *SIAM Rev*. 1965;7(3):409-409. doi:10.1137/1007077

9. Escudé B, James C, Deguine O, Cochard N, Eter E, Fraysse B. The size of the cochlea and predictions of insertion depth angles for cochlear implant electrodes. *Audiol Neurootol*. 2006;11 Suppl 1:27-33. doi:10.1159/000095611

10. Cakir A, Dawant BM, Noble JH. Evaluation of a μCT-based electro-anatomical cochlear implant model. In: Webster RJ, Yaniv ZR, eds. San Diego, California, United States; 2016:97860M. doi:10.1117/12.2217275

11. Bookstein FL. Principal warps: thin-plate splines and the decomposition of deformations. *IEEE Transactions on Pattern Analysis and Machine Intelligence*. 1989;11(6):567-585. doi:10.1109/34.24792

12. Rattay F, Lutter P, Felix H. A model of the electrically excited human cochlear neuron. I. Contribution of neural substructures to the generation and propagation of spikes. *Hear Res*. 2001;153(1-2):43-63.

13. Nadol JB, Shiao JY, Burgess BJ, et al. Histopathology of cochlear implants in humans. *Ann Otol*

Rhinol Laryngol. 2001;110(9):883-891. doi:10.1177/000348940111000914

14. Kamakura T, Nadol JB. Correlation between word recognition score and intracochlear new bone and fibrous tissue after cochlear implantation in the human. *Hear Res*. 2016;339:132-141. doi:10.1016/j.heares.2016.06.015

15. Choi CTM, Lee Y-H. A Review of Stimulating Strategies for Cochlear Implants. *Cochlear Implant Research Updates*.:16.

16. Baer T, Moore BCJ. Effects of spectral smearing on the intelligibility of sentences in the presence of interfering speech. *The Journal of the Acoustical Society of America*. 1994;95(4):2277-2280. doi:10.1121/1.408640

17. Rubinstein JT. How cochlear implants encode speech: *Current Opinion in Otolaryngology & Head and Neck Surgery*. 2004;12(5):444-448. doi:10.1097/01.moo.0000134452.24819.c0

18. Berenstein CK, Mens LHM, Mulder JJS, Vanpoucke FJ. Current steering and current focusing in cochlear implants: comparison of monopolar, tripolar, and virtual channel electrode configurations. *Ear Hear*. 2008;29(2):250-260.

19. Donaldson GS, Kreft HA, Litvak L. Place-pitch discrimination of single- versus dual-electrode stimuli by cochlear implant users (L). *J Acoust Soc Am*. 2005;118(2):623-626.

20. Firszt JB, Koch DB, Downing M, Litvak L. Current steering creates additional pitch percepts in adult cochlear implant recipients. *Otol Neurotol*. 2007;28(5):629-636. doi:10.1097/01.mao.0000281803.36574.bc

21. Drennan WR, Won JH, Nie K, Jameyson E, Rubinstein JT. Sensitivity of psychophysical measures to signal processor modifications in cochlear implant users. *Hear Res*. 2010;262(1-2):1-8. doi:10.1016/j.heares.2010.02.003

22. Donaldson GS, Dawson PK, Borden LZ. Within-subjects comparison of the HiRes and Fidelity120 speech processing strategies: speech perception and its relation to place-pitch sensitivity. *Ear Hear*. 2011;32(2):238-250. doi:10.1097/AUD.0b013e3181fb8390

23. Won JH, Nie K, Drennan WR, Rubinstein JT. Maximizing the spectral and temporal benefits of two clinically used sound processing strategies for cochlear implants. *Trends Amplif*. 2012;16(4):201-210. doi:10.1177/1084713812467855

24. Bierer JA. Threshold and channel interaction in cochlear implant users: evaluation of the tripolar electrode configuration. *J Acoust Soc Am*. 2007;121(3):1642-1653.

25. Bierer JA. Probing the electrode-neuron interface with focused cochlear implant stimulation. *Trends Amplif*. 2010;14(2):84-95. doi:10.1177/1084713810375249

26. Landsberger DM, Padilla M, Srinivasan AG. Reducing current spread using current focusing in cochlear implant users. *Hear Res*. 2012;284(1-2):16-24. doi:10.1016/j.heares.2011.12.009

27. Srinivasan AG, Padilla M, Shannon RV, Landsberger DM. Improving speech perception in noise with current focusing in cochlear implant users. *Hear Res*. 2013;299:29-36. doi:10.1016/j.heares.2013.02.004